THE UNIVERSITY
of EDINBURGH

Biological evolution and the physics of growing microbial colonies

Jakub Pastuszak

Doctor of Philosophy
The University of Edinburgh
2016

Abstract

In this thesis I investigate the role of spatial structure, cell-cell interactions and horizontal gene transfer on the genetic composition of growing microbial colonies. In the first part I study how the roughness of the growing layer of the colony depends on the shape of colony-forming cells. To study its impact I develop an off-lattice Eden-like model in which cells are represented as spherocylinders with a variable aspect ratio. I show that the roughness of the expansion front is not significantly affected by the shape of cells and that the dynamic scaling of growing front belongs to the KPZ universality class.

Roughness is an important and easy to measure feature which affects the probability of fixation of genetic lineages in the colony. Another feature contributing to the genetic composition of a microbial community is horizontal gene transfer, which is investigated in the second part of this thesis. I develop an agent-based computational model of bacterial cells which grow, divide, and interact mechanically. I focus on plasmid conjugation, in which donors transfer a plasmid (a small, circular DNA molecule) to plasmid-free recipients. I show that bacteria in the expanding colony segregate into sectors of donors and acceptors. Donor sectors grow at the expense of acceptor sectors and that effect can be effectively described by coalescing random walkers that perform biased random walk on the colony expansion front. I use numerical and analytical methods to show that the plasmid eventually spreads to the whole colony given enough time, and I also show that this time is unrealistically long for experimentally determined conjugation rates and therefore real colonies are expected to have both acceptor and donor sectors. Furthermore, my simulations show that segregative plasmid loss at the moment of cell division can counteract the effect of conjugation and can lead to fixation of plasmid free cells. I also show that changes in nutrient concentration and the resultant change in roughness of the expansion front affect the rate of plasmid spread into population. Quantitative and qualitative results

obtained in this section may serve as a tool to extract plasmid invasion rates from experimental data.

In the last part of this thesis I investigate how the physical factors, such as finite strength of conjugative junctions, affect the conjugation process. I develop a computational model of plasmid transfer in which conjugative junctions are explicitly modelled as short, spring-like tubes that connect conjugating cells. My results show that factors such as junction creation rate and its strength can significantly affect the conjugation performance. I study different situations corresponding to different experimental scenarios (well-mixed colony on a filter paper, colliding colonies) and show that shear forces acting between cells can significantly lower the rate of plasmid transfer. My results can explain why conjugation occurs very rarely in some of these scenarios investigates in laboratory assays.

Lay summary

In my thesis I studied the physics of expanding microbial colonies and its role in biological evolution of bacteria. Bacteria often attach to surfaces on which they form colonies and biofilms. Surface-attached bacterial populations are important from the medical and industrial viewpoint (teeth plaque, biofilms on surgical implants, water distribution pipes etc.) but little is known how mechanical interactions between cells in such communities affect their growth and evolution. Here I investigated the effects that such interactions may have on the genetic composition of bacterial colonies.

First, I studied the impact of the shape of bacterial cells on the growth of a bacterial colony. I considered two different shapes common among real bacteria: spherical and rod-like. I simulated a simple model of a growing colony and showed that the shape did not significantly affect statistical properties of the colony such as the roughness of the growing layer of cells.

I then turned to biological evolution and studied plasmid conjugation in bacterial colonies. Conjugation is the process in which two cells exchange genetic material in the form of small, circular DNA molecules called plasmids. Conjugation requires physical contact between cells and is thus an important process by which genes are transferred between unrelated individuals in dense microbial communities. Given that many plasmids contain genes responsible for antibiotic resistance, understanding conjugation is of paramount importance. I developed a computational model of mechanically interacting bacterial cells in which some of the cells were plasmid donors that could donate the plasmid to plasmid-free cells. I showed that bacteria in the colony segregated into sectors with and without the plasmid, and that plasmid-bearing sectors grew at the expense of plasmid-free sectors.

Furthermore, I showed that the plasmid eventually spreads to all cells in the

population given enough time, but that this time can be unrealistically long and that typically both plasmid-bearing and plasmid-free cells would be observed in the colony. I also showed that the roughness of the growing layer of cells affects the rate with which the plasmid spreads in the population, with rougher layers causing the plasmid to spread faster. Previous work has demonstrated that roughness affects the probability that a new mutation spreads in the colony. My work shows that the same holds when new genes are passed by conjugation.

Finally, I studied how physical connections between conjugating cells affect conjugation. I developed a more detailed simulation to show that conjugative junctions created between bacteria passing the plasmid can stabilize the mating pair of cells against external forces that would otherwise pull the two mating cells apart. These results could explain why conjugation occurs very rarely in some experiments where the relative motion of bacterial cells is particularly strong.

Declaration

I declare that this thesis was composed by myself, that the work contained herein is my own except where explicitly stated otherwise in the text, and that this work has not been submitted for any other degree or professional qualification except as specified.

(Jakub Pastuszak, October 2016)

Acknowledgements

I would like to thank my supervisor, Dr Bartek Waclaw, for his guidance through my PhD, for his infectious enthusiasm for science that kept me inspired and motivated during my good and bad PhD days, and for his advice on big academic topics and small day-to-day matters. I would like to thank my second supervisor, Dr Rosalind Allen, for her help, insightful conversations, input of new ideas and her useful comments that contributed to my overall progress. I would like to thank EPSRC and SUPA for funding and giving me the chance to walk the scientific path.

I want to thank Jane Patterson for her help, answering my questions about formalities and her guidance through twisted procedures. I want to also thank the course organisers I had a great pleasure to work with as a teaching assistant: Dr Will Hossack, Dr Simon Titmuss and Prof Alex Murphy.

Thanks to Dario, Diarmuid, Alex, Gavin, Chay, Vlad, Elena, Susana, Petra and others for all those less-and-more geeky conversations, great ideas, humour and companionship during the lunch, coffee and Friday beer times.

Big thanks to Monika for being a great companion, for great patience about me trying to be a scientist, for being an inspiring and motivating soul mate who positively charged my days and nights with a great vibe.

Finally, the biggest thanks go to my family, my parents Danuta and Mariusz, my sister Dominika, my grandparents Danuta, Stanislaw and Salwina, my godmother Joanna and others. Without you and your support I would not be able to write these lines here and now, I would not make it through the undergraduate ground, and I would not make it all the way up to top of the PhD hill.

Contents

Chapter 1

Background

Approximately 4 billion years ago out of the primordial soup of chemical ingredients and driven by thermodynamic processes, the first entities capable of self-reproduction emerged and gave rise to life on Earth [1]. Starting from the single universal common ancestor, and moved forward by the force of evolution, the first lifeforms then segregated into three domains: Arachaea, Bacteria and Eukaryota. Throughout millions of years of evolution the eukaryotic life developed into the most complex multicellular forms that one can find on Earth today, with the plant and animal kingdom species being the best examples of these [2]. Arachaea are unicellular prokaryotic micro-organisms that were initially taken for bacteria, yet their biochemistry and metabolic pathways make them very different from the other two kingdoms [3]. It is bacterial living matter, however, that is observed to be the most diverse and abundant on our planet. Microbiologists consider two bacterial cells belong to the same bacterial species if 79% of their chromosomal DNA is the same [4] and, based on this definition, it is estimated that the total number of bacterial 'species' is of the order of 10^9 [5] which greatly exceeds the number of species in other two kingdoms [6]. For comparison, it is estimated that the number of insect species, which are the most diverse representatives of eukaryotic life, is of the order of 10^7 [7].

Bacteria had been present long before the first multicellular organisms emerged on Earth, and now they form many ecosystems found on Earth. They are a vital part of ecological and geochemical processes forming the basis of complex regulatory networks in the environments inhabited by higher-order organisms. As far as the history of our own species goes, bacterial cells play an important role in human

health. Many of them cause harmful diseases such as legionella, salmonella or pneumonia, with the treatment of these diseases becoming more difficult as new mutant strains, resistant to current treatments, constantly evolve [8, 9]. Yet, the pathogenic effects of bacteria are only a part of the story. It is estimated that the human skin and gut microbiome hosts 5 000 - 10 000 species of bacteria and the total number of bactieral cells in or on our bodies can outnumber our own body cells [10, 11]. Thus, one could say that the human body is a reservoir of bacterial cells. These unicellular organisms make our lives possible as they contribute to human metabolism [12] and immune system response [13]. Some studies even suggest a connection between the gut microbiome and neural responses. For example, *Bacteroides fragilis* bacteria that are common in the human gut, are shown to reduce autism in mice when moved from human to mouse guts [14]. These examples highlight the fact that the way bacteria live and the way they evolve is highly correlated with our own life cycles. Hence, understanding how bacteria grow and evolve is of essential importance in relation to human health and well-being.

1.0.1 Bacteria and physics

Even though the field of biological sciences is usually associated with study of microbial organisms, the physicists' point of view is nevertheless of extreme importance for understanding the underlying principles of bacterial life. Single cells can be considered as out-of-equilibrium entities that eat, grow and divide. They move around in search of food by performing a run-and-tumble motion that can be described as diffusive phenomenon [15]. The food is converted to ATP molecules which in turn serve as the energy source used to perform necessary functions such as synthesis of vital proteins [16], and the underlying principles can be described by statistical physicists who use models such as totally asymmetric simple exclusion process (TASEP) to investigate such processes [17]. All the vital functions are encoded in cell DNA, and the thermodynamic approach to gene activity uses concepts like free energy to give key insights into gene expression and DNA activity [18]. And all these things take place within elastic and porous cell envelope with mechanical properties such as elasticity and friction which are described with tools belonging to the domain of classical physics [19].

As discussed in later sections, single bacterial cells naturally assemble into large populations. Moving from a single-cell scale to large collection of growing

and interacting cells, physics again becomes a key tool for investigation. The population of cells acquires energy by eating nutrients and this energy flux causes the growing population to be far from equilibrium. The term 'active matter' is used to describe such systems, and many different tools have been adapted and developed by statistical physicists to account for phenomena associated with active matter. As seen later in Chapter 2, simple statistical models of microbial population growth capture some of the dynamical properties that can be related to experimental observations on microbial colonies. As discussed in section 1.2, tools normally used to describe physics of liquid crystals and dense suspension flow can be adapted to capture the behaviour of growing microbial populations and to successfully predict some of the statistical phenomena [20].

The above general examples highlight the importance of physics and the role of physicists in the exploration of living matter and the underlying principles that govern live. This thesis explores the phenomena associated with growth and genetic diversity of bacterial colonies. It explores the effect of bacterial cell shape on the properties of growing colony, and further explores factors that contribute to the observed genetic diversity of growing microbial populations. The approach focuses on careful modelling of underlying physics and interactions that give rise to the collective behaviour and evolution of bacterial colonies. The mixture of computational and analytical methods in this work allows one to take an accurate physical point of view on growing colonies. The results obtained in later chapters show that the accurate physical modelling of biological phenomena serves as a very powerful tool in exploration of living matter. The following sections give more details on phenomena under consideration and features that are of particular interest in this thesis.

1.1 Bacterial populations and their evolution

As already mentioned, individual bacterial cells are perfectly capable of living the individual, asocial life. For example, when living as individual cells in planktonic, liquid medium, *E.coli* cells use their flagella motors to swim through liquid suspensions in search of food while responding to nutrient gradients [23]. However, in the natural environment it is believed that bacteria usually assemble together in dense, surface attached communities. This multicellular assembly process is believed to be survival strategy targeted at better nutrient distribution and adaptation to harsh environments [24]. Micro-colonies and biofilms are the

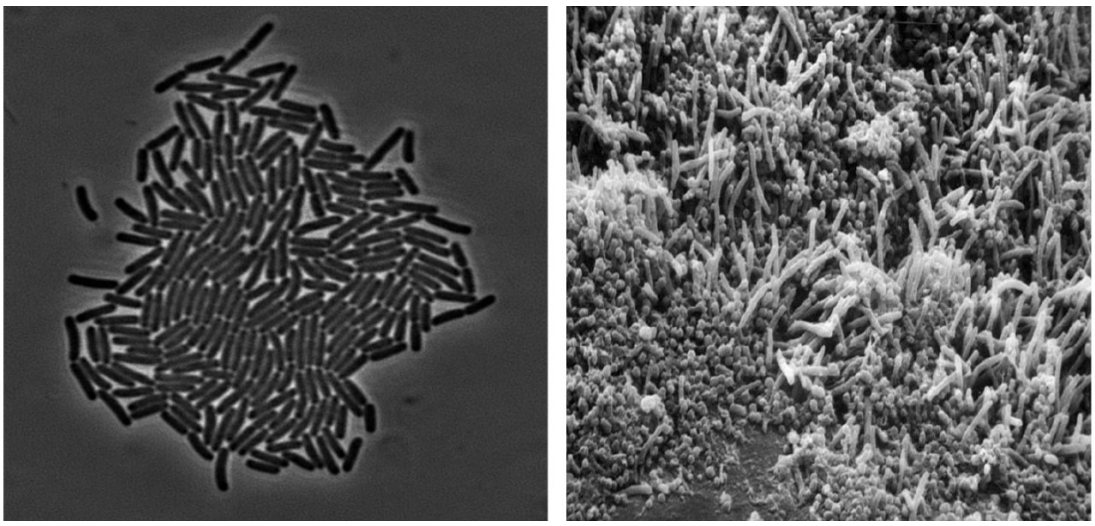

Figure 1.1 *Two common ways bacterial cells assemble into populations. Left: The bright-field microscope image of microbial colony grown on an agar plate. The initial growth is confined to two dimensions, however, the build up of pressure can cause the transition into the third dimension. Micro-colonies are usually dense and consist of relatively few bacterial species (Image source: [21]). Right: The microscope image of dental plaque biofilm, with the more complex structure as compared to that of a micro-colony. Biofilms are surface attached aggregates consisting of many types of cells that are kept together by an extracellular polymer matrix. They are found in many different and often extreme environments. Due to high adaptability and fast evolution of cells living within biofilms, these microbial communities are a serious problem if they host pathogenic bacteria (Image source: [22]).*

two most common types of such microbial populations observed in nature. Fig. 1.1 shows images of these two forms of microbial growth. Biofilms are dense communities that form on flat surfaces in almost any environmental conditions, including sanitary devices [25], human teeth [26] and plant leafs [27]. Biofilms are characterized by complex spatial structure, and can contain multiple species of bacteria, linked by complex interactions and metabolic networks. A biofilm structure is typically stablized by an extracellular matrix. Biofilms are highly adaptable to changing surroundings [28], a phenomenon that can pose a serious problem if the biofilm is composed of pathogenic cells, because the biofilm is difficult to remove.

While biofilms are important in disease and in the natural environment, the other form of microbial growth, colony formation, is easier to study in the laboratory. Bacterial colonies are simpler in structure and are easier to grow in laboratory conditions. Because of this, bacterial colonies are a useful laboratory tool with which to study multicellular assembly processes. The growth of a colony starts

from one or more cells located on the surface of a suitable medium that provides mechanical support and nutrients. These founder cells start to divide and the colony expands while it is able to access nutrients from its surroundings. The initial growth is usually confined to two dimensions, however it is often observed that mechanical forces acting between individual cells and the pressure build-up due to colony growth can eventually lead to expansion into the third dimension [29]. If colonies are given enough nutrients and time to grow they can quickly evolve, giving rise to new mutants.

Within a spatially organised bacterial population like a biofilm or a colony, there is evidence that cells specialize into different phenotypic types. This specialization may be beneficial in terms of the overall growth rate and survival in the presence of stress [30, 31]. During the specialization process, different cells acquire different roles in metabolic and singalling processes, in a process that is highly dependent on the environment, nutrient distribution and the population age [32]. It is also known that in some bacterial species, individual cells can switch stochastically between different phenotypes, which leads to rapid adaptation to changing environmental conditions [33]. The structure of microbial populations can also be affected by quorum sensing [34]. This phenomenon occurs when cells secrete small, diffusive signalling molecules into the nearby environment that can be sensed by surrounding cells. The concentration of these signalling molecules is highly dependent on the surrounding environment and state of the population, in particular its cell density. Bacteria can sense the local concentration of signal molecules and respond to this in a variety of ways. For example, it is observed that the critical concentration of certain signal molecules triggers biofilm formation in *Pseudomonas aeruginosa* [35]. Other responses include an increase in pathogenity or induced motility of individual cells [36]. Quorum sensing regulated behaviours are often thought to be cooperative, in the sense that a bacterial cell secretes a product that benefits not just itself but also surrounding cells. However, within biofilms and colonies, competitive processes can also occur [37]. For example, different strains compete for space and nutrients, and natural selection acts on these strains favouring ones which perform better in this competition.

E.coli cells can grow very fast, with a doubling time of 20 minutes under optimal laboratory conditions [38]. *E.coli* can also mutate rapidly, with a typical mutation rate of $\sim 1 \times 10^{-3}$ per genome per generation [39]. Such large mutation rates and small division times mean that bacterial evolution can happen very fast. There are two main mechanisms of evolution in bacterial populations. Vertical

gene transmission by cell reproduction allows transfer between cells in successive generations [40, 41]. When a cell divides, the offspring cell inherits the genetic material of the parent cell. This form of gene transmission is susceptible to point mutations in the genome during the replication process, and due to molecular changes from the external factors acting on the cell during its life-cycle. Such genome mutations drive the evolution and give rise, on a long timescale, to new species which then can become dominant in ecosystems, given that they reproduce fast enough. Thus, natural selection acts on these species and ensures that the most beneficial features are propagated into future generations. It is common to visualise vertical gene transmission in the form of phylogenetic tree of life [42], such as in the left panel in Fig. 1.2. Successive families (or species) form the branches of the tree that meet at the point of the last common ancestor.

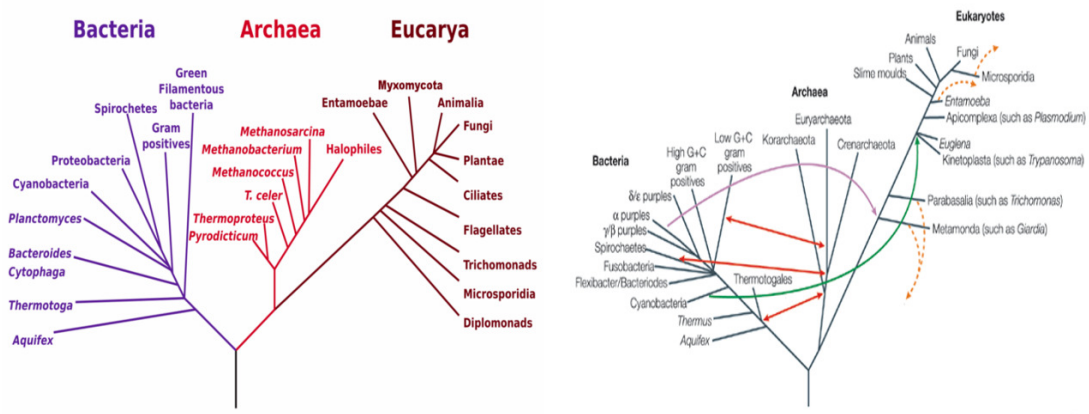

Figure 1.2 *Left: A simple schematic of a rooted phylogenetic tree. Each branch corresponds to different taxa (i.e family) of organisms and different branches meet at the point of the common ancestor. In the case presented, the black root corresponds to the last universal common ancestor of all the living forms. (Image adapted from: [43]) Right: Horizontal gene transfer is the transfer of genes between taxa that do not necessarily share the common ancestor, as indicated by arrows in the picture. Hence, the phylogenetic tree is no longer a tree but a network in which different branches are connected with horizontal links (Image source: [44]).*

While vertical gene transfer is important, it is believed that horizontal gene transfer may also play a crucial role in the evolution of bacterial populations. Horizontal gene transfer (HGT) is the transmission of genes by means other than cell reproduction [45]. There are three main types of HGT [46]:

1. **Conjugation**: cells in direct contact with each other can transfer small, circular pieces of DNA (plasmids) from one cell to a neighbour.

2. **Transformation**: introduction of foreign DNA into the cell genome. Such DNA can be introduced from the environment or in laboratory assays.

3. **Transduction**: DNA is transferred between cells by viruses (bacteriophages in the case of bacteria)

Horizontal gene transfer may have played a very important role in the early evolution of life, and it has been shown to be a major driver in evolution of microbes [46]. For example, in the natural environment, bacteriophages outnumber bacterial cells by a factor of 10 [47] and there can be several conjugation events per lifespan of a bacterial cell [48]. Moreover, all the three mechanisms of HGT can take place between cells of different species [44]. Hence, one needs to reconsider the traditional view of the phylogenetic tree of life in which speciation due to vertical gene transfer gives rise to branches of the tree. Since HGT can act between different species, different branches of the phylogenetic tree may be horizontally connected (hence the name 'horizontal gene transfer'), see the right panel in Fig. 1.2.

1.1.1 Bacterial conjugation

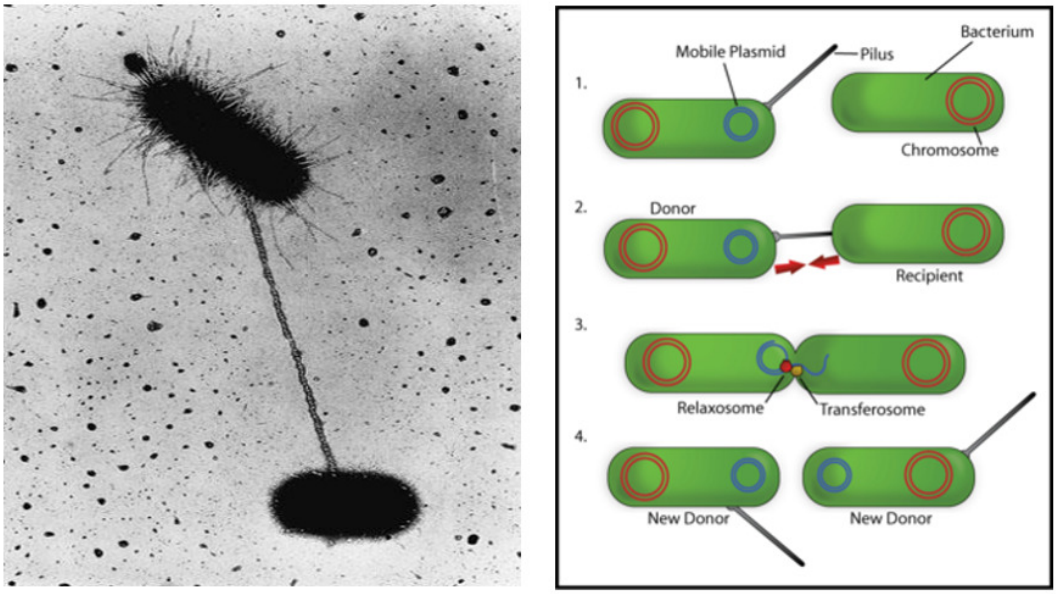

Figure 1.3 *Left: The microscope image of two conjugating cells. The long sex pillus that is used to bring two cells together is clearly visible (Image source: [49]). Right: The scheme of conjugation process. Pillus retraction is used to bring two cells (plasmid donor and recipient) into mechanical contact with each other. The plasmid is copied and transferred to the recipient cell which then becomes the transconjugant cell that is capable of donating the plasmid to other recipients (Image source: [50]).*

A big part of this thesis focuses on horizontal gene transfer by plasmid conjugation in spatially structured populations. Plasmid conjugation was first discovered in 1946 by Joshua Lederberg and Edward Tatum [51]. During this process, two cells exchange genetic material in the form of a small, circular piece of DNA called a plasmid [52]. Fig. 1.3 shows a microscope image of two conjugating cells, together with a schematic showing the main steps of this process. A 'donor' cell, which contains a plasmid, can transmit a copy of its plasmid to a plasmid 'recipient' cell, if the mechanical contact between cells is established and if the environmental conditions are favourable. The mechanical contact is faciliated by a sex pilus that is synthesized by the plasmid donor cell and is used to bring the two cells together. The plasmid is moved between cells and after the process is complete the plasmid recipient cell becomes a new donor (called a transconjugant cell) which can then take part in further propagation of the plasmid. The plasmid itself is a circular DNA molecule that is independent of the bacterial chromosomal DNA. Similarly to viruses, plasmids depend on the DNA replication machinery of the bacterial host for their replication. In contrast to a virus, however, the plasmid does not posses a protein capsid; instead, it is a naked strand of DNA that is transmittable between cells. Plasmids vary in size between a few and a couple of hundred of kilobase pairs [53]. Usually, in the case of large plasmids their DNA codes for the their own life-cycle functions such as maintenance and transfer. In contrast, smaller plasmids tend to rely on enzymes found in the host cell, while larger plasmids usually carry enough genes to maintain their own life-cycle [54]. Plasmids can be found in multiple copies within one cell and plasmid copy number varies between few to several hundred plasmids per cell [55].

The first plasmids were discovered and described over 50 years ago [56] and since then several thousand plasmids have been characterised [57]. Plasmids can be classified in several different ways. One can distinguish between conjugative and non-conjugative plasmids. Conjugative plasmids have a set of transfer genes that allow them to initialize the conjugation process [58]. Non-conjugative plasmids rely on the transfer gene region of conjugative plasmids and can be considered as parasites that can propagate in the presence of other conjugative plasmids [59]. Another way to classify plasmids is based on the replication control genes and their associated incompatibility (Inc-) groups [60]. 'Plasmid incompatibility' arises when another plasmid introduced to the plasmid hosting cell disturbs the inheritance of both plasmids in the absence of selective pressure. In particular, introduction of the second plasmid to the cell that already hosts a plasmid of the same incompatibility usually causes both plasmids to be lost from a host cell.

Hence, plasmids that belong to the same incompatibility group are not able to coexist in the same cell for a significant length of time [61]. This occurs because the host cell is unable to maintain two plasmids with the same set of origin-of-replication genes [62]. It is also commonly observed that conjugation is not even initialized if plasmids in the donor cell are incompatible with those in the recipient cell. This is caused by a phenomenon called surface exclusion, which arises when the donor cell does not recognize the recipient cell. In such cases, the incompatible plasmids code for proteins that are present at the surface of the recipient cell and inhibit the mating pair formation [63, 64].

Typically, plasmid DNA does not code for vital functions of the host cell, but it provides additional genetic information which, when expressed, can contribute to the fitness of the host cell. In order to confer a fitness advantage, plasmid-encoded genes should be beneficial enough to balance the metabolic cost of carrying the plasmid. If this is not the case then plasmid-carrying cells will be outcompeted by those that do not carry the plasmid. The effects of plasmids on the host cell vary between plasmids, and plasmid function provides another way to classify plasmids. Degredative plasmids code for enzymes that digest unwanted substances and toxic metabolic byproducts [65, 66]. Other plasmids can code for bacterial proteins that are used to kill other cells [67, 68]. Virulent plasmids can change relatively harmless bacteria into pathogens that secrete toxic substances [69]. Fertility (F) plasmids rapidly spread in bacterial populations since they code for the highly expressed conjugation system [70]. Plasmids have also been observed to be involved in the establishment of social interactions in a similar way to signalling proteins used in quorum sensing [71]. Moreover, plasmid DNA has also been observed to be of importance in the triggering of biofilm development [72].

Conjugative resistance (R) plasmids code for antibiotic resistance traits such as beta-lactamase enzymes that are expressed in *Enterobacteriaceae* [73, 74]. Because they confer a significant fitness gain for the host cell in the presence of antibiotics such as penicillins and cephamycins, R plasmids spread fast. For example, in recent years there has been an increased overuse of antibiotics in livestock where animals grown in crowded conditions are fed with antibiotics to avoid the spread of diseases in herds. This has led to a fast spread of antibiotic resistance genes [75, 76]. Additionally, antibiotics are commonly used in the treatment of human diseases that are not bacterial, for example the common cold or the flu [77, 78]. These actions contribute to a selective pressure promoting the

maintenance and spread of resistance genes carried by plasmids. A recent example is the emergence of the NDM-1 (New Delhi Metallo-beta-lactamase-1) enzymes that make bacteria resistant to a variety of antibiotics, including carbapenem [79, 80]. Conjugative plasmid carried genes responsible for NDM-1 that originated in Sweden are now widely spread around the world, including Japan and USA [81]. mcr-1 is another resistance gene that originated in China and in 2015 was found in imported meat in Denmark [81, 82]. mcr-1 is spread by conjugative plasmids and confers resistance to all the commonly used antibiotics, including colistin, which some researchers term as our last line of defence against bacterial diseases [83]. These are situations every doctor wants to avoid, as the diseases that were easily treatable yesterday might soon become deadly again. Although plasmid spread thus poses global health risks, it is also worth to note that plasmids and their associated genetic material are an essential tool in laboratories. In particular, plasmids are used by genetic engineers as vectors to introduce foreign genetic material into cells [84, 85]. By careful manipulation of the plasmid DNA it can be set to replicate and clone inside cells. Such methods allow exploration of functions of certain proteins and their effect on the cell life-cycle [86].

The conclusion that can be drawn from the above examples is that plasmids and plasmid conjugation are very common in nature and have a variety of important functions. They are used by evolution as a tool for phenotype spread, population diversification and adaptation. They are also an important tool in a variety of laboratory assays. As discussed, microbial communities found in hospitals and the human body etc., often live in surface attached communities where bacteria are located in close proximity to one another. Under these conditions one would expect plasmid transfer to be rapid. Therefore, conjugative plasmids may have important effects on such bacterial communities. However, despite the importance of conjugation in evolutionary dynamics, it is still a relatively poorly understood phenomenon in the context of spatially structured populations such as microbial colonies. Given the omnipresence of such populations and their impact on human life, it is essential to understand the main driving forces behind their evolutionary dynamics. In this work computer simulations and analytical tools are used to study how plasmids spread in growing microbial communities.

1.2 Computational modelling in microbiology

The computational power that is available in a typical university setting makes it feasible to use simulations as a convenient tool to study large physical and biological systems. In this context, various different models for the growth of microbial colonies have been developed so far. Probably the simplest of these are lattice models. Here, each lattice site hosts an individual cell that is described by a set of states [87, 88], such as cell type or activity. As seen in the next chapter of this thesis lattice based models capture important statistical properties of growing particle systems and allow one to infer the dynamic properties of these. Other lattice-based models include variants of the stepping stone model [89]. This is a quasi-spatial model where instead of an individual cell each lattice node accounts for a certain subset of a population of cells characterized by different properties such as cell concentration or type. Migration between nodes is allowed to account for the spatial diffusion of cells and a certain level of mixing between nodes is present. Other approaches are based on continuum modeling of the flow propertes of a population of cells, which dispenses with the individual treatment of cells in favour of the collective properties of the population. In such continuum models, reaction-diffusion equations are used to model the dynamics of colony expansion [90, 91]. Although the microscopic view of the interactions between individual cells is lost, the properties of the population as a whole can be inferred in a relatively fast and efficient way using numerical solutions of the reaction-diffusion equations.

1.2.1 Off-lattice models

Another approach to modelling microbial colonies is based on individual based off-lattice models [92, 93]. In such models, cells are treated as individual entities capable of reproduction in a continuous space. They can interact with other cells as well as with the surrounding environment. An example of such a model is BacSim that was developed by Kreft et al. [93] and is one of many robust individual based models (IBMs) created for investigating the growth of bacterial cells in biofilms and colonies. In BacSim, cells are represented as spherical objects of variable volume. Interactions between cells and the environment arise from their growth as well as nutrient diffusion and reaction. In recent years, the BacSim model has been improved [94, 95] and the resulting iDynoMiCS framework

includes contributions due to the phenomena such as those associated with the extracellular matrix, environmental pressure and metabolic effects. iDynoMiCS is now widely used to study spatially structured biofilms and serves as a platform to investigate the phenomena associated with biofilm growth. However, the software was not intended to accurately model the physics of cell-cell and cell-environment interactions. In the real world, the growth and statistical properties of microbial colonies are driven by the details of cell-cell interactions that depend on the shape of the bacterial cell [96]. Further discussion of the biomechanics of cell-cell interactions follows in the next subsection, but an important point to stress beforehand is that some important mechanical components are not taken into consideration in models of microbial growth like those implemented in BacSim and iDynoMiCS. This represents a trade-off: on the one hand, one wishes to model the growth of microbial communities as accurately as possible. On the other hand, the increased complexity of interactions increases the use of computational resources. One needs to find a compromise and set the algorithm so it is both simple enough to be computationally efficient and complex enough to capture the required physics of the system. Complex systems, such as bacterial cells and their populations, are governed by an enormous complexity of interactions at different scales that ultimately govern their collective behaviour. Hence, it is up to the investigator to narrow down the set of dynamic rules which are included in a model and to achieve a compromise. Although iDynoMiCS does not include cell-cell biomechanics, it does capture other interactions that are found to be essential in biofilm growth and development and hence, it serves as a very good framework for the study of biofilms.

It is one of the main objectives of this thesis to apply the agent based off-lattice simulation framework to study the evolutionary dynamics of expanding *E.coli* populations. As opposed to frameworks like BacSim and iDynoMiCS, the shape of cell and the physical interactions between cells will be considered as important factors that contribute to the overall dynamics of the colony growth.

E.coli biomechanics

Bacterial cells can adopt a variety of shapes, as seen in Fig. 1.4. *E.coli* cells are of a rod-like shape (Bacilli) and it has been suggested that this is advantageous over a spherical shape for capturing diffusing nutrients [98]. Small bacteria with high surface-to-volume ratios are more efficient in terms of nutrient uptake

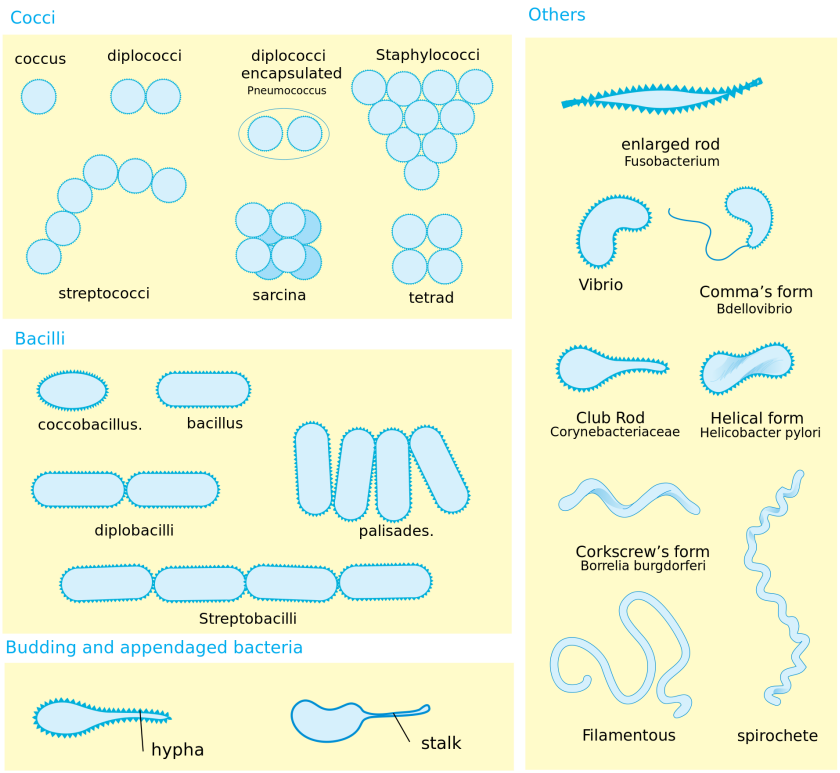

Figure 1.4 *The picture shows the variety of cell shapes that have evolved and are found in nature. As natural selection constantly acts on bacteria, each of these shapes has to be of evolutionary benefit. There is a wide range of environmental conditions that bacteria live in and different shapes provide different selective advantages towards the adaptation and survival of bacterial cells that live under varying selective pressures. (Image source: [97]).*

and are observed to have a fitness advantage when in competition for limited resources with larger cells. The shape of bacterial cells is also important for collective motion in dense bacterial suspensions. The study in [99] shows that irregularly shaped mutants of *Proteus mirabili* bacteria perform worse at the colony formation when their shape deviates from a rod. Studies in [100] and [101] show that very large deviations from the optimal aspect ratio of *E.coli* cells can also inhibit correct biofilm development.

As in the case of dense colloidal dispersions, the mechanical interactions between individual bacterial cells are the main ingredient driving the emergent morphology of colonies [102]. However, little is known about the exact nature of these interactions on the level of individual cells. The flagellar motility of bacterial cells is highly reduced in dense populations [103] and hence, the main force contribution to the dynamics of growth comes from cell proliferation and the resultant interactions between neighboring cells. Individual cells push on each

other as they grow, leading to spatial displacements of bacteria. It has been shown that in the case of rod-shaped cells the spatial structure of colonies is affected by the elasticity of bacterial cells and the substrate they grow on [29]. As already mentioned, mechanical forces can drive the two-dimensional growth of *E.coli* colonies on agar plates into the third dimension. Cell-substrate adhesion is also essential for the initialization and the maintenance of biofilm and micro-colony growth [104]. Moreover, frictional forces between a bacterium and its substrate depend on the nature of the substrate (for example, its stiffness) in a complex way that is highly dependant on the shape of bacterial cell.

Experimental assays on micro-colonies indicate that dense bacterial colonies consisting of rod-shaped cells can make a transition to an ordered (nematic) state when the colony cell density gets high [20]. This transition is related to the well-studied isotropic-to-nematic transition in liquid crystals [105, 106]. Studies of expanding microbial colonies in long, narrow channels [20] show that high cellular flow velocities increase the nematic ordering inside the colony. Cells align along the direction of expansion and the flow propagates the nematic order through the expansion medium. The process of such expansion has been modeled using tools developed for liquid crystal flow [20]. Together with another study in [107] this work predicts the existence of instabilities that lead to disordered domains deep inside the bulk of the colony. Such domains facilitate increased contact between cells and high cell packing ratios [96, 108]. It is worth to point out that such a nematic effect would not be possible for spherically symmetric cells.

The importance of hydrodynamic interactions in bacterial populations has been pointed out as well. Liquid microbial suspensions at high density in low Reynolds number regimes are observed to exhibit a highly collective motion in the form of vortices [109]. Short-lived whirls and jets are observed to increase fluid mixing and the effective diffusion of nutrients inside the colony, causing a more uniform nutrient distribution and hence, better nutrient uptake [110, 111]. Further studies show that there is no need for quorum sensing and other chemical means of communication to induce such vortex instabilities [112]. These observations are quite similar to the self-organized behavior predicted by the Vicsek model that describes the behavior of a set of agents which move with a velocity that is the average of the neighboring agent velocities [92]. The model predicts collective behavior, such as flocking, and can be related to observations on bacterial colonies [109–111]. This highlights the point that hydrodynamics and the resultant fluid dynamics can influence collective behaviour in bacterial suspensions.

1.3 The outline of further chapters

The first aim of this thesis is to investigate how cell shape affects the statistical properties of microbial colonies. The thesis begins with an investigation of the 2D off-lattice model (Eden model) for cells growing in a vertical tube. As discussed in the next chapter, the Eden model is a simple model where discrete reproducing agents give rise to an expanding cluster that mimics the growth of a microbial colony. The model lacks physical interactions between individual cells and the statistical properties of the population are determined by the phenomena occurring on the cluster periphery (i.e interface). The study in this work extends this well understood model for disc-shaped cells towards rod-like cells and explores the effect of the cell shape on the roughness of the growing interface. As further discussed in Chapter 3, the roughness of the interface is an important factor that contributes to the genetic diversity of growing microbial colonies. The approach taken in this study allows to explore the possible relationship between cell shape and the roughness of growing interface, and hence, the genetic diversity of growing microbial colony. The obtained results show that variation in cell shape and length do not affect the properties of the interface (growing front). The study also shows that the interface in the case of rod shaped cells belongs to the KPZ universality class. Only in the case of correlations in the spatial directions of cells there is a small change in the observed scaling dynamics of the initial phase of population growth. Further simulations also show that the statistical properties of the growing population change when the width of the growing interface changes, and that wide interfaces do not belong to the KPZ universality class.

The next chapter further investigates the dynamics and the evolution of genetic diversity of growing microbial systems. In addition to contributions coming from the colony growth and the roughness of expansion front, this chapter investigates the additional effect from plasmid conjugation and its impact on observed genetic diversity of growing *E.coli* microbial populations. Off-lattice simulations of growing colonies are developed and used for the investigation. As compared to the Eden model and computational frameworks such as BacSim and iDynoMiCS[94, 95], the computational model developed in this chapter accounts for details of mechanical interactions between cells. Soft, rod-shaped cells grow on the nutrient medium and mechanically interact with each other as cells do in colonies during microbiology assays. While living on the nutrient medium, cells can exchange plasmids and the net effect is such that interesting

macroscopic patterns in genetic diversity emerge that are subject to investigation in this chapter. The study numerically explores the fate of neutral plasmids and shows that they are capable of overtaking the population, given a long enough colony expansion time. Further investigations show the relationship between the colony's genetic structure and the roughness of the colony expansion front determined by the amount of nutrients in the medium that the colony grows on. These observations highlight the importance of the front roughness in the context of genetic diversity, and support some of the observations made in Chapter 2. The numerical work is further supplemented with the extension of existing analytical models that have been used to study the spatial and genetic structure of expanding micro-colonies. The annihilating random walk theory is used to set up a diffusion equation that allows one to numerically predict the probability of a neutral plasmid overtaking the expanding microbial population.

Finally, in the last chapter the computational model is extended to capture more of the important details that are observed to impact plasmid conjugation. The model developed in this chapter considers conjugation as a non-instantaneous process affected by the surrounding environment. At the expense of computational efficiency the physical connections between conjugating cells that affect the mechanics of cell-cell interactions are implemented. Such 'conjugative junctions' are modelled as spring-like objects providing force that keeps two conjugating cells together. The algorithm developed in this chapter supplements the program developed in Chapter 3 and aims to accurately capture the biomechanical cell-cell interactions that give rise to collective behaviour in growing microbial colonies. Even though the model is based on some assumptions on the nature of conjugative junctions, it is nevertheless one of the first attempts to model conjugation on a single cell level as a biomechanical process. The simulation results show that various physical properties of conjugative junctions, such as their stiffness and resistance to breaking, impact the conjugation performance in various ways. The case of two colliding colonies with conjugation at the collision front is used to show that shear forces due to the relative motion of cells at the collision front can reduce the number of transconjugant cells. It is also shown that the physical connection between mating cells can provide the additional resistance to shear and reduce the impact of shear forces on the number of transconjugant cells. The numerical results in this chapter partially explain the experimental observations obtained from assays performed on colliding colonies, and hence the model developed in this chapter is shown to successfully captures some of the biomechanics of the conjugation process.

Chapter 2

Eden growth

This chapter is inspired by the work of O. Hallatschek [113, 114] who shows that some of the dynamical properties of expanding colonies are universal and belong to a wider class of phenomena. The computational study in this chapter considers the universality of a simple, two dimensional off-lattice Eden model of micro community growth and checks whether the shape of the reproducing agent affects some of the global properties of microbial colony (in particular, the roughness of colony front). By considering reproducing cells as rod-like objects that match the shape of a *E.coli* cell, the Eden model developed in this chapter captures some of the essential features of real microbes that form colonies. To date, there were no studies performed on the Eden model consisting of rod-like agents, and hence this study fills the gap with numerical results relevant to this particular shape of reproducing rods. The results in the chapter are also important in the context of genetic diversity driven by horizontal gene transfer studied later in Chapter 3, where it is shown that the front roughness investigated in this chapter is one of the key factors determining the fate of a plasmid in expanding population.

2.1 Eden growth and universal scaling of the Eden interface

The Eden model was first introduced by Eden in 1961 [115] as a simple growth model to explain biological phenomena such as bacterial colony growth and tissue morphology. Initially developed for 2D growing communities it was later extended

to $d > 2$ dimensions. The main assumption of the model is that cells can reproduce only if they have enough empty space around them, and hence the cluster grows only on its boundary. Cell reproduction events are stochastic and the probability of the cell reproduction depends on the amount of free space around the cell. The growth starts from one or multiple seeds and the cluster that grows in d-dimensions is compact, having constant bulk cell density. However, as the cluster grows, the properties of its periphery (i.e interface) defined in (d-1)-dimensions are driven by stochastic dynamics of the local cell growth. For example, the boundary layer (interface) of the cluster gets rough, see Fig. 2.1 which shows the simulation snapshot for the 2D off-lattice Eden growth (details of the model will be explained later in this section).

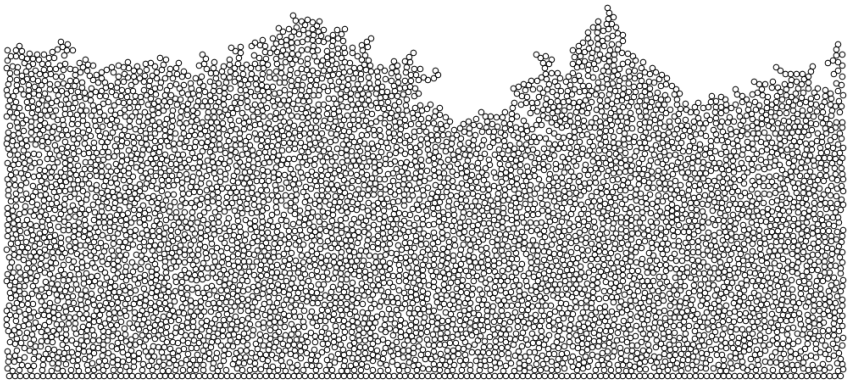

Figure 2.1 *An example of the growth in the vertical tube of size L. The Eden model results in the compact bulk structure consisting of tightly packed cells. As discussed in the main text, the width of the Eden interface can be described by its dynamic scaling properties that are characterized by the roughness, growth and dynamic exponents.*

The interface scaling properties are the result of non-deterministic, stochastic fluctuations of the interface resulting from the dynamics of the cluster growth. The Eden model assumes the growth on the periphery of the cluster and one could argue that such model does not reflect the real experimental observations which show that cells also grow and divide in the bulk of microbial colony [102, 107]. The Eden model takes a simplified view and explores growth properties that are a direct result of the stochastic interface growth only. Nevertheless, as seen later in this and other works, the Eden model and its properties have been succesfully used to describe the growth of microbial colonies [113].

To get more insight into the Eden model, consider an initial line of cells confined to the growth in a two dimensional tube. The net-direction of the interface growth is perpendicular to the initial line of cells and is stochastic due to random

cell reproduction. The growing interface can be described by the height function $h(\mathbf{x}, t)$, which describes the interface distance from the initial flat line of cells, measured at time t and position $\mathbf{x}$. The mean height of the interface at time t is given by Eq.(2.1):

$$\langle h(\mathbf{x}, t)\rangle = \frac{\sum_{\mathbf{x}} h(\mathbf{x}, t)}{L^{d-1}} \tag{2.1}$$

where L^{d-1} gives the size of the surface in $d-1$ dimensions. Note that when $\langle h(\mathbf{x}, t)\rangle$ grows linearly in time the mean interface height can be used as an effective measure of time. The interface width (i.e roughness) is given by the deviation from its mean height and is described by Eq.(2.2):

$$w(L, t) = \sqrt{\frac{1}{L^{d-1}} \sum_{\mathbf{x}} \langle h(\mathbf{x}, t)^2\rangle - \langle h(\mathbf{x}, t)\rangle^2)}. \tag{2.2}$$

The value in Eq.(2.2) indicates the extent of the surface fluctuations in the direction of growth. Starting from the initial seed the interface roughness increases and it has been noted that in many models of surface growth the interface width scales with time as:

$$w(L, t) \sim t^{\beta} \tag{2.3}$$

where β is called the growth exponent. For very long times the extent of fluctuations reaches its maximum and hence the interface width becomes fixed. The numerical observations [116] show that the fluctuation width $w(L, t)$ for long time limits scales with the system spatial size L as:

$$w(L, t \to \infty) \sim L^{\alpha} \tag{2.4}$$

where α is called the roughness exponent and characterizes the width $w(L, t)$ of the steady-state interface. Combining the relations observed in Eq.(2.3) and Eq.(2.4) allows one to rewrite the interface dynamic scaling as:

$$w(L, t) \sim L^{\alpha} f(\frac{t}{L^{\alpha/\beta}}) \tag{2.5}$$

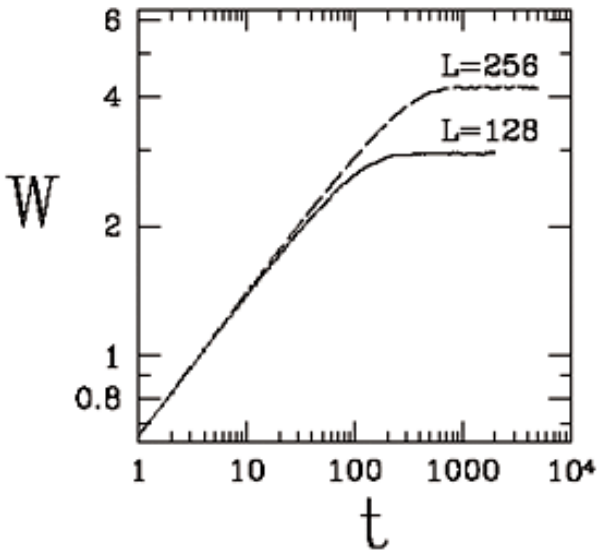

Figure 2.2 *The figure shows the interface width as a function of time. For small t the width scales as t^β, while for long times the growth is in the steady state giving the $w(L,t) \sim L^\alpha$ scaling. The transition to the steady state occurs at the t^z timescales, where $z = \alpha/\beta$. (Image source: [117])*

with $f(x) \sim x^\beta$ for $x \ll 1$ and $f(x) = const$ for $x \gg 1$. The dynamic scaling in Eq.(2.5) allows one to define the time τ to reach a steady state where $w(L, t > \tau) \approx const$ as:

$$\tau \sim L^{\alpha/\beta} \tag{2.6}$$

which in turn allows one to define the dynamic exponent z as:

$$z = \frac{\alpha}{\beta}. \tag{2.7}$$

The exponent z allows one to estimate the time when the interface growth moves to a steady state, given that the values of α and β are known. Fig. 2.2 shows the scaling of interface width with time, with two regimes indicated: an increase in the width determined by β for small t, and the steady state width determined by L and α for large t.

Kardar-Parisi-Zhang universality

After it had been developed, the Eden model was studied to infer its characteris-

tics and the corresponding values of α, β and z exponents. First, the lattice based model for symmetric lattices was studied analytically and numerically [116] to infer that the values of dynamic and roughness exponents for the two dimensional Eden growth were $z = 3/2$ and $\alpha = 1/2$ respectively. One year later, an important paper by Kardar, Parisi and Zhang [118] described the model (named Kardar-Parisi-Zhang (KPZ) growth) of the time evolution of the growing interface and its profile. According to the model, the evolution of the interface local profile is described by the following non-linear Langevin equation:

$$\frac{\partial h(x,t)}{\partial t} = \nu \nabla^2 h(x,t) + \frac{\lambda}{2}(\nabla h(x,t))^2 + \eta(\mathbf{x},t). \tag{2.8}$$

The equation is written down in the frame of reference co-moving with the interface and describes the stochastically evolving height $h(x,t)$ at position x at time t for the interface with a surface tension ν. The first relaxation term accounts for diffusion and interface smoothening. The second term arises due to the curvature of the interface. The slope of interface gives rise to lateral growth and λ is proportional to the average velocity of growth. The noise term in Eq.(2.8) is Gaussian of zero mean, yet studies show that the exact form of noise does not affect the observed scaling.

The renormalization group approach was used to study Eq.(2.8) in [118]. The equation was solved in 2 dimensions and the non-linearity of the growth profile allowed one to infer the existence of the KPZ universality class characterized by the scaling exponents evaluated for the $d = 1+1$ with $\alpha = 1/2$, $\beta = 1/3$ and $z = 3/2$. The same results were obtained by numerical studies one year earlier in [116], and were further confirmed in larger-scale studies [119]. Hence, the conclusion was that the Eden model belongs to the KPZ universality class. However, cases for more than 2 dimensions were not treated in [118] analytically, as for such cases the framework used to study the equation breaks down. Further numerical studies indicated the same scaling behavior ($\alpha = 1/2$, $\beta = 1/3$, $z = 3/2$) for other 2D growth models: ballistic deposition [120, 121], asymmetric solid-on-solid [122] and the single-step growth model [121]. And while first determined for lattice-based growth, the later research, such as in [123], proved that the off-lattice extensions of 2D models, including those with curved surfaces as during the circular growth of microbial colony [124], also give the KPZ scaling. Thus, the universality found in [118] spanned a vast range of 2D growth models where stochastic fluctuations affect the statistical properties of the cluster interface. However, even though

multiple research has consistently shown the same set of exponents for 2D case, there appears to be a larger discrepancy of numerical results when one moves to higher dimensions. Wolf and Kertesz [125] investigated 3-dimensional and 4-dimensional growth on hyper-lattices to obtain $\alpha = 0.33 \pm 0.01$, $\beta = 0.22 \pm 0.02$ for 3D and $\alpha = 0.24 \pm 0.02$, $\beta = 0.146 \pm 0.015$ for 4D system, hinting that values of α and β might depend on the dimensionality of the system. The results in [125] suggested a hypothetical scaling $\alpha = 1/d$ and $\alpha + z = 2$ relation, where d is the dimensionality of the system. Later studies [126] mapped the Eden growth on the problem of a directed walk on random lattice and found that $\alpha = 11/30$ for three dimensional growth. In the mean time, the investigation on solid-on-solid model [127] and further extended to the Eden model in [128] conjectured that $\alpha = 2/(2 + d)$. The resulting roughness exponent of $\alpha = 0.39 \pm 0.03$ for 3D and $\alpha = 0.22 \pm 0.03$ for 4D growth was obtained. The results were obtained with the noise reduction method that was different from other methods used in observations in [125, 126] and which maintained the controversy about the possible universality of the Eden model in higher dimensions. All these examples show that even though a lot of effort was put into the understanding of the Eden model, no general consensus about the scaling and its (super)universality exists.

It is worth to note that the KPZ equation and the associated universality class span a wide class of phenomena. For example, experiments show that when the bacterial colony expands the expanding colony edge very often belongs to the KPZ universality class [113]. The same is true for the front of flame on a slowly burning paper which also belongs to the same universality class [129]. The scaling of fluctuations in totally asymmetric simple exclusion process (TASEP) belongs to the KPZ universality class [130]. Thus, after it was developed the KPZ model of growth became the essential tool to study a wide spectrum of phenomena, and to date the KPZ universality is subject to investigation by many statistical physicists exploring a wide set of phenomena.

2.2 Aims and objectives

The main objective of this chapter is to numerically investigate the 2D off-lattice Eden model for non-spherical cells. The shape of cells used corresponds to that of *E.coli* bacterial cells, i.e two-dimensional rods with circular caps. As already discussed, the 2D off-lattice Eden model has been studied for circular cells ([123, 124]) and the KPZ scaling of the interface has been confirmed. However, there

appears to be no evidence of numerical investigations that would infer the values of α and β exponent for systems consisting of non-symmetric reproducing cells. The aim here is to investigate whether the non-spherical shape of cells affects the interface width scaling.

The Eden model was originally developed to study the growth of microbial colonies. However, rod-shaped bacterial cells of the same species living in micro-colony are of different lengths and spatial orientations of offspring cells after division are correlated [131]. It is possible that such spatial correlations could give rise to long-range interactions that affect the interface scaling. For example, as discussed in Chapter 1, the ordering of individual rods in liquid crystals and bacterial colonies results in ordered domains [20, 106]. It is possible that such effects might arise in the Eden model and affect the interface roughness. To investigate this, simulations of the Eden model with rods of varying lengths and correlated spatial orientations will be performed. As it is discussed in the further chapter of this thesis, the spatial and genetic structure of growing microbial colonies is determined by properties of the expansion front that drives the development of colony morphology. Hence, the investigation in this chapter will be relevant in the context of the expanding colonies investigated later in this thesis.

2.3 Methods

2.3.1 Simulations of Eden growth

Object oriented C++ programming is used to develop the off-lattice computational model to simulate the Eden model and the corresponding interface growth. As opposed to the research done for both lattice-based and off-lattice Eden growth [116, 119], the reproducing cells are not perfectly symmetric. Every cell i is a rod with a center-of-mass position $\mathbf{r_i} = (x_i, y_i)$ and the main-axis orientation $\theta \in [0, 2\pi]$. The hemi-spherical caps have a fixed radius $r = 0.25$ and the diameter of the rod $2r$. The length of the rod measured along the main axis between the centres of two spherical caps is d and thus the total rod length is $l_{tot} = d + 2r$. Depending on the requirements d can be fixed or can be drawn from a distribution of lengths.

The simulation is updated according to the Monte Carlo algorithm. At the every

system update dt (where dt corresponds to one Monte Carlo step, i.e simulation time increment) the system size is N_{ts} cells and the following steps are performed:

1. Out of the set of N_{ts} cells pick up one parent cell i_p for reproduction.
2. Select the point (x_g, y_g) on the wall of a parent cell where the daughter cell is going touch it after successful reproduction.
3. Set the length of a new cell d to that of i_p, unless one considers the case of rods with varying length where d of a new cell is drawn from the distribution of lengths.
4. Randomly pick θ of a new cell, unless otherwise needed.
5. Place the daughter rod far from the parent cell, with its center-of-mass position $\mathbf{r} = (x, y)$ placed on the line going through (x_g, y_g) and the center-of-mass position of the parent cell $\mathbf{r_p} = (x_p, y_p)$.
6. Slide the daughter cell along the line going through (x_g, y_g) and $\mathbf{r_p} = (x_p, y_p)$ until it touches the parent cell at (x_g, y_g).
7. Check if the new cell does not overlap with other cells in the system.
8. If overlaps are present the reproduction process of i_p is unsuccessful and no daughter of i_p is added to the system.
9. Otherwise the cell is added to the system and is ready for further reproduction in the next Monte Carlo step.
10. Repeat the above steps N_{ts} times.

The algorithm ensures that on average every rod i_p attempts to reproduce once per simulation update. The update step dt defines the physical time of simulations as $t_{ph} = dt \times N_{ts}$, where N_{ts} gives the number of Monte Carlo steps per system update. The simulation is stopped after a suitable number of steps so that the interface width reaches steady state.

In order to define the interface and measure its width the dimension L perpendicular to the direction of growth is divided into n discrete segments of the unit length. Thus, for $L = M$ it gives $n = M$ segments $x_1, x_2...x_M$. All cells with the closest integer value of their x coordinate matching the x_{th} segment under consideration are checked for their height y, and the cell with the highest

value y is considered as the cell belonging to the interface. Thus, for $L = M$ there are M cells that make up the interface. Note that in case of overhangs, it is the highest cell that counts towards the interface. The average height and the interface width are calculated according to equations (2.1) and (2.2) respectively and are averaged over multiple independent simulations and for different system sizes L.

Program efficiency and optimization

The computational resources are the bottleneck in terms of performance and system sizes possible to simulate. For every update at time t_s the system size is N_{ts}. According to the Monte Carlo algorithm, every cell from the set of N_{ts} cells is, on average, picked up once for evaluation of its neighbourhood distances, overlaps and reproduction events. Since the system is off-lattice, one could pick up the cell, scan the whole system to find its closest neighbour and calculate the necessary distances and overlaps. However, this would require $N_{ts}(N_{ts}-1)/2$ iterations for N_{ts} cells at the every update step dt, and would quickly require very high computing power. Hence, in order to improve the program performance the continuous $L \times H$ space is divided into a discrete grid of square 'boxes' of the unit size, giving the total of $L \times H$ boxes. Every box in the grid keeps track of only these cells that match the box coordinates with their spatial coordinates. Thus, an additional list of neighbours is created and every cell can refer to the corresponding box for its neighbours. This reduces the number of iterations for every system update to N_{ts} as opposed to $N_{ts}(N_{ts}-1)/2$.

Note also that scaling in Eq.(2.4) requires $t \gg 1$ and is obtained in the $t \to \infty$ limit. For long simulations, the accessible RAM memory bottlenecks the number of cells that can be simulated. In order to reduce the necessary memory note that there is a limited number of agents that actively contribute towards the system growth. These agents form the growing surface (system interface) of the width $w(L,t)$. Recognizing this allows to reduce the number of agents simulated and after every $n_{res} \times dt$ simulation steps the inactive, non-reproducing bottom layer of the system can be removed from the program. During this optimisation step, the interface is evaluated for the cell that has the lowest y coordinate (call it y_l). Then, cells which do not belong to the interface and which have the y coordinate lower than y_l are removed from the system and computer memory. Thus, as the system approaches its steady state the amount of memory required

for simulation stops increasing and stays relatively constant due to a fixed value of $w(L,t)$. This enables one to simulate large systems that are necessary to obtain the value of the roughness exponent α. Moreover, in order to reduce the cost of computations associated with the interface growth, the measurement of its properties is performed only after every $n_{measure}$ simulation time steps.

2.4 Simulations

The system is initialized with a flat layer of rods and the growth geometry is such that cells grow in a rectangular simulation box of a base size L (see Fig. 2.1 for reference). Periodic boundary conditions that are applied in the horizontal direction ensure that the growth corresponds to that in the vertical tube. The initial rod orientation is θ_0 (along x-axis). However, the exact value of θ_0 should not affect the observed interface scaling as the memory of the system initial state is quickly lost due to random orientations of newly born cells. The length $d = 1$ for every rod, which adds up the total rod length of 1.5 (including $r = 0.25$ for both hemi-spherical caps). Various system sizes L are investigated to infer the values of exponents α and β. In order to save on simulation time, systems with large size L_{max} are simulated and then a running average is used to infer the scaling properties of smaller systems. The values of $w(L,t)$ for smaller L are calculated in windows of varying size w (such that $w < L_{max}$) that run over the system with the size L_{max}. The values of w are chosen such that they are the integer multiples of each other. Thus, for $L_{max} = 8192$ the smaller system sizes that are investigated have $L = 128$, $L = 256$, $L = 512$, $L = 1024$, $L = 2048$ and $L = 4096$ respectively. A track of interface widths is kept and the simulation stops only when $w(L,t)$ for the $L_{max} = 8192$ system reaches the steady state. To get the statistical significance of results a set of 30 independent simulations is run for $L_{max} = 8192$.

2.4.1 Numerical results for rods of equal length

In this section the results for simulations of the Eden model consisting of rods of equal lengths $d = 1$ with no spatial correlations are presented. The system sizes under investigation are: $L = 128$, $L = 256$, $L = 512$, $L = 1024$, $L = 2048$, $L = 4096$ and $L = 8192$. Fig. 2.3 shows the behavior of $w(L,t)$ against the mean

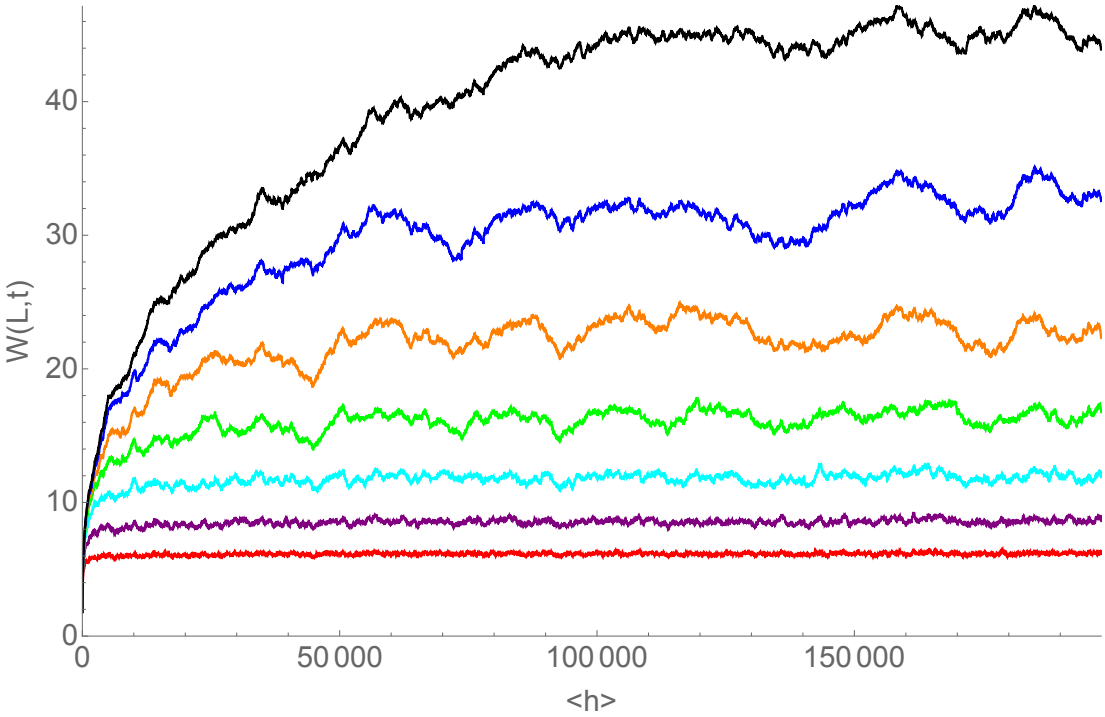

Figure 2.3 *Simulation results showing the interface width plotted against mean interface height (proportional to time). Colours correspond to different system sizes: L=128 (red), L=256 (purple), L=512 (cyan), L=1024 (green), L=2048 (orange), L=4096 (dark blue), L=8192 (black). Every plot is the average over 30 independent simulations. Two distinct regimes are seen in the plot, with the trend similar to that in Fig. 2.2. For larger system sizes random fluctuations in the interface width are present due to stochastic reproduction of cells at the growing front.*

interface height (i.e time). Every line in the plot is the average taken from 30 independent simulations. The trend in the plot is similar to that for symmetric agents in Fig. 2.2. Two distinct regimes that correspond to $w(L,t) \propto t^{\beta}$ at small t and settled down steady state $w(L,t)$ for much larger times are seen in Fig. 2.3. Due to stochastic reproduction of cells there are fluctuations in $w(L,t)$ visible in the steady state regime. Similarly to Fig. 2.2, the crossover time to steady state increases with L, indicating that it scales with the system size as L^z. Fig. 2.4 shows the log-log plot of data seen in Fig. 2.3 and clearly indicates the regime where the interface width scales as t^{β}. Plots for different L overlap with each other for very short times, showing the expected t^{β} scaling that is independent of L.

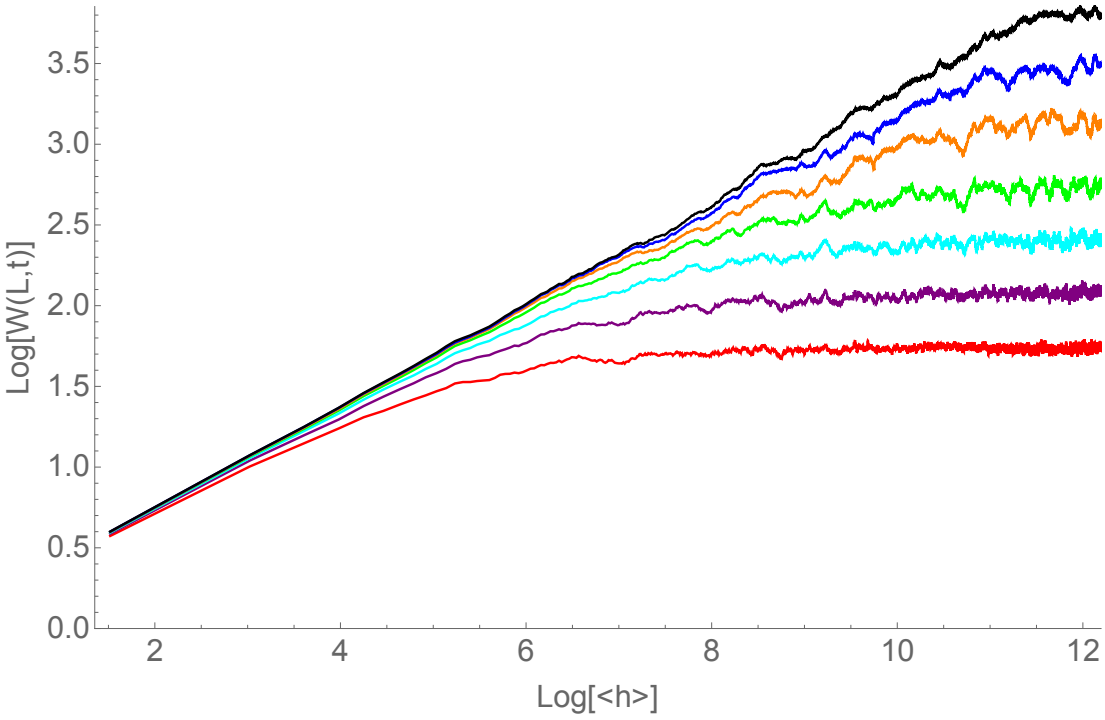

Figure 2.4 *The log-log plot of simulation data found in Fig. 2.3 shows that the $w(L,t)$ scaling in the small t regime is similar for all the system sizes.*

The growth exponent β

To obtain the value of β note that since $w(L,t) \sim t^{\beta} \sim \langle h \rangle^{\beta}$ then $\log(w(L,t)) \sim \beta \log(h)$. Thus, using a linear regression fit on the log-log data in the small t regime results in a straight line with the slope β.

System size L	β
128	0.236 ± 0.003
256	0.262 ± 0.004
512	0.275 ± 0.004
1024	0.281 ± 0.005
2048	0.284 ± 0.008
4096	0.292 ± 0.011
8192	0.303 ± 0.020

Table 2.1 *The table of β values obtained for simulations of different system sizes*

Table 2.1 shows the values of β obtained by linear regression through data averaged over 30 simulations for every L. For every L the bootstrap method was used to estimate the uncertainty in the average β [132]. The values in Table 2.1 are smaller than the $\beta = 1/3$ KPZ value, however, recall that the values of scaling exponents derived for the KPZ growth are obtained for system sizes

$L \to \infty$.

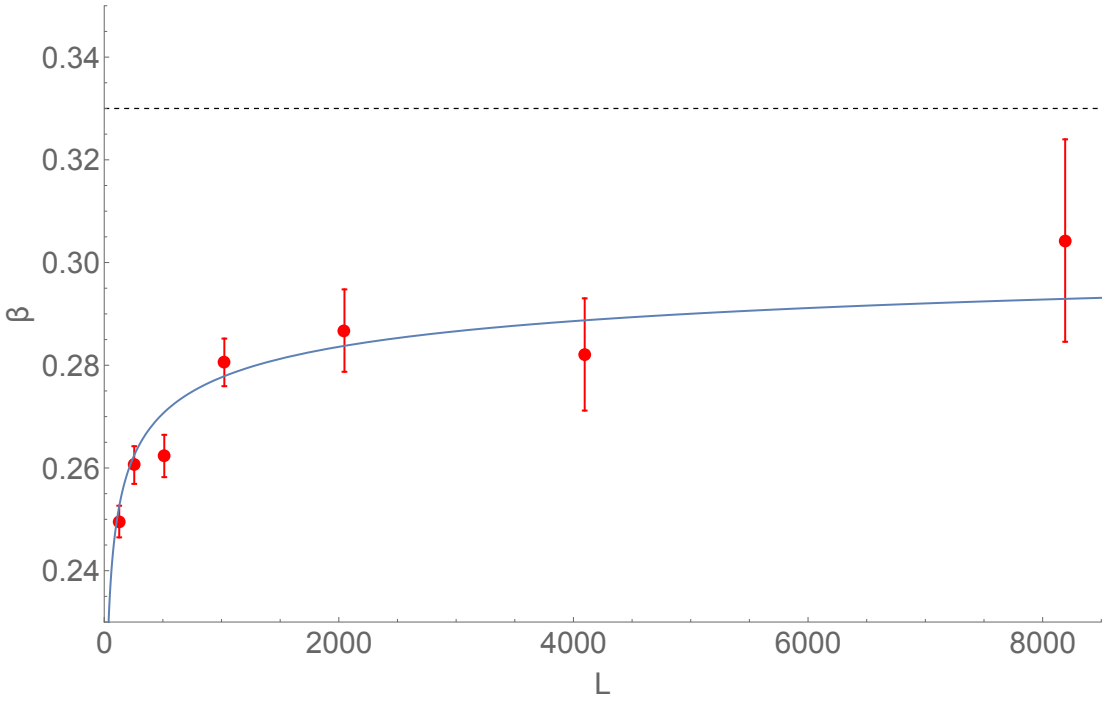

Figure 2.5 *Red data points correspond to the values of β in Table 2.1 that are found from the linear regression through the log-log data points in Fig. 2.2 in the small t regime. The blue line corresponds to $\beta(L) = 0.315 - 0.21/L^{0.25}$ fit through points in Table 2.1, with $\beta(L \to \infty) = 0.315 \pm 0.015$. Given the uncertainties in Table 2.2 the value lies close to $\beta = 1/3$ KPZ value marked with the black dashed line in the plot.*

Fig. 2.5 shows the values of β in Table 2.1 plotted against the L, with the trend where β increases with L. To obtain the limiting value of β when $L \to \infty$, the finite-size scaling method as used in [133, 134] to infer scaling exponents for large scale simulations is applied. Non-linear fitting function of the $\beta(L) = \beta_{L\to\infty} + A/L^c$ form is used through data points with error bars taken into consideration, see Fig. 2.5. After evaluation in Wolfram Mathematica (using the 'non-linear fit with weights' option) it results in coefficients of $\beta_{L\to\infty} = 0.315 \pm 0.015$, $A = -0.21 \pm 0.02$ and $c = 0.25$. Thus, $\beta_{L\to\infty} = 0.315 \pm 0.015$ is the limiting value when $L \to \infty$. Given the measurement uncertainty in $\beta_{L\to\infty}$, it is in good agreement with the KPZ value predicting $\beta = 1/3$. The blue dashed line in Fig. 2.5 shows the resultant fitting line through the simulation data points, approaching the theoretical black $\beta = 1/3$ KPZ line as the system size L increases. The plot hints that very large systems would be needed if one wanted to further evaluate the scaling numerically and approach the limiting value of β. However, given that the functional form $\beta(L) = 0.315 - 0.21/L^{0.25}$ captures simulation results and gives $\beta = 0.315 \pm 0.015$ in the $L \to \infty$ case, it is safe to conclude that β for simulated

systems in this section matches the KPZ value.

The roughness exponent α

To get the value of α, that is the scaling of $w(L,t)$ for large t, it is necessary to get the values of $w(L,t)$ for systems in their steady states, i.e the values of $w(L,\infty)$. The value of α can be obtained by the same method as in [133, 134]. Simulation system sizes L are set such that the i^{th} system size L_i is two times larger than L_{i-1}. Since at the steady state $w(L,\infty) \sim L^{\alpha}$ then the ratio of widths $w_i(L,\infty)/w_{i-1}(L,\infty)$ between L_i and L_{i-1} gives (Eq.2.9):

$$\frac{w_i(L,\infty)}{w_{i-1}(L,\infty)} = \frac{L_i^{\alpha}}{L_{i-1}^{\alpha}} = \frac{(2L_{i-1})^{\alpha}}{L_{i-1}^{\alpha}} = 2^{\alpha}. \tag{2.9}$$

System size L	$w_i(L,\infty)$	$w_i(L,\infty)/w_{i-1}(L,\infty)$
128	6.172 ± 0.309	-
256	8.591 ± 0.586	1.392 ± 0.008
512	11.907 ± 1.013	1.386 ± 0.011
1024	16.493 ± 1.751	1.385 ± 0.013
2048	22.980 ± 4.189	1.393 ± 0.032
4096	32.086 ± 6.274	1.396 ± 0.038
8192	45.045 ± 6.742	1.403 ± 0.034

Table 2.2 *The table of average steady state values of $w(L,\infty)$ obtained for simulations of different system sizes, with the third column giving the corresponding $w_i(L,\infty)/w_{i-1}(L,\infty)$ interface width ratios.*

Table 2.2 shows the steady state values of $w(L,\infty)$ obtained and averaged over 30 independent simulations, with the bootstrap method used to evaluate the measurement uncertainties. These values are used to obtain $w_i(L,\infty)/w_{i-1}(L,\infty)$ ratios found in the third column of Table 2.2, giving the set of points in Fig. 2.6. For the KPZ scaling the prediction is $\alpha = 1/2$ and so the value of ratios should approach $\sqrt{2} \approx 1.41$, which is indicated by the black line on the plot. Note that errors are significantly higher for larger values of L due to fluctuations in $w(L,\infty)$ getting larger for increasing L. To infer the limiting value of α when $L \to \infty$, the same method of finite size scaling as in the case of the β exponent is used. The non-linear fitting function of the form $w_i(L,\infty)/w_{i-1}(L,\infty) = w_{L\to\infty} + A/L^c$ is evaluated in Wolfram Mathematica. Here, $w_{L\to\infty}$ stands for $w_i(L,\infty)/w_{i-1}(L,\infty)$ when $L \to \infty$. The obtained values are $w_{L\to\infty} = 1.395 \pm 0.056$, $A = -1.011 \pm 0.004$

and $c = 0.9$. Given the value of $w_{L\to\infty}$ the limiting value of $\alpha_{L\to\infty}$ when $L \to \infty$ is obtained by noting that in the cases considered $2^{\alpha} = 1.395 \pm 0.056$. Thus, it gives $\alpha_{L\to\infty} = 0.481 \pm 0.04$ and given the measurement error it can be concluded that the roughness exponent α approaches the KPZ value when $L \to \infty$.

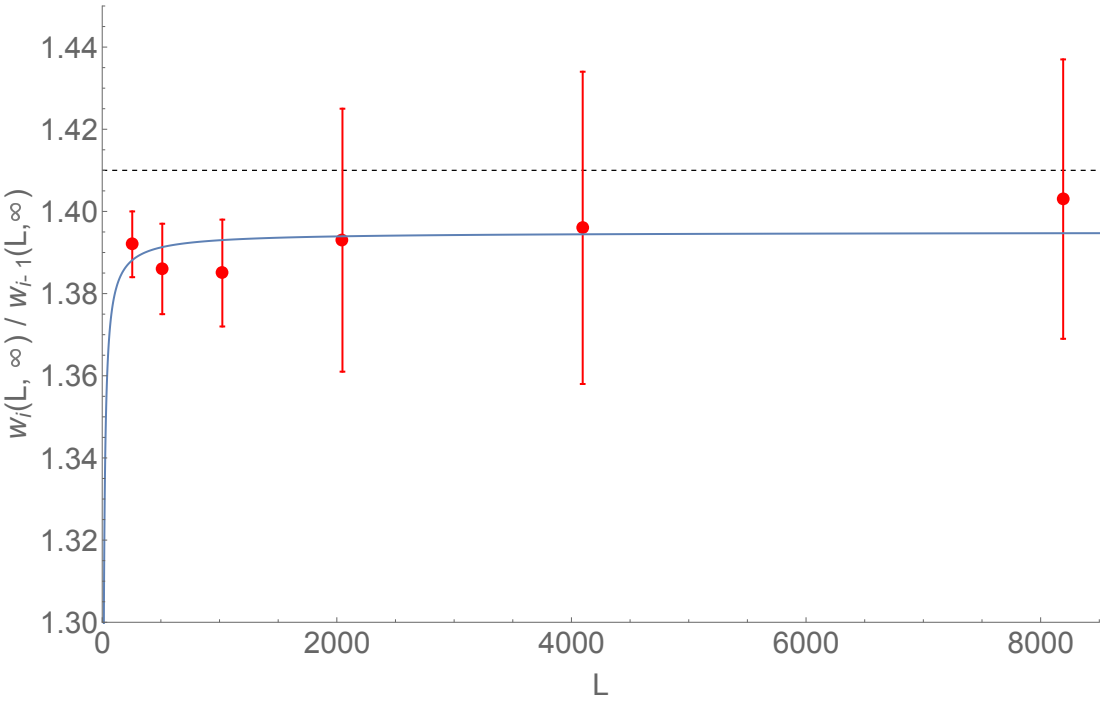

Figure 2.6 *Values of $w_i(L,\infty)/w_{i-1}(L,\infty)$ obtained from simulations (red data points), with the black line marking $w_i(L,\infty)/w_{i-1}(L,\infty) \approx 1.41$ which corresponds to the $\alpha = 1/2$ KPZ value. The fit function of the $w_i(L,\infty)/w_{i-1}(L,\infty) = 1.395 - 1.011/L^{0.9}$ form (blue) through data points results in $\alpha_{L\to\infty} = 0.481 \pm 0.04$ as $L \to \infty$, and hence the obtained roughness exponent is in a good agreement with the KPZ value.*

Finally, recalling the definition of the dynamic exponent $z = \alpha/\beta$ the numerical value obtained from simulations gives $z = 0.481/0.315 = 1.527 \pm 0.055$. It is in a good agreement with the KPZ value of $z = 3/2$. Thus, it is safe to conclude that the non-symmetric shape of reproducing cells in 2D off-lattice Eden model does not significantly affect the dynamic scaling of the growing interface.

2.4.2 The distribution of lengths and correlations in the rod spatial orientation

All cells in the previous section had the same length and their spatial orientations were random. This section aims to investigate the effect that the variation in length of cell and the correlations between cell directions have on the interface

scaling dynamics. There are two sets of independent simulations run, with the first set considering rods of varying length d and uncorrelated spatial directions. The initial configuration for simulations in this section is the same as in the last section: $\theta_0 = 0$ and $d = 1$ for all lined up cells at the bottom of vertical tube. However, the value of d for every newly born cell is drawn from the uniform distribution of lengths $d_{new} \in [0.5, 1.5]$ centered around $d_{mean} = 1$. Here, the length d of a newly born cell is uncorrelated with the length of the parent cell. Since $d_{mean} = 1$, the mid-point of the distribution corresponds to the value used in the previous subsection where all the cells are of equal length. This choice of parameters allows one to compare results for dynamic scaling exponents with the previous subsection and see whether the interface is affected by the varying value of d. The second set of simulations is run where the spatial orientation of the offspring cell is correlated with that of the parent. The orientation of a new cell is set to $\theta_{new} = \theta_{parent} + \theta_{correl}$, where θ_{parent} is the spatial orientation of the parent cell. θ_{correl} is the random angle increment drawn from the uniform distribution in the $\theta_{correl} \in [-\pi/8; \pi/8]$ range that determines the orientation of a newly born cell. Hence, the orientation of a new cell is correlated with the parent, with the additional random 'kick' due to the contribution from θ_{correl}. Note that smaller values of θ_{correl} result in more correlated cell directions. Simulation setup and the methods used to infer the interface scaling properties are the same as in section 2.4.1. For both cases there are 30 independent simulations run to obtain good statistical results.

The growth exponent β for the distribution of rod lengths

Fig. 2.7 shows the $\log(w(L,t))$ vs $\log(\langle h \rangle)$ plots for simulation data for rods of varying length. Similarly to Fig. 2.5 there are two distinct time regimes observed, one corresponding to $w(L,t) \propto t^{\beta}$ when t is small, and $w(L,t) \propto L^{\alpha}$ when t is large. The growth exponent β is extracted in the same way as in the previous section.

Performing the linear regression through $\log - \log$ data in the small t regime gives β values seen in Table 2.3. Similarly to previous cases, the bootstrap method is used to get the measurement uncertainty in β values.

Fig. 2.8 shows the data from Table 2.3 along with the fit function of the form $\beta(L) = 0.320 - 0.685/L^{0.479}$ marked in green. The limiting value of $\beta_{L\to\infty}$ is 0.320 ± 0.043 which is in good agreement with the KPZ scaling. Note that

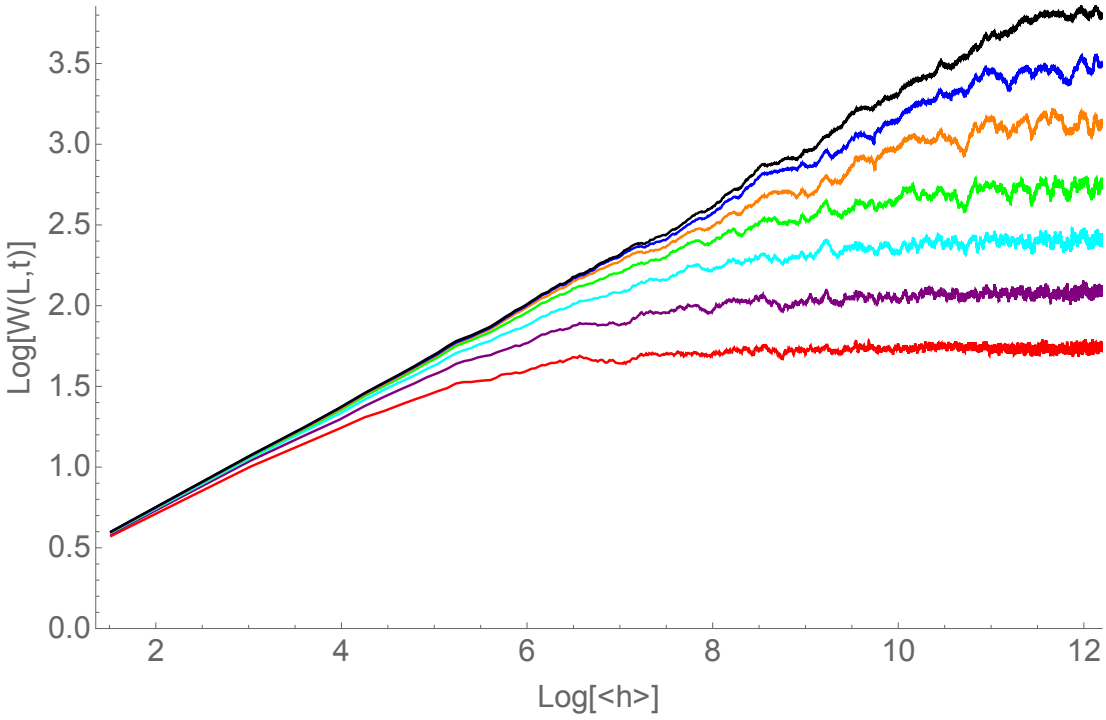

Figure 2.7 $\log(w(L,t))$ *vs* $\log(\langle h \rangle)$ *data plot averaged over 30 simulations. As in Fig 2.5 colours correspond to different system sizes. Similarly to Fig 2.5 there are two regimes observed with the same trends observed in both cases. Every plot is the average over 30 simulations.*

System size L	β
128	0.256 ± 0.003
256	0.265 ± 0.003
512	0.282 ± 0.004
1024	0.301 ± 0.004
2048	0.316 ± 0.008
4096	0.300 ± 0.011
8192	0.310 ± 0.012

Table 2.3 *The table of β values obtained for simulations of different system sizes with rods of varying length*

the green line in Fig. 2.8 lies a bit closer than the blue fit coming from the data points in Table 2.1, yet both fits go towards $\beta_{L\to\infty}$ values that, within the measurement error, fit the KPZ growth exponent. This leads to the conclusion that the variation in rod length does not affect the dynamic scaling in the small t regime.

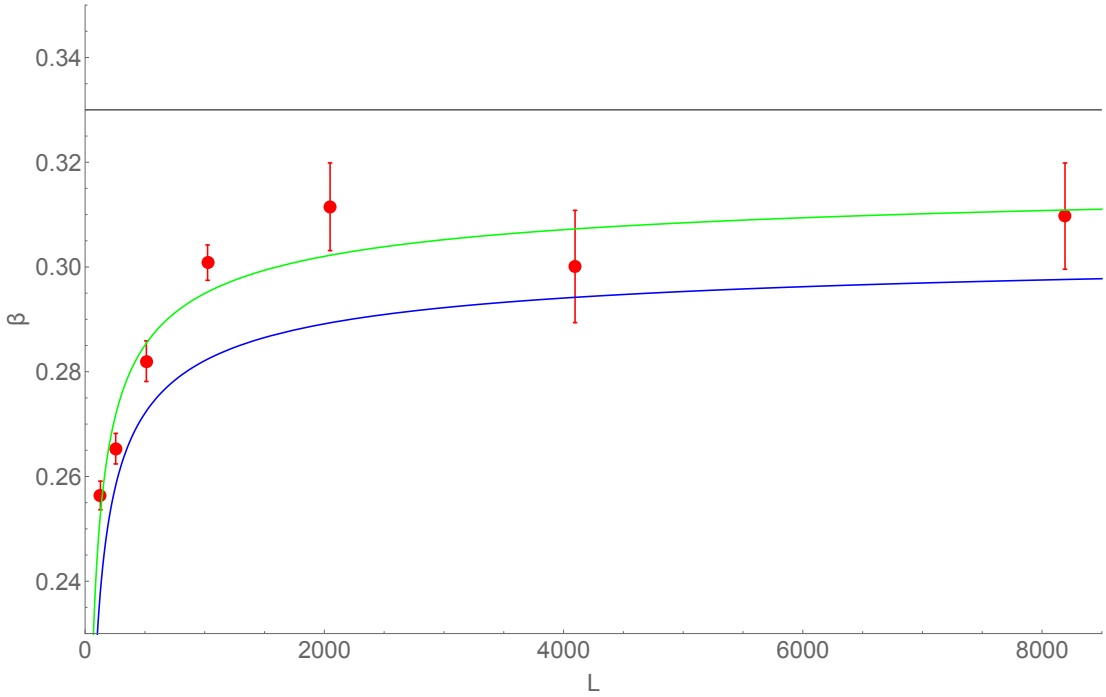

Figure 2.8 *Red data points correspond to values of β in Table 2.3 for the small t regime and the system consisting of rods of varying length. The green line represents the $\beta(L) = 0.320 - 0.685/L^{0.479}$ function that comes from fitting the points in Table 2.3. For $L \to \infty$ the value of $\beta(L \to \infty) \to 0.320 \pm 0.043$, which lies very close to the KPZ value $\beta = 1/3$ (black line in the plot). For comparison, the blue line corresponds to the $\beta(L) = 0.306 - 0.817/L^{0.514}$ fit obtained in the previous section and seen in Fig 2.5.*

The roughness exponent α for the distribution of rod lengths

To get the value of α, the same steps are performed as in the case of the growth of rods of uniform length. Steady state $w(L,t)$ values are obtained for each system size, and the corresponding $w_i(L,\infty)/w_{i-1}(L,\infty)$ width ratios are evaluated. Table 2.4 shows the obtained values, while Fig. 2.9 represents the plot of $w_i(L,\infty)/w_{i-1}(L,\infty)$ vs L_i.

As in case of Fig. 2.6, the $w_i(L,\infty)/w_{i-1}(L,\infty)$ values stay relatively close to the black $\sqrt{2} \approx 1.41$ line. The non-linear fitting function of the form $w_i(L,\infty)/w_{i-1}(L,\infty) = w_{L\to\infty} + A/L^c$ is applied to data points, giving the coefficients $w_{L\to\infty} = 1.409 \pm 0.039$, $A = -0.72 \pm 0.03$ and $c = 0.5$. Note that the values of coefficients A and c are different from these found in the previous case. The difference comes from the way Wolfram Mathematica algorithm deals with fitting internally, however the fit Fig. 2.9 is good and hence the resultant function returned by Wolfram Mathematica is reasonable. The obtained value

System size L	$w_i(L,\infty)$	$w_i(L,\infty)/w_{i-1}(L,\infty)$
128	7.059 ± 0.283	-
256	9.653 ± 0.512	1.367 ± 0.010
512	13.381 ± 1.117	1.386 ± 0.011
1024	18.589 ± 1.553	1.403 ± 0.018
2048	25.791 ± 4.398	1.387 ± 0.030
4096	35.834 ± 6.671	1.389 ± 0.027
8192	50.335 ± 6.515	1.405 ± 0.031

Table 2.4 *The table of average steady state values of $w(L,\infty)$ along with $w_i(L,\infty)/w_{i-1}(L,\infty)$ ratios obtained for simulations of different system sizes for rods of the varying length.*

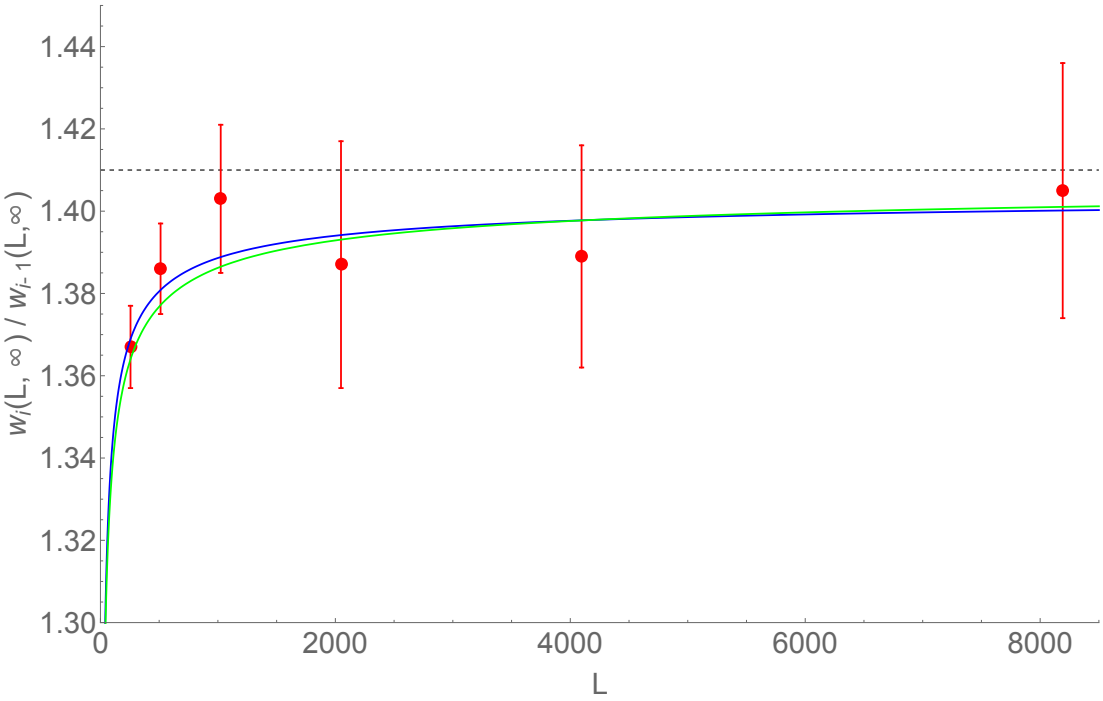

Figure 2.9 *Values of $w_i(L,t)/w_{i-1}(L,t)$ obtained for data from simulations for rods of varying length (red data points), with the black $\sqrt{2} \approx 1.41$ line that corresponds to $\alpha = 1/2$. The green line shows the non-linear fit of the form $w_i(L,\infty)/w_{i-1}(L,\infty) = 1.409 - 0.72/L^{0.5}$, which is very similar to the fit in case of rods of equal length in Fig. 2.6. The results show that the roughness exponent α is not affected by the variation in length of reproducing cells.*

$w_{L\to\infty}$ gives the roughness exponent $\alpha = 0.495 \pm 0.014$, which again fits the KPZ value. Given the value of $\beta = 0.320 \pm 0.043$ from the previous subsection the value of the dynamic exponent is $z = \alpha/\beta = 1.547 \pm 0.057$. Hence, the conclusion from simulations in this section is that the dynamic scaling of growing Eden interface is not affected by the variation in lengths of reproducing cells.

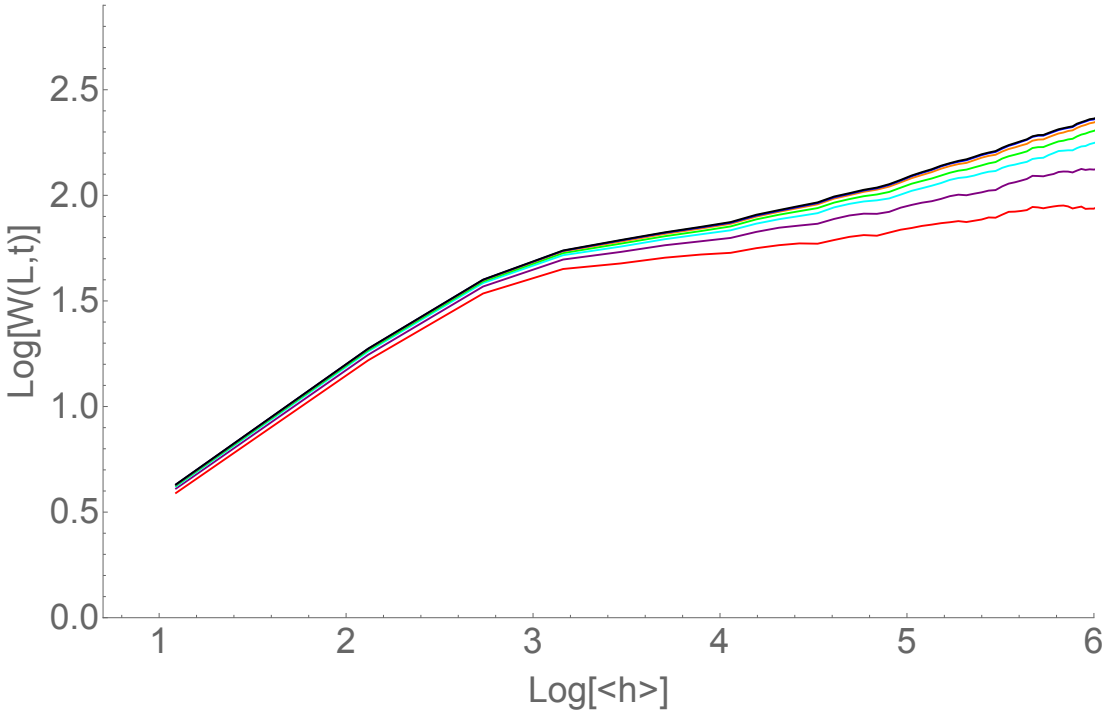

Figure 2.10 $\log(w(L,t))$ *vs* $\log(\langle h\rangle)$ *for rods with correlated spatial orientation* θ *with colours corresponding to different system sizes as in Fig 2.5. The data shown for small* t *indicates two regimes in low* t *with a more rapid increase in the front roughness for very low times, as opposed to Fig. 2.5.*

The $\log(\langle h\rangle)$ vs $\log(w(L,t))$ plots for small times for simulation data of rods with correlated spatial orientations is presented in Fig. 2.10. The time range on the plot is narrowed down to show that there is a characteristic change in scaling observed at small values of $\log(\langle h\rangle)$. This occurs due to the after effect of the initial configuration where all the rods have the same initial spatial orientation ($\theta_0 = 0$). Since the orientation of a new cell $\theta_{new} = \theta_{parent} + \theta_{correl}$, where $\theta_{correl} \in [-\pi/8; \pi/8]$ and is randomly picked during the system update, the random behavior of θ results in the correlation time t_{corr} that should decrease with θ_{correl}. Hence, starting from the initial configuration where θ_0 is the same for all cells one can expect three regimes as opposed to two observed in Figs. 2.5 and 2.7. First, there is a relatively short phase of the correlated growth where the memory of initial correlated orientation is retained. The phase then moves to the second regime that looks similar to that characterized by β in previous cases. For smaller θ_{correl} than the one used in Fig. 2.10 on might expect that the $\langle h\rangle$ for which the transition between phases occurs should be larger. This is indeed the case as seen Fig. 2.11 which shows the results for simulations performed

for $\theta_{correl} \in [-\pi/16; \pi/16]$, i.e half of that used in Fig. 2.10. One could now try and investigate the possible scaling relationship in the very small $\log(\langle h \rangle)$ range. However, the overlap of plots in both Fig. 2.10 and Fig. 2.11 in the very small $\log(\langle h \rangle)$ regime immediately suggests that the evolution of the interface width $w(L,t)$ is independent of the system size L. Moreover, as seen in plots the transition to the second regime occurs for similar values of $\log(\langle h \rangle)$ in all cases, further implying the non-existence of scaling with L. The value of θ_{correl} is the only parameter that affects this regime, with smaller θ_{correl} resulting in larger correlations and hence longer memory of the initial configuration that moves the transition point towards higher values of $\log(\langle h \rangle)$.

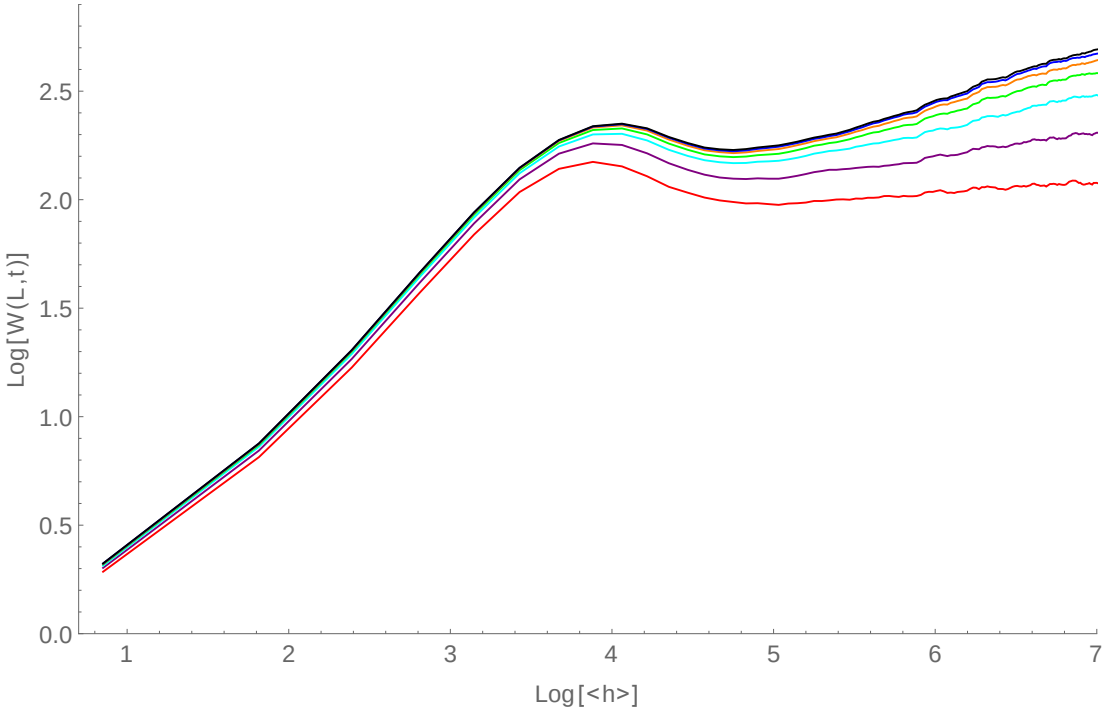

Figure 2.11 *The* $\log(\langle h \rangle)$ *vs* $\log(w(L,t))$ *plot for simulations where* $\theta_{correl} \in [-\pi/16; \pi/16]$. *Similarly to Fig 2.10 there are three regimes observed. The point of transition between the first and the second regime is related* θ_{correl}. *As seen in the plot, smaller* θ_{correl} *result in longer times for the transition to occurs.*

After the transition between the first and the second regime, the memory of initial configuration is lost. Given that, one could expect that after the transition point the $w(L,t) \sim t^{\beta}$ scaling for small t is retrieved. Thus, as in previous cases, the linear regression through the corresponding data points in Fig. 2.10 is performed. The obtained values of β along with the measurement error estimated with the bootstrap method are presented in Table 2.5.

Note that $L = 128$ and $L = 256$ are not included in Table 2.5. Only the first

System size L	β
512	0.215 ± 0.010
1024	0.258 ± 0.005
2048	0.278 ± 0.010
4096	0.296 ± 0.016
8192	0.301 ± 0.012

Table 2.5 *The table of β values obtained for simulations in the second regime seen in Fig. 2.10*

regime is observed for these sizes, since for these sizes the transition to the steady state occurs too fast to explore the t^{β} scaling. For sizes larger than $L = 256$ the finite size scaling can be used to infer the value of β for $L \to \infty$. The evaluation of the fitting function $\beta(L) = \beta_{L\to\infty} + A/L^{c}$ gives $x(L) = 0.311 - 15.149/L^{0.812}$, where for $L \to \infty$ limit $x_{L\to\infty} = 0.311 \pm 0.048$ and so the β KPZ growth exponent is retrieved.

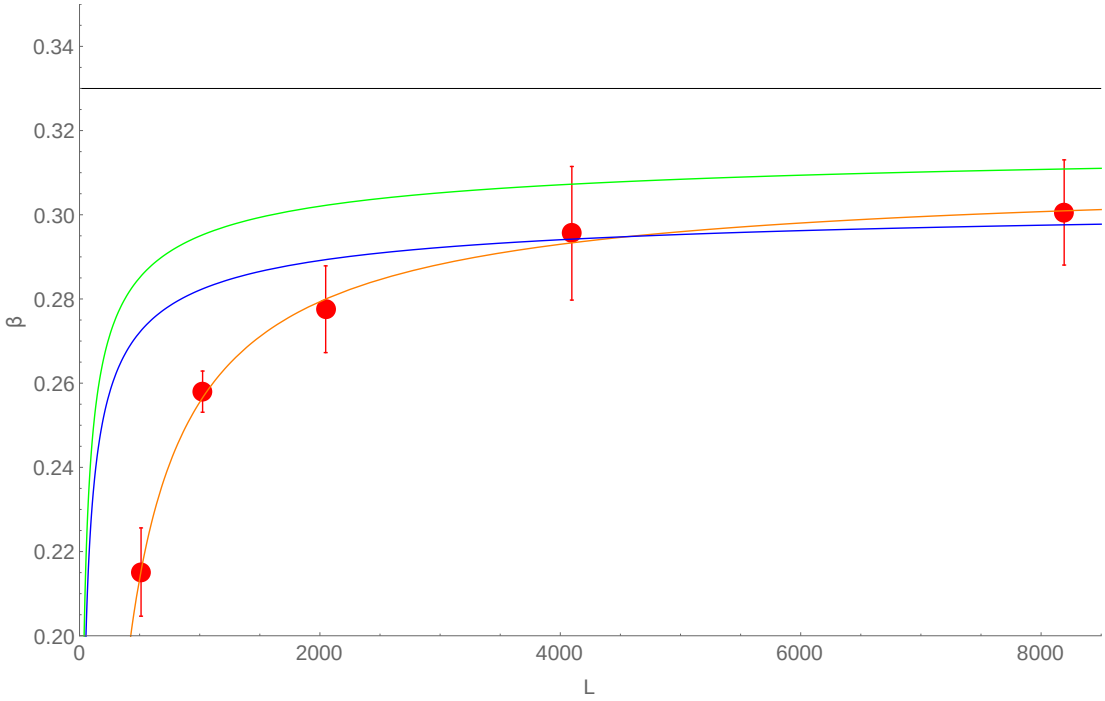

Figure 2.12 *Red data points correspond to the values of β in Table 2.5 found for the growth exponent in $t_{corr} < t \ll \tau$ regime for clusters with spatially correlated rods. The orange line represents $x(L) = 0.311 - 15.149/L^{0.812}$ fit that retrieves the β exponent for the KPZ model and fits the results obtained in the cases found in Fig. 2.8.*

Fig. 2.12 shows the obtained fit line (orange), plotted along the lines seen in Fig. 2.8. All three lines lie below the $\beta = 1/3$ black line for system sizes considered, however given the measurement error all three $\beta_{L\to\infty}$ values imply

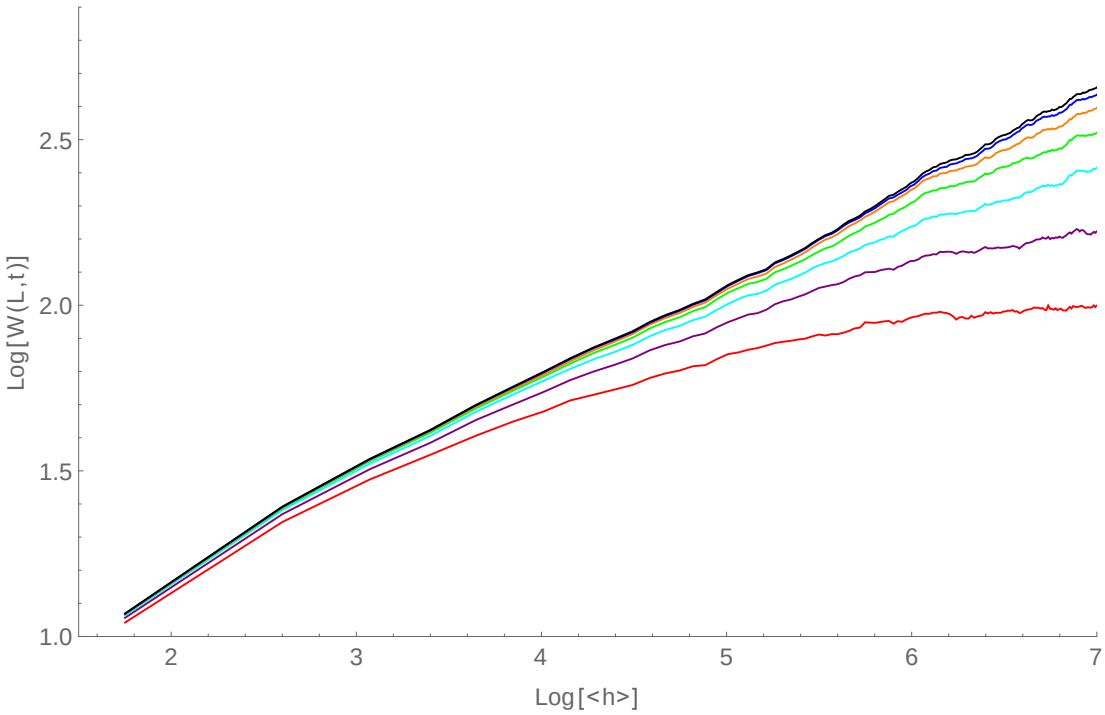

Figure 2.13 *The* $\log(\langle h \rangle)$ *vs* $\log(w(L,t))$ *plot for simulations of rods with correlated* θ *and random* θ_0*. As opposed to Fig. 2.10, only one regime for low* t *is observed and it corresponds to the small* t *regime seen in Fig. 2.5 which is characterized by the KPZ growth exponent.*

the KPZ scaling. Even though, in the case of the correlated growth, the initial growth is characterized by the regime of the non-universal behaviour, the system recovers the KPZ growth exponent β when the memory of the initial configuration is lost. For very small $\langle h \rangle$ the initial phase of interface growth is affected by the correlations due to θ_0 being non-random. However, for larger times this effect disappears due to stochasticity introduced in θ by random values of θ_{corr} at the every system update step.

The $w(L,t) \sim t^{\beta}$ phase is recovered only after the growth thermalizes due to random fluctuations in θ. Hence, one could expect that if θ_0 was random the thermalization will be achieved from the beginning of growth. In such cases, the first, non-universal phase in Figs. 2.10 and 2.11 should not exist. Indeed, this is the case as seen in Fig. 2.13 which represents small t results obtained with random initial orientation of cells θ_0. The normal scaling behavior that corresponds to the β exponent is observed for small times. The growth exponent in Fig. 2.13 is retrieved in the usual way by fitting the non-linear function through data points and gives $\beta_{L\to\infty} = 0.312 \pm 0.047$ which again corresponds to the KPZ scaling.

The roughness exponent α

To get the value of α for the case of correlated rods, the same steps as before are performed. Table 2.6 shows the obtained steady state values $w(L,\infty)$ and the corresponding $w_i(L,\infty)/w_{i-1}(L,\infty)$ width ratios. Fig. 2.9 represents the plot of $w_i(L,\infty)/w_{i-1}(L,\infty)$ vs L_i.

System size L	$w_i(L,\infty)$	$w_i(L,\infty)/w_{i-1}(L,\infty)$
128	6.812 ± 0.341	-
256	9.431 ± 0.631	1.384 ± 0.009
512	12.992 ± 1.102	1.378 ± 0.011
1024	18.003 ± 1.912	1.386 ± 0.014
2048	25.046 ± 3.982	1.391 ± 0.019
4096	35.044 ± 5.845	1.399 ± 0.023
8192	49.263 ± 6.237	1.405 ± 0.021

Table 2.6 *The table of the average steady state values of $w(L,\infty)$ obtained for simulations of different system sizes with rods correlated in space. The third column gives the corresponding $w_i(L,\infty)/w_{i-1}(L,\infty)$ interface width ratios used for evaluation of the roughness exponent α.*

The non-linear fitting function of the form $w_i(L,\infty)/w_{i-1}(L,\infty) = w_{L\to\infty} + A/L^c$ is applied to data points and is shown in Fig. 2.14. It gives the coefficients $w_{L\to\infty} = 1.401 \pm 0.039$, $A = 0.72 \pm 0.006$ and $c = 0.6$. The value $w_{L\to\infty}$ gives the roughness exponent $\alpha = 0.491 \pm 0.031$, which, as in previous cases, fits the KPZ value. Given $\beta = 0.312 \pm 0.047$ from the previous subsection the value of the dynamic exponent is $z = \alpha/\beta = 1.574 \pm 0.078$. This leads to the conclusion that after the memory of initial configuration is lost, the Eden growth with spatially correlated rods belongs to the KPZ universality class. Only for very small times the growth is affected by the spatial correlations of rods. Moreover, correlations in θ affect the initial phase of growth only when the initial state is such that rods are far from being disordered. For random initial configurations of rod orientations the system is thermalized and the small t growth regime is unaffected.

2.5 Discussion and summary

Simulations in this chapter have shown that the shape of the cell does not significantly impact the dynamic scaling of the growth interface in the 2D off-lattice Eden model. In all the cases considered here the growing front belongs

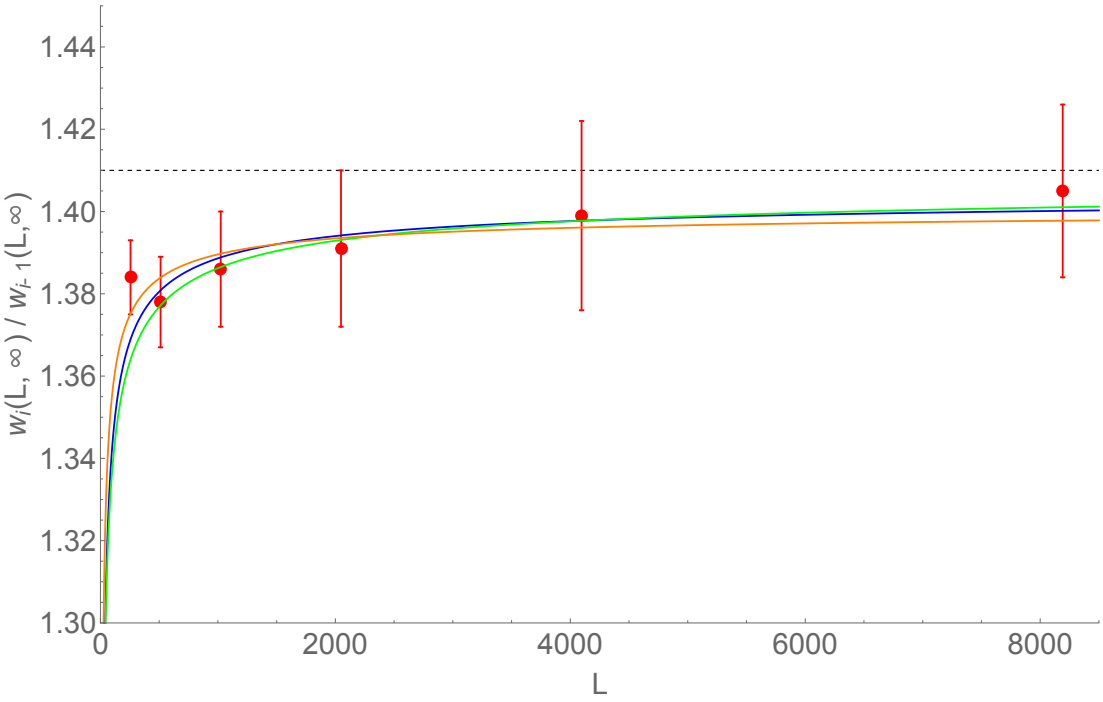

Figure 2.14 *Values of $w_i(L,t)/w_{i-1}(L,t)$ obtained for data from simulations for rods with correlated spatial orientations (red data points), with the black $\sqrt{2} \approx 1.41$ line that corresponds to $\alpha = 1/2$. The orange line shows the non-linear fit of the form $w_i(L,\infty)/w_{i-1}(L,\infty) = 1.401 - 0.72/L^{0.6}$, which is very similar to fits found before (green and blue plots). The results show that the roughness exponent α is not affected by rod correlations in space.*

to the KPZ universality class characterized by the scaling exponents $\alpha = 1/2$, $\beta = 1/3$ and $z = 3/2$. In the case where the spatial orientations of cells are correlated, there is a small effect in the initial phase of the growth observed. It arises due to the memory of initial state, however the effect is very quickly lost due to stochastic reproduction of cells and the thermalization of the system.

Recall that the Eden model had been originally developed to study the statistical physics of microbial communities and the results of this chapter indicate that the roughness of the expanding microbial colony front might not be significantly affected by the exact shape of the cell. However, such extrapolation to the real world entities is dangerous as the simplicity of the cell reproduction in the Eden model does not capture complex interactions and mechanics that give rise to the microbial colony morphology. The only interaction in the Eden model is due to space-exclusion, and as discussed in the introductory chapter of this thesis, the biomechanical interactions of cells in real colonies are the vital component that contributes to colony morphology. Laboratory studies on the spatial structure of colonies in [135] suggest that the shape of a cell affects the way cells diffuse in

space. The spatial structure of a colony is shown to be significantly different due to shape differences between rod-like *E.coli* and spherical *S.cerevisiae* cells.

In the cases considered in this chapter the active (i.e. reproducing) front width is confined to the periphery of the cluster. Only a narrow strip of cells with free space around them are reproducing while the bulk of the cluster is effectively 'frozen'. As discussed in the next chapter, nutrient diffusion in the growing microbial colonies is such that the active layer of growing and mechanically interacting cells can be wider than the narrow strip observed in the Eden model. Hence, in such case the bulk of the colony becomes the active contributor towards the observed features of the growing cluster. Due to a larger front width the interactions between cells in the expansion front could affect its roughness and hence impact the observed dynamic scaling.

Simulations of growing microbial colonies indeed indicate that the α exponent might be different and depends on the colony growth conditions which in turn define the width of the growing layer. The details of the algorithm used for these simulations are fully described in the later Section 3.4 of this thesis. Cells grow in a vertical tube, consume nutrients, divide, mechanically interact with each other and give rise to the spatially structured cluster. By varying the nutrient concentration and/or the rate of nutrient consumption by cells, the number of bacteria in the active state of growth can be changed and as a result, the active layer of growth (i.e front) can be of a different width. Simulations with two different nutrient concentrations are used to check the scaling coefficient α for two different widths of growing fronts. In both cases, the maximum linear dimension of the growth tube $L_{max} = 5000$ and enough growth time is given ensure the proper thermalization of the system. Running average for windows of a varying size L is used to measure the width $w(L, \infty)$ as a function of L.

Figure 2.15 shows the $w(L, \infty)^2$ vs L plot for $t \gg 1$ limit for the case of the narrow front (i.e low nutrient concentration in simulations of growing colonies), which in turn corresponds to the Eden model. The resulting plot in Fig. 2.15 is a straight line, leading to the conclusion that $w(L, \infty) \sim L^{1/2}$ and hence $\alpha = 1/2$ which corresponds to the KPZ universality class.

In contrast, as the nutrient concentration is increased the expansion front gets wider and the scaling of the interface width is different. Fig 2.16 shows that the $w(L, \infty)^3$ vs L plot results in the straight line and implies the roughness exponent $\alpha = 1/3$. Hence, a wider front results in the large t scaling that does not

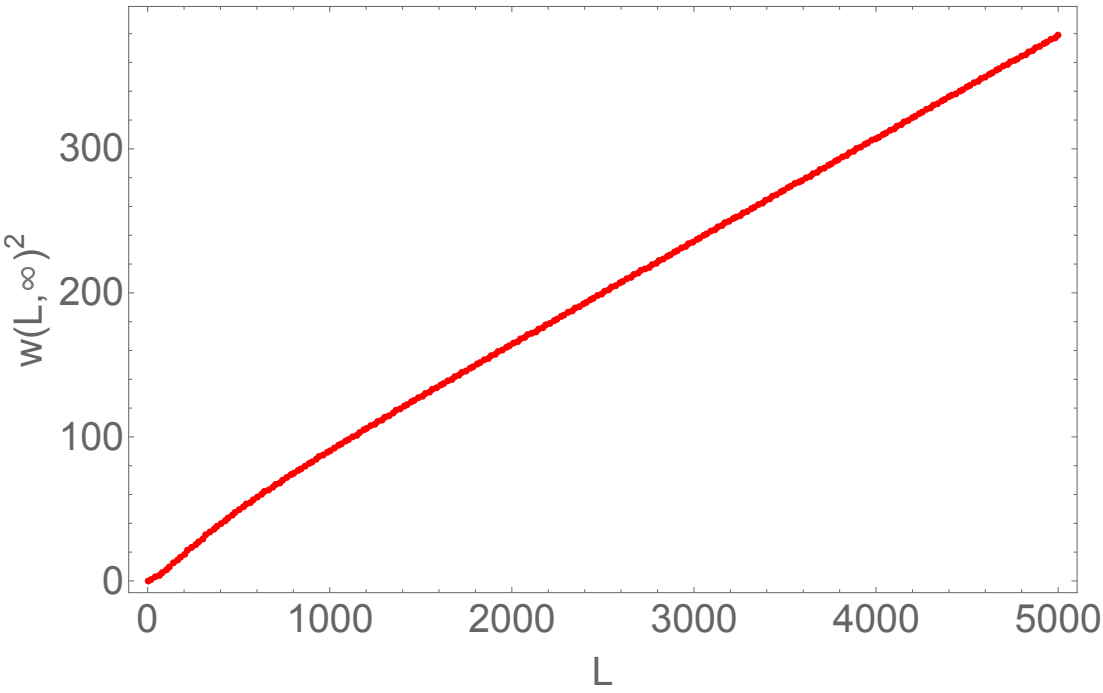

Figure 2.15 *For simulations of growing microbial colonies, low nutrient concentration and high nutrient consumption rate by cells results in a narrow layer of actively growing cells at the expansion front. This is a case similar to the narrow growing interface in the Eden model considered in this chapter. The* $w(L,\infty)^2$ *vs* L *plot results in the straight line that implies the value of the* $\alpha = 1/2$ *exponent that corresponds to the KPZ scaling.*

correspond to the KPZ universality class. Since α is smaller, the roughness of the interface is smaller when the nutrient concentration is high and the resultant front width is larger. Further evaluation of the impact of nutrient concentration on the front roughness and the resulting colony structure can be found in subsection 3.6.1 in Chapter 3. Observations such as those in Fig 2.16 highlight the fact that new factors become relevant when one moves from the simple Eden model to a more detailed way of modeling the microbial community growth. To account for these and to study other properties of growing colonies in more detail, one needs a more complex simulation framework such as the one developed in the next Chapter 3.

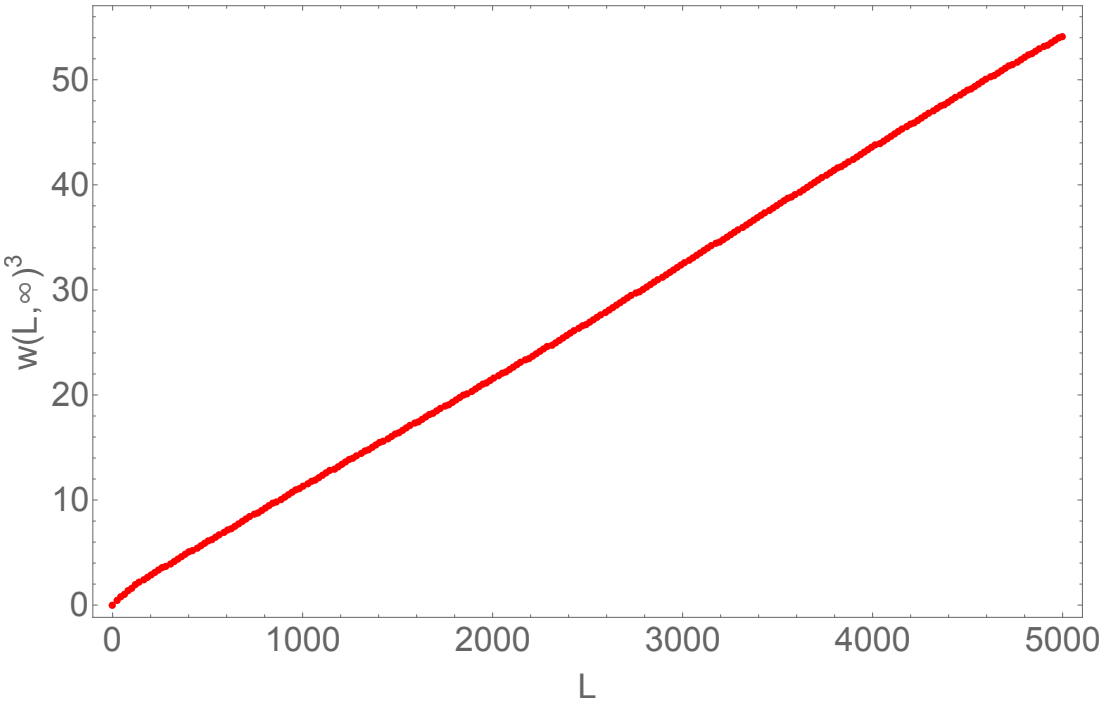

Figure 2.16 *As opposed to Fig. 2.15, larger nutrient concentrations give wider front that results in non-KPZ scaling of the interface in the* $t \gg 1$ *limit. The* $w(L,\infty)^3$ *vs* L *plot results in the straight line that implies the* $\alpha = 1/3$ *exponent that is different from that corresponding to the KPZ scaling.*

Chapter 3

Plasmid conjugation in 2D spatially structured microbial colonies

Results in the previous chapter show that dynamic scaling of the Eden model is not significantly affected by the shape of the reproducing cells. However, the lack of physical and biological details makes this model not accurate enough for a more detailed study of microbial growth. It has been noted in the previous section that nutrient concentration and cell-cell interactions can affect the width of the expansion front and hence the roughness of the colony interface. As discussed further in this chapter, spatial and genetic structure of the colony are further affected by physical details of interactions between cells that constitute the expansion front. This chapter extends the simple, Eden-like approach of computational modelling of the 2D cluster growth towards a simulation framework which includes physical interactions between rod-shaped cells and their environment. As it is discussed later in this chapter, the colony growth that results from these interactions drives the evolution of genetic diversity of expanding colony, since the emergent roughness of the colony expansion front becomes an important factor contributing to the genetic structure of the population. The study in this chapter is motivated by works by Oscar Hallatschek [113, 114, 135], who studied the expansion and genetic diversity of microbial populations, as described in later sections. Inspired by the omnipresence of plasmids in natural habitats and their contribution to the pool of genes, the work in this chapter extends studies in [113, 114, 135] by adding plasmid conjugation between cells. The implementation of horizontal gene transfer by plasmid conjugation into the computational model developed in this chapter will

allow one to study its effect on the genetic structure of microbial colonies, and contributes an important step towards better understanding of phenomena that drive the adaptation dynamics of microbial communities.

3.1 Spatial structure and genetic diversity

In a well-mixed culture, every cell experiences the same surroundings and conditions. The mixing of cells results in no spatial patterns that can be observed in a generic diversity of bacteria. On the other hand, the surface confinement of a growing bacterial colony reduces the number and range of possible interactions between cells. This gives rise to interesting genetic structures and patterns, as observed by Hallatschek et al in [113], who used growing *E.coli* colonies to study the genetic structure of populations during 2D spatial expansions. The observation was that when CFP-labeled and YFP-labeled and otherwise genetically identical individuals are allowed to reproduce and expand into a circular colony, the population segregates into domains of reduced genetic diversity as seen in Fig. 3.1.

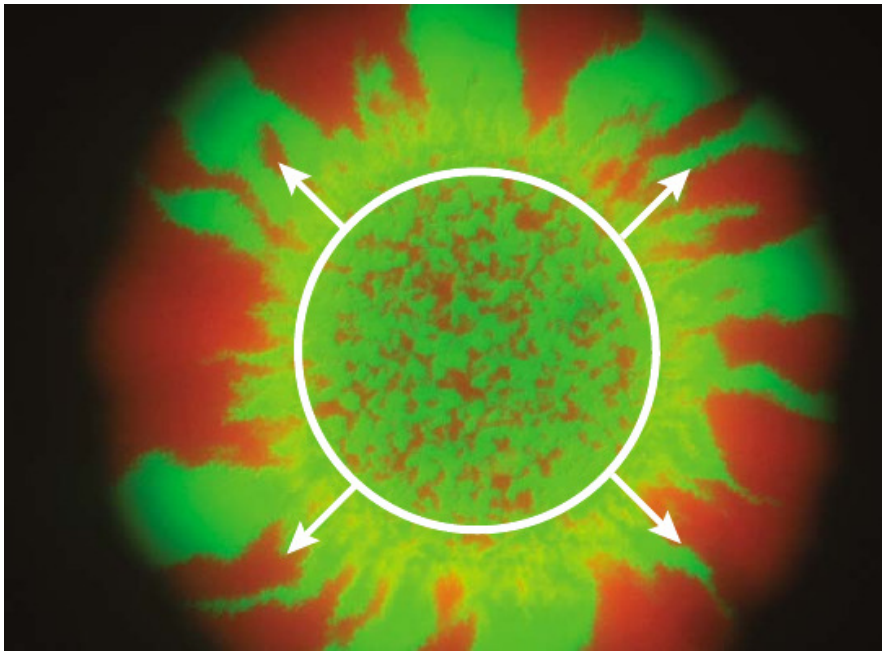

Figure 3.1 *The population of genetically identical cells (except for colour labeling) segregates into domains of reduced genetic diversity when allowed to grow on a solid agarose infused with nutrient broth. (Image source: [113])*

As the nutrient becomes depleted in the center of the colony due to consumption by bacteria, only a narrow layer of bacterial cells (called the 'founder' or 'pioneer'

population) at the expansion front contributes to the spatial population expansion into uninhabited space. This reduces the effective population size significantly and the pool of genes that are found in new population is limited. Since the effective population is small, chance effects in cell reproduction become important. Some cells can have, by pure chance, a few more offsprings that can then become founders of new generations. When the population is large, the law of large numbers causes the effect of such changes in the gene frequency due to random sampling (called 'genetic drift' [136]) to be small. However, for small populations this genetic drift becomes one of the major factors affecting the genetic structure of the colony. This genetic drift together with spatial displacements of cells lead to the emergence of sectors of genetically related bacteria separated by domain walls, as seen in Fig. 3.1. Domain walls between sectors exhibit the quasi-diffusive behavior. The experimental data in [113] shows that the mean square transverse (i.e. perpendicular to the radial direction of colony growth) displacement $\langle \Delta X_{tip}^2 \rangle$ of the tip of the domain wall at the expansion front scales as:

$$\langle \Delta X_{tip}^2 \rangle \sim L_{walk}^{2\xi} \tag{3.1}$$

where L_{walk} gives time and $\xi = 0.65 \pm 0.05$ is the wandering exponent indicating the super-diffusion of domain walls. Two domain walls annihilate when meeting at the expansion front, see Fig. 3.2. As seen in the figure, at the annihilation point two sectors of the same colour merge and no domain wall between them is left. A different case scenario would happen if the two merging sectors were of a different colour. In such a case, two domain walls at the annihilation point would coalesce into one. In both cases, cells constituting for the entrapped sector behind the annihilation point do not give rise to new pioneers and the population heterogeneity (that is, the probability that two cells picked from two different sites in population will be genetically different) decreases.

The observed behavior of domain walls is related to statistical properties of the growing interface. For example, rough fronts lead to more 'wandering' of sector domain walls, whereas smooth fronts cause the sectors to look more straight. As seen in Fig. 3.3, the net motion of the domain wall is tilted at the expansion front. A simple geometric argument as in [113] can be used to estimate how the front roughness contributes to sector wandering.

Hallatschek considers a short segment of the colony expansion front, as seen in Fig. 3.3. Such approximation arises due the fact that the circular expanding

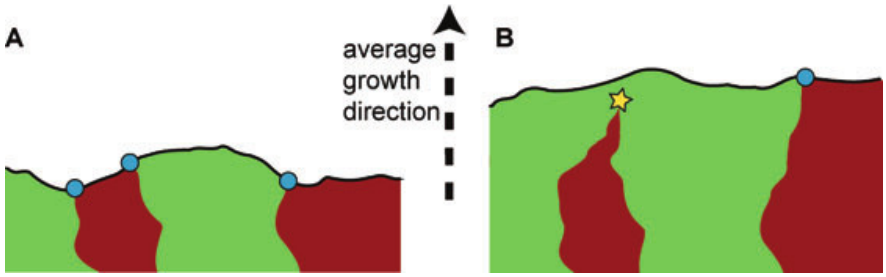

Figure 3.2 *Random behavior of two domain walls. When their tips meet they coalesce and the sector becomes entrapped behind the expansion front. Bacterial cells in such a sector do not give rise to new pioneer cells. (Image source: [114]).*

front does not have a fixed size L that would set the limit for the amplitude of fluctuations, as it is the case for the flat front considered in the previous chapter. Hence, the segment of the front in this sections under consideration is subject to stochastic shape fluctuations of amplitude h that arise on a somehow artifically set length-scale λ. Similarly to the discussion in Chapter 2 for the Eden model, the amplitude of fluctuation scales with the system length-scale as $h \sim \lambda^{\alpha}$. The fluctuation arises during time t and hence, its amplitude scales with time as $h \sim t^{\beta}$. Thus, $h \sim t^{\beta} \sim \lambda^{\alpha}$ and so $\lambda \sim t^{\beta/\alpha}$. The motion of domain walls is biased, with the angular deviation (tilt) of a small section of the front being $\sim \frac{h}{\lambda}$, as seen in Fig. 3.3. As $h \sim t^{\beta}$ and $\lambda \sim t^{\alpha/\beta}$, then after substituting both of these expressions into $\sim \frac{h}{\lambda}$ the tilt angle of the front undulation becomes $\propto t^{\beta(\alpha-1)/\alpha} \sim t^{(\alpha-1)/z}$, where $z = \alpha/\beta$ is the dynamic exponent. Hence, by integration with respect to time, this shows that transverse displacements of sector domain walls scale like $t^{1+(\alpha-1)/z}$, implying the wandering exponent $\xi = 1 + (\alpha - 1)/z$. The Eden model values from the previous chapter are $z = 3/2$ and $\alpha = 1/2$, which after substitution give $\xi = 2/3$. This is in agreement with the experimentally obtained exponent $\xi = 0.65 \pm 0.05$ in [113] and suggests that microbial colonies in the case considered there are in the KPZ universality class. However, this has not yet been confirmed by direct measurements of α and β exponents.

The mathematical methods of annihilating random walkers can be used to treat the problem mathematically [114]. As discussed, the motion of domain walls is super-diffusive. However, the qualitative behavior of the domain wall motion can be explained by using a simpler mathematical diffusion model. Consider a neutral case where all cells have the same fitness (i.e reproduction rate) and the front is linear and of fixed length, as seen in Fig. 3.4a. The distance between two domain walls is $X(r)$, which is a continuous variable that is changing due to the random motion of the domain walls. For the front advancing from r_0 to r the

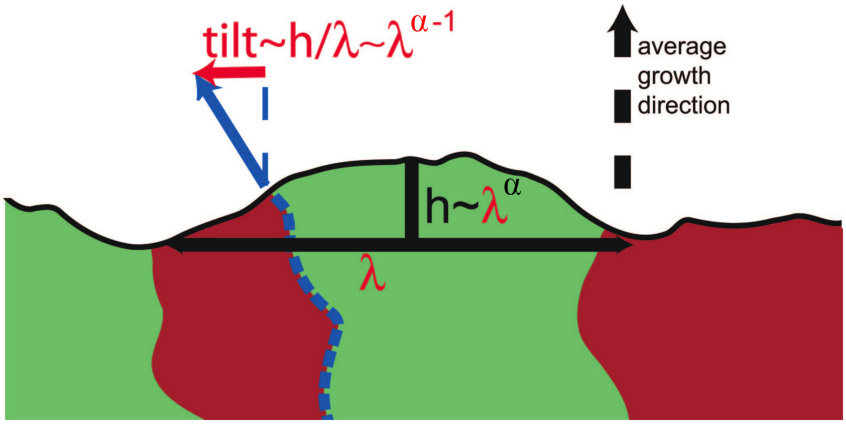

Figure 3.3 *The roughness of the expansion front results in the tilt (red) in the domain wall motion (blue). Black arrow indicates the radial direction of colony growth. The amplitude h of the roughness fluctuation is set by the length-scale λ and the roughness exponent α. (Image modified after: [113])*

value of $\Delta X = X(r) - X(r_0)$ behaves as $\langle \Delta X \rangle = 0$ and $\langle \Delta X^2 \rangle = 4D_x \Delta r$. The diffusion coefficient $D_x = const$ describes the random motion of a single domain wall. There are two domain walls that account for one sector of size $X(r)$ and so the factor of 2 arises in the expression for $\langle \Delta X^2 \rangle$. The radius increment is $\Delta r = r - r_0$ and since for both linear fronts and circular 2D colonies the radius is observed to increase, within a good approximation, proportionally with time [135] then $\Delta r \propto t$. Now, for the circular colony growth seen in Fig. 3.4a the colony perimeter expands in time and so the angular distance between two domain walls increases. The sector domain size is given by its angular size $\Phi(r)$. As in the case of the linear front, the domain size changes randomly due to random motion of the domain walls when the front advances from r_0 to r. Thus, $\Delta\Phi(r) = \Phi(r) - \Phi(r_0)$ is characterized by $\langle \Delta\Phi(r) \rangle = 0$ and $\langle \Delta\Phi(r)^2 \rangle = 4D_\phi \Delta r$, where D_ϕ is the angular diffusion coefficient. The linear distance between two domain walls on the circular expansion front can be expressed in terms of the angular distance between them, with $\Delta\Phi(r) = \Delta X(r)/r$. This can be substituted into the expression for $\langle \Phi(r)^2 \rangle$ and rewritten for $D_\phi = \langle \Delta\Phi(r)^2 \rangle / \Delta r = \frac{\langle \Delta X^2 \rangle / r^2}{\Delta r}$, which after taking the $\Delta r \to 0$ limit gives $D_\phi = D_x / r^2$. Hence, D_ϕ is expressed in terms of the linear diffusion coefficient D_x. Note the factor $1/r^2$ which arises due to linear expansion of the perimeter of the colony.

The diffusion framework allows one to make predictions about the number of sectors in the colony. A sector arises at time r_0 from two domain walls starting close to each other on the expansion front. Domain walls annihilate when they meet, however the probability of annihilation quickly decreases with an increasing

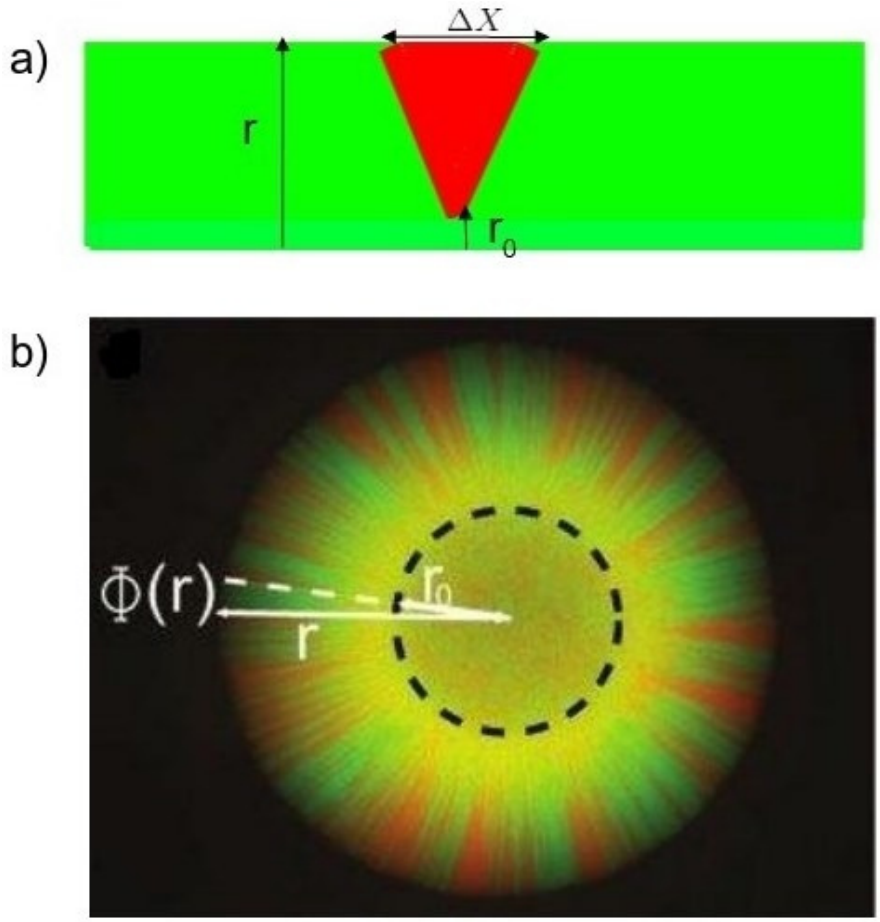

Figure 3.4 *a) For a linear front of fixed length the sector domain can be described by the change in distance between two corresponding domain walls b) For a circular growth the sector domain is described by the angle $\Phi(r)$ measured between two domain walls. For both cases the diffusion of domain walls randomly changes the distance between them.*

distance between walls. The number of sectors is defined by the set of random walkers that avoid annihilation at $r > r_0$. The sector size $Z(r)$ (with $Z(r) = X(r)$ for linear and $Z(r) = \Phi(r)$ for circular expansion) is a continuous variable, and so its statistical properties can be described by a diffusion equation. Let $F(z, r|z_0, r_0)$ be the probability of finding sector of size $Z(r) = z$ when the expansion front is at r, given that the size at the earlier moment r_0 was $Z(r_0) = z_0$. The diffusion equation for the evolution of $F(z, r|z_0, r_0)$ is then:

$$\frac{\partial F(z, r|z_0, r_0)}{\partial r} = 2D(r)\frac{\partial^2 F(z, r|z_0, r_0)}{\partial z^2} \tag{3.2}$$

with the boundary conditions $\lim_{z\to 0^+} F(z, r|z_0, r_0) = 0$ to account for annihilation of two domain walls. Consider the infinite allele scenario, which is the case

where every cell of the founder population at r_0 is of a different colour. Eq.(3.2) can be solved with the use of a method of images and allows one to obtain the expression for the sector size distribution $P(z, r|r_0)$, that is the probability of finding the sector of size z when the colony size is r:

$$P(z, r|r_0) = \frac{z}{\sigma(r, r_0)^2} \exp^{(} \frac{-z^2}{2\sigma^2_{r,r_0}}) \tag{3.3}$$

with $z \geq 0$ and $\sigma(r, r_0)^2$ being the total standard deviation that is accumulated by the variable $Z(r)$ when the front advances from r_0 to r. The expression for $\sigma(r, r_0)^2$ can be evaluated for both linear and circular front by noting that $\sigma(r, r_0)^2 = 4\int_{r_0}^{r'} D(r')dr'$, which for linear inoculation gives $\sigma(r, r_0)^2 = 4D_x(r - r_0)$ and for the circular front $\sigma(r, r_0)^2 = 4D_x(r_0^{-1} - r^{-1})$. Note that for the circular growing front $0 \leq z \leq 2\pi$ and so Eq.(3.3) is valid in the $\sigma \ll 1$ limit only. The average sector size $\langle Z(r|r_0)\rangle$ expected when the front advances from r_0 to r corresponds to the mean of distribution in Eq.(3.3):

$$\langle Z(r|r_0)\rangle = \sqrt{\frac{\pi}{2}}\sigma(r, r_0). \tag{3.4}$$

Thus, the expected number of sectors for a front of length L is $\frac{L}{\langle Z(r|r_0)\rangle}$. After substituting $\sigma(r, r_0)^2 = 4D_x(r - r_0)$ for the linear front the expected number of sectors $N(r|r_0)_{lin}$ is:

$$N(r|r_0)_{lin} = \frac{L}{\sqrt{2\pi D_x \Delta r}} \tag{3.5}$$

where $r = r_0 + \Delta r$. Hence, the average sector number for the linear inoculation depends on the front length L and time r from the initial r_0. Eq.(3.5) implies that $N(r|r_0)_{lin}$ does not depend on any details of individual cells and the initial sector size, as long as the initial number of sectors is sufficiently large. For circular inoculation, note that when $r \to \infty$ then $\sigma(r, r_0) = 2\sqrt{D_x/r_0}$, and noting that $L = 2\pi r$ for circular inoculation the number of sectors in the $r \to \infty$ limit $N(\infty|r_0)_{circ}$ is:

$$N(\infty|r_0)_{circ} = \sqrt{\frac{2\pi r_0}{D_x}}. \tag{3.6}$$

Thus, the number of sectors during circular growth is expected to become fixed for large colony radii. The expected number of sectors depends on r_0 and $N(\infty|r_0) \propto r_0^{1/2}$, and so for larger initial habitat sizes one expects more sectors when $r/r_0 \gg 1$.

Finally, note that the above derivations assumed the infinite allele model, i.e. every sector is of a different colour. Given that there are only two types of sectors (for example green and red as seen in Fig. 3.1), there is a probability of 1/2 that two neighbor sectors are of the same colour. Due to this, the number of sector domain walls is half of that expected for the infinite allele case. To account for this, the expressions for $N(r|r_0)_{lin}$ and $N(r|r_0)_{circ}$ obtained above need to be multiplied by the factor of 1/2 in both cases.

It is worth to note that it is possible to study the genetic diversity (quantified previously by the number of sectors) in a different way. Korolev et al. [137] extended the stepping-stone model of growing populations (developed in [138] for well-mixed populations) to a higher dimension and considered the additional contributions from the colony spatial structure and correlations. Korolev has shown that in the neutral case the average genetic diversity $H(t, x)$ (here defined as the average probability of sampling two different species, picked up at time t, from locations separated by distance x) for the linear expanding front evolves in time as $t^{-\frac{1}{2}}$. This is the same time dependence as found in Eq.(3.5) (because $\Delta r \propto t$ in that case). Moreover, both approaches in [113] and [137] show that for the limiting case $t \to \infty$ the genetic diversity goes to zero.

Natural selection

The above discussion applies to neutral evolution, i.e all the species grow at the same rate. In non-neutral case, different bacterial strains have different growth rates. For well-mixed populations Lotka-Volterra interactions [139] are usually adapted to describe evolutionary dynamics of the population. They predict the existence of several equilibrium points which correspond to the survival of one species only or the coexistence of species at some critical species frequencies c_1^* and c_2^* (where $c_1^* + c_2^* = 1$). However, spatially structured communities exhibit complex structures [140] and mutant competition is spatially dependent, with population expansion additionally contributing to observed dynamics. Hallatschek et al. extends his work on sectors to non-neutral case [114]. Consider the case of linear fronts. As in the previous section the distance between two domain walls $X(r)$ is treated as a continuous variable which is fluctuating due to the random motion

of the domain walls and the time is measured by $\Delta r = r - r_0$. However, now $\langle \Delta X \rangle = 2m_\perp \Delta r$ and $\langle \Delta X^2 \rangle = 4D_x \Delta r$ where the $m_\perp$ has the units of slope (see Fig. 3.5) and it is the parameter describing the net increase or decrease in sector size as a result of natural selection. In the case of beneficial mutations cells reproduce faster than the wild (i.e non-mutant) type of cells and $m_\perp > 0$. On the other hand, deleterious mutants reproduce slower than the wild type and so $m_\perp < 0$. With reference to Fig. 3.5 the parameter $m_\perp$ can be defined as

$$m_\perp = \frac{v_\perp}{v} = \tan(\frac{\phi}{2}) \tag{3.7}$$

where v is the front expansion velocity, $v_\perp$ is the velocity component perpendicular to the local direction of the front expansion and θ is the sector opening angle which will get bigger when the selective pressure increases. Given that ϕ can be measured in the laboratory by the direct inspection of sectors, it could be potentially used to deduce $m_\perp$ and hence, unknown fitness advantages of mutants. Moreover, similarly to the neutral case in Eq.(3.2) it is possible to write down the diffusion equation that describes $F(z, r|z_0, r_0)$, that is the probability of finding a sector of size $Z(r) = z$ when the expansion front is at r:

$$\frac{\partial F(z, r|z_0, r_0)}{\partial r} = 2D_x \frac{\partial^2 F(z, r|z_0, r_0)}{\partial z^2} - 2m_\perp \frac{\partial F(z, r|z_0, r_0)}{\partial z} \tag{3.8}$$

where the additional convective term is the result of bias due to fitness advantage. Note that when $m_\perp = 0$ the Eq.(3.2) is recovered. The diffusion approach can be solved and used to explore various phenomena associated with natural selection affecting the genetic structure of an expanding colony. For example, for beneficial mutants ($m_\perp > 0$) one can estimate the probability $u(L, r \to \infty|x_0, r_0)$ that the mutant sector spans the whole length L after long time r, given its size x_0 at r_0 (i.e. the probability of fixation in population):

$$u(L, \infty|x_0, r_0) = \frac{1 - e^{-m_\perp x_0/D_x}}{1 - e^{-m_\perp L/D_x}}. \tag{3.9}$$

The equation shows that the time for required for a mutant to reach fixation scales with L/D_x and so, is proportional to the population size. Moreover, since $u(L, r \to \infty|x_0, r_0)$ scales exponentially with x_0 the mutant sector has a much higher probability of fixation when its size is at least of the order of $D_x/m_\perp$.

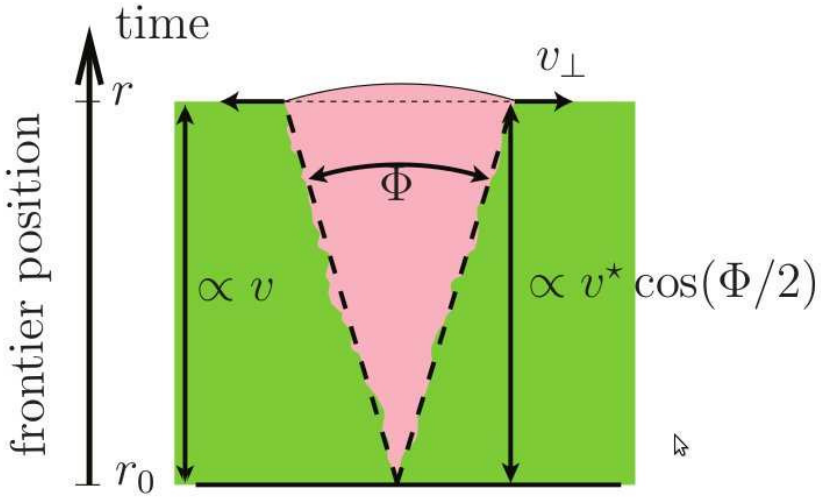

Figure 3.5 *As a small number of beneficial mutants grow in time they form a sector with the characteristic opening angle ϕ and bulge resulting from a higher reproduction rate. The opening angle ϕ is determined by $m_\perp$ which is related to the strength of natural selection acting on bacteria. Picture taken from [114]*

3.2 Conjugation

3.2.1 Conjugation in well-mixed communities

The introductory chapter of this thesis has highlighted the importance of plasmid conjugation in driving the adaptation and evolution of bacterial cells living in dense microbial communities. This section outlines more details about the present understanding of plasmid transfer dynamics.

The widely used approach to describe plasmid conjugation dynamics and infer conjugation rates in well-mixed cultures is based on mass-action models. The most important were developed by Levin et. al in [141] for conjugative plasmid, and further extended in [142] for non-conjugative plasmids. Models like these assume instantaneous plasmid transfer between cells which randomly encounter each other with the frequency proportional to cell density. There is no segregative plasmid loss due to cell division and newly born transconjugant cells can conjugate instantaneously after formation. The population dynamics of well-mixed culture where cells are allowed to conjugate is described by the set of ODEs [143]:

$$\frac{dR}{dt} = \psi(c)R - \gamma(c)R(D+T), \tag{3.10}$$

$$\frac{dD}{dt} = \psi(c)D, \tag{3.11}$$

$$\frac{dT}{dt} = \psi(c)T + \gamma(c)R(D+T), \tag{3.12}$$

$$\frac{dc}{dt} = -\psi(c)(R+T+D)e, \tag{3.13}$$

where R, D and T are the recipient, donor and transconjugant cell densities [cell/ml] respectively, c is nutrient abundance [g/ml], ψ is cell growth rate [h^{-1}], γ is the *bulk* plasmid transfer rate [ml*cell^{-1} h^{-1}] and e is the amount of nutrients [μg] needed to for a cell to replicate. Both $\gamma(c)$ and $\psi(c)$ are assumed to be first-order Monod functions [144] of nutrient concentration c of the form:

$$\gamma(c) = \gamma_{\max}\frac{c}{c+K_{\mathrm{c}}} \tag{3.14}$$

where $\gamma_{\max}$ is the maximum conjugation rate, c is nutrient concentration and K_{c} is nutrient concentration for which $\gamma/\gamma_{\max} = 0.5$. Note that in the above set of equations one distinguishes between D and T cells, because experimentally both donors and transconjugants express fluorescent proteins of different colors which depend on whether the plasmid is inherited on division or acquired by conjugation. If one marked all of them with one color (which would correspond to a single equation for all plasmid hosting cells T and D) it would be very problematic to distinguish between division and conjugation events that contribute to plasmid spread. In such case, one would not be able to accurately measure conjugation rate γ, which is of a particular interest in such assays. Indeed, given that the total population size is $N = T + R + D$ and assuming that T=0 at t=0, the above system of equations can be solved for γ :

$$\gamma = \psi \ln\left(1 + \frac{TN}{RD}\right)\frac{1}{N - N_0}. \tag{3.15}$$

Eq.(3.15) defines the end point (EP) method of the estimation of the bulk conjugation rate and is widely used to experimentally study the conjugation dynamics. The main advantage of it is that it does not depend on the initial D/R ratio. To get the estimate of γ one needs to measure the total number of cells N_0 at time t_0 and then measure T, R, D and N at a later time $t_1 > t_0$. However, the

EP method has its limitations. It assumes the same forms of $\gamma(c)$ and $\psi(c)$ for all types of cells, which might not be the case due to plasmid metabolic burden on the host cell. Moreover, the EP method is limited to mixed-cultures and this is not valid when one considers conjugation in spatially structured communities.

3.2.2 Conjugation in spatially structured populations

The observations indicate that conjugation in spatially structured populations has different characteristics when compared to this process in well-mixed cultures. The study in [145] shows that while in liquid environments the initial cell density does not affect the transconjugant yield, then in surface attached communities such dependence exists and the trend is that for higher initial densities plasmid invasion is proportionally faster. Other studies that followed [146, 147] further indicated that plasmid conjugation in surface attached populations is very different from that in liquid environments. The study of R1 plasmid conjugation [148] shows that plasmid history has two distinct phases: firstly, there is a high increase in the the number of transconjugant cells and then there is a significant drop in conjugation events. A later assay [149] on another IncP plasmid shows that when a static colony is rapidly mixed to create new contacts between cells and let to settle down, a rapid increase in the transconjugant population is observed. Rearrangement of the population cells allows mating between bacteria which could not meet before due to spatial confinement. Observations indicate that in microbial colonies conjugation occurs only between neighboring cells [150] and so plasmid is propagated at shorter spatial scales. This is in contrary to well-mixed populations where all bacterial cells can mate with each other. Later studies [141, 143] show that intrinsic plasmid transfer rates measured between two cells in surface attached communities may be orders of magnitude lower than bulk estimates, i.e. rates measured in well-mixed populations [147, 151]. A recent study by Freese et al. [152] shows that the spatial structure reduces the spread of non-neutral plasmids in the colony, mainly due to strong genetic drift, since there exists a competition between the conjugation rate μ and the selective plasmid cost s.

3.3 Aims

The discussion above shows that conjugation in bacterial colonies is a complex and not fully understood problem and to date there exists no mathematical model which would accurately and systematically predict intrinsic plasmid conjugation rates in spatially structured populations. Although methods like EP are used to study general properties of HGT, an accurate model will need to include other experimentally observed features which challenge assumptions on which well-mixed population models are based. This chapter focuses on a computational modeling of conjugation in a simple way (instantaneous process with no detailed mechanics and factors affecting its performance), with the subsequent Chapter 4 presenting a more realistic model of conjugation. Numerical simulations are the main tool in this chapter. Neutral plasmids and their effect on the population heterogeneity are considered. Moreover, plasmid segregative loss and different nutrient concentrations are inspected and evaluated for their effect on the plasmid transfer dynamics. The numerical approach taken here allows to estimate plasmid invasion probabilities and the possible relationship between population genetic structure and conjugation rates. Finally, the mathematical formalism of [113, 114, 137] and discussed above is extended to include the conjugation process.

3.4 Computational modelling of plasmid conjugation in expanding colonies

3.4.1 Modeling the colony dynamics

C++ object oriented program is used to simulate the two dimensional off-lattice growth of expanding colonies. Every cell is a growing rod-shaped soft spherocylinder of a fixed diameter $d_0 = 1\mu m$ and variable length l. Cells live in 2D space, with their position described by the position vector $\mathbf{R} = (x, y)$. Rods have spatial orientation ϕ, defined by the angle between direction vector and the x-axis. Bacterial cells do not migrate as it is assumed that the bacterial cells do not have flagella, as observed for dense microbial communities where the expression of genes responsible for flagellum is highly down-regulated [153]. Nutrients that cells consume in order to grow are assumed to diffuse in a thin layer of agarose-like substrate underneath the colony. Initial nutrient concentration is c_0 and they

diffuse with the diffusion constant D_n. Bacteria consume nutrients with rate $kf(c)$, where k is nutrient uptake rate and $f(c)$ is a sigmoid function of nutrient concentration $f(c) = c/(c+1)$. Note that for convenience the concentration at which growth decreases by 50% has been set to 1 in this formula. The dynamics of the nutrient is described by the following equation:

$$\frac{\partial c(x,y)}{\partial t} = D_n(\frac{\partial^2 c(x,y)}{\partial x^2} + \frac{\partial^2 c(x,y)}{\partial y^2}) - k\sum_i^N A_i f(c) \tag{3.16}$$

where $c(x,y)$ is local nutrient concentration at position (x,y), N is the total number of cells. A_i is the surface area of the i^{th} cell, given by $A_i = d_0 l + \pi r_0^2$ where $r_0 = 1/2 \times d_0$. As cells consume the nutrient and turn it into their biomass, their length increases. The elongation rate of the bacterial cell is:

$$v_g = g_c A_i f(c) \tag{3.17}$$

where g_c is the growth rate per unit area of cell. Larger bacteria grow faster (due to larger A_i), and the factor $f(c)$ makes bacterial cells to grow only if there are enough nutrients available. If $c(x,y) < c_{thres}$, where c_{thres} is some critical nutrient concentration, growth of the cell ceases. Otherwise, the bacterial cell grows until it reaches the maximum length l_{max} when it divides and gives rise to two daughter cell of length $l = \frac{l_{max}}{2}$. Daughter cells are almost collinear, but a small perturbation is introduced in their spatial orientation to account for experimentally observed imperfect alignment of daughter cells after division [131].

Cells growing next to each other in a dense community will push on each other due to their proliferation. The Hertzian model of elastic contact [154] is used to model cell-cell mechanical interactions. The force acting between the two cells is approximated by the force which would act between two spheres of diameter d_0 and located inside the cells. The spheres are positioned such that the distance d_{ij} between them is minimized (see Fig. 3.6). The force is then:

$$F_{ij} = E d_0^{1/2} h_{ij}^{3/2} \tag{3.18}$$

where E is the parameter that characterizes the interaction strength and is proportional to the effective Young modulus of the cell. d_0 is the diameter of

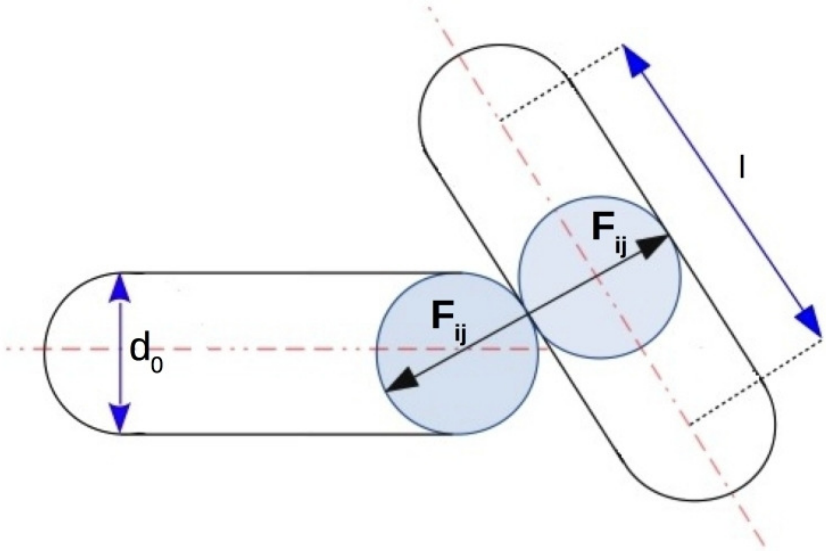

Figure 3.6 *Cells are modelled as soft rod-shaped spherocylinders of fixed diameter d_0 and variable length l. Interactions between cells are evaluated according to the Hertzian model of elastic contact between two interacting spheres.*

the cell, and h_{ij} is the overlap between cells defined as $h_{ij} = d_0 - d_{ij}$. The force acts along the vector joining the points of closest contact between rods i and j, and its direction is always such that it is repulsive on both rods. Note that by increasing the value of E it is possible to increase the stiffness of the bacterial cell, with $E \to \infty$ giving hard rods.

Consider the cell i which has n neighbor cells, with each of them proliferating and giving rise to the pushing force $\mathbf{F_{ji}}$ acting on i. The net total force acting on the cell i is $\mathbf{F_{net}} = \sum_{j=1}^{n} \mathbf{F_{ji}}$. The resulting motion of the rod i is assumed to be governed by the overdamped Newton's equation:

$$\dot{\mathbf{r}}_\mathbf{i} = \frac{\mathbf{F_{net}}}{l\xi} \tag{3.19}$$

where ξ is the coefficient of dynamic friction per unit length of the rod. Similarly, rotational motion of the cell about its center of mass is described with:

$$\dot{\phi}_i = \frac{1}{12l^3\xi}\tau_i \tag{3.20}$$

where τ_i is the net torque on i. The velocity of the center of mass $\vec{r_i}$ of rod i does not depend on the rod's spatial orientation ϕ.

To implement conjugation, one of three possible types is assigned to each cell: donor (D), recipient (R) or transconjugant (T). D-cells have plasmids and can give it to R-cells. After getting the plasmid from D-cells, R-cells become T-cells that can propagate plasmids further. Plasmid can be transferred only if the following conditions are met:

1. Plasmid goes from D- or T-cells to R-cells only.
2. Both cells need to be in an active state of proliferation.
3. Two cells need to be in the direct mechanical contact with each other for the plasmid to transfer.
4. One cell can only mate with one cell at a time.

When all these conditions are met at a given simulation update step the R-cell changes its type to T with rate $\mu \times dt$ where μ is the conjugation rate and dt is the simulation time-step. After the recipient cell becomes the transconjugant it can then propagate the plasmid further, given that all the above conditions are met again. The plasmid in simulations is neutral so it bears no fitness cost nor benefit to the host cell, and its only effect is the change of cell type. Therefore all types of cells elongate at the rate independent of their type.

Program and numerical methods

The program starts from the initial configuration of 100 cells arranged on the ring of unit radius. Half of the cells are of the recipient type and half are of the donor type. The initial nutrient concentration is c_0 at every (x, y). Bacteria grow, reproduce and interact according to the rules described in the previous section. For every system update, the following sequence of steps is performed:

1. Solve the equations of motion (3.19) and (3.20) for every cell, using the forces resulting from the previous update step.
2. Calculate new forces using Eq.(3.18).
3. Conjugate (if conditions described in the previous section are met).
4. If the cell is alive and $c(x, y) > c_{thres}$ it grows according to Eq.(3.17) and divides when $l > l_{max}$.

5. Eq.(3.16) is solved for nutrient diffusion.

Euler method of integration [155] is used to solve equations of motion in Step 1 and the simulation time increment dt needs to be small enough to reduce the integration error. The values used in simulations are $2^{-16} < dt_s < 2^{-12}$ h, with smaller values decreasing error but increasing the time required for simulations to complete. Forward finite difference method [156] is used to solve the nutrient diffusion equation in Step 5 in the above algorithm.

To compute mechanical forces between bacterial cells a similar optimization algorithm is used as in the case of the Eden model in the previous Chapter 2 of this thesis. Only cells in mechanical contact with each other can mechanically interact. The system is off-lattice and so one could pick up the cell, check the whole system of N cells to find its neighbor and then calculate interactions. However, long computations would be needed for this and there would be $N \times (N-1)/2$ iterations needed for every system update step. Thus, the 2D continuous space is divided into a grid of square 'boxes', each of the $d_0 \times d_0$ dimensions. When the bacterium moves or is born, there is a pointer to that cell added in the corresponding box based on the cell spatial coordinates. Hence, to update forces between cells, the neighbor bacteria can be picked up based on their spatial coordinates and their corresponding boxes.

For small colonies, all bacteria divide and the colony grows exponentially. As the simulated colony gets bigger, nutrient gradients form due to diffusion towards the center of the colony where nutrients are exhausted by replicating cells. Due to $c(x, y) > c_{thres}$ condition for cells to grow the colony divides into two layers. A layer of proliferating bacterial cells close at and near the expansion front forms around the colony bulk consisting of non-proliferating bacteria. Recognizing this fact allows one to increase the efficiency of the algorithm, as there is no need to compute the movement of non-proliferating cells deep in the colony.

Many simulations are needed to get a statistically significant amount of data for the conjugation process and the corresponding population heterogeneity. The range of values of conjugation rates μ that corresponds to $\sim 10^3$ simulations, each for different μ, has to be explored for a particular system configurations. Additionally, many different system configurations are needed to be explored for each value μ to get good statistics of results. Assuming 30 different system configurations and each explored for $\sim 10^3$ different values of μ, this would require at least $3 \sim 10^4$ simulations, each taking around 24 hours to reach the colony

sizes of 5×10^5 cells. Hence, in order to reduce computational time, the following algorithm is performed:

1. First, the simulation from the initial configuration up to the size of 5×10^5 cells is run but with no conjugation at this step.
2. At every $t_{snap} = 2$ minutes of the physical time the table with positions, types and growth state of all the cells in the colony is saved to memory (refer to this step as 'taking snapshots of the colony configuration').
3. After 5×10^5 cells is reached, snapshots are used to re-run the conjugation algorithm on saved configurations for different values of μ.
4. For every snapshot conjugation is performed according to the rules described in the previous section.

Thus, the computational time is saved by running mechanical simulations once only and the stored configurations allow to implement conjugation (as in this simple model it does not affect the mechanics of colony growth) given the 'snapshots' are taken frequently enough to keep the time evolution of the colony accurate.

3.5 Parameters and simulation setup

Parameters used in simulations are given and compared to experimental values in Table 3.1.

The values quoted for conjugation rates correspond to the absolute conjugation rate, i.e conjugation rate per mating pair per hour. On the other hand, measurements of conjugation rates in laboratories use techniques such as the end-point estimate, usually performed in well-mixed cultures. Such measurements give a bulk conjugation rate γ_b ml*cell^{-1}h^{-1}. However, it is possible to give the estimation of γ_b based on μ. The cell is a rod of volume approximately $1 \times 1 \times 3\mu m^3$. Since 1 ml is $10^{12}\mu m^3$, the $1ml$ of bacterial culture consists of $\approx 3 \times 10^{11}$ cell/ml (if cells are densely packed in the culture). Hence, for $\mu = 1$ it gives $\gamma_b = \mu \times (cell/ml)^{-1} \approx 3 \times 10^{-11}$. Hence, for the range of μ values given in Table 3.1 this correspondence results in $1 < \mu < 100 \rightarrow 10^{-11} < \gamma_{bulk} < 10^{-9}$. To compare, for the r702 IncP the value of γ_b is of the order of $\gamma_b = 10^{-10}$

Parameter	Simulation parameters	Experimental values
Average length before division l_{max}	$3.5\mu m$	$2-4\mu m$ [157]
Cell growth rate g_c	$5\mu m/h$	$3-6\mu m/h$ (estimate from l_{max} and cell lifetime $\frac{1}{3}-\frac{1}{2}$ h)
Cell diameter d_0	$1\mu m$	$0.7-1.4\mu m$ [157]
Coefficient of dynamic friction ξ	$200Pa \times h$	$200Pa \times h$ (estimated in [102]
Elastic modulus of cell wall E	$4 \times 10^6 Pa$	$5 \times 10^5 - 5 \times 10^6 Pa$ [158]
Nutrient diffusion rate D_n	100 μm^2/h	$2 - 4 \times 10^6$ μm^2/h [159]
Nutrient consumption rate k	50 h^{-1}	80-160 h^{-1} [160]
Nutrient concentration c_0	1 fg/μm^3	1fg/μm^3 for the minimal growth medium
Absolute conjugation rate μ	$1-100$ h^{-1}	$1-100$ h^{-1} (estimated from bulk conjugation rates) [149, 161]

Table 3.1 *The table of parameters used in simulations of microbial colonies, and the corresponding values inferred from experimental assays*

ml*cell^{-1}h^{-1} and so the range of μ picked up for simulations matches the observations [149, 161].

The initial configuration of the system and the main routine are as described before: 100 bacterial cells in a 50:50 ratio of donors to recipients are arranged in a uniform ring of unit radius r_0 that are allowed to grow and give rise to the circularly symmetric colony. Every 2 minutes the colony configuration is stored for later use in the actual simulation of conjugation and the maximum colony size is 5×10^5 cells. Snapshots are then used to explore the colony heterogeneity for different values of μ. For every snapshot a pair of neighbouring cells is picked up, checked for their types and mechanical contact, and if conditions for successful

conjugation are met then the R-cell becomes a transconjugant. Data on the number of cells of each type are saved when the colony reaches size N_t: 2×10^4, 5×10^4, 1×10^5, 2×10^5, 3.5×10^5 and 5×10^5 cells. At these measurement points the average number of sectors is evaluated according to Eq.(3.21):

$$N_S = \left(\sum_{i=1}^{n} \frac{\Delta\phi_{i,i-1}^2}{4\pi^2} \right)^{-1} \tag{3.21}$$

where ϕ is the angular size of sector i. Each sector is bound by two domain walls and to get the value of ϕ the expansion front is tracked for its boundaries. One cell from the tip of each of two domain walls is picked and the difference between the angular coordinates of these two cells gives ϕ. Sectors in Eq.(3.21) are weighted by their angular size, hence, smaller sectors contribute less and larger sectors contribute more. This method gives a better estimate of the number of sectors in the situation when a large number of very small (and negligible) sectors is present at the boundary. Fig. (3.7) shows the example of segregation patterns for two different values of μ obtained throughout simulations. Green are plasmid free cells (R), and red are cells with plasmid (D and T). For small μ (left picture) the number of recipients is similar to that of the other types (given that all D, R and T cells have similar reproduction rates). In this case, the total area spanned by both green and red sectors is similar. However, as the conjugation rate increases the number of transconjugants increases (right picture) and the plasmid becomes widespread in the population.

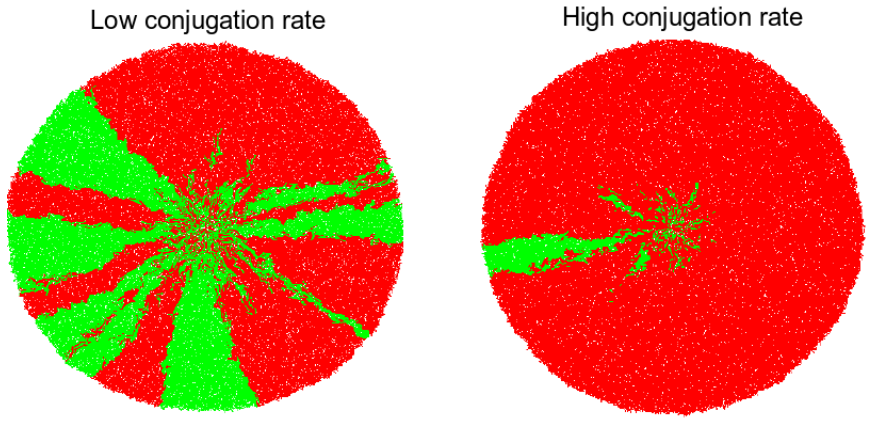

Figure 3.7 *The example of segregation patterns obtained for two different values of μ. Green colour marks plasmid free cells (R) and the red colour marks cells with plasmid (D and T).*

3.6 Numerical results

The number of sectors N_S obtained throughout simulations for a set of values of μ and different colony sizes are represented in Fig. 3.8. Every data point corresponds to the average sector number calculated according to Eq.(3.21) and is averaged over 30 independent simulations for a given value of μ. Colours correspond to the sector number count taken at different colony radii, as stated in the figure caption.

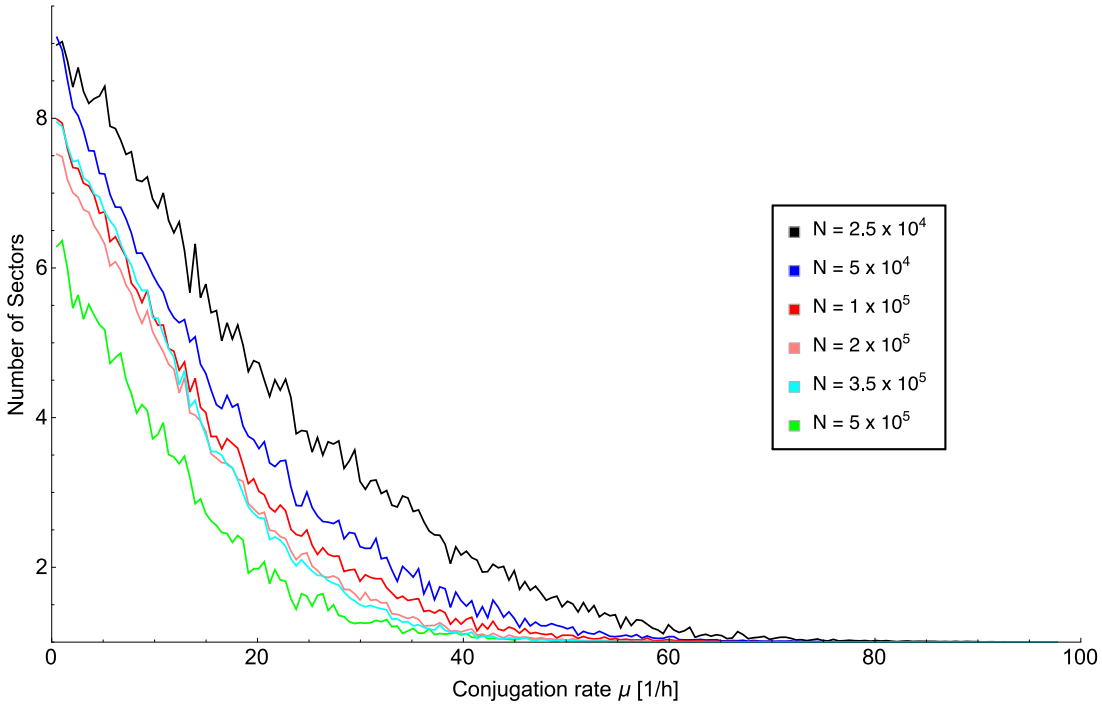

Figure 3.8 *The average number of sectors plotted against μ. As the conjugation rate increases, the number of sectors starts to decrease and ultimately goes to one. This indicates the point where expansion of the colony cannot counteract the conjugation that takes place on the sector domain walls. For large values of μ, plasmid invasion occurs and the population becomes homogeneous. Different colours correspond to sector numbers measured at different times (i.e colony sizes): $N = 2.5 \times 10^4$ (black), $N = 5 \times 10^4$ (blue), $N = 1 \times 10^5$ (red), $N = 2 \times 10^5$ (pink), $N = 3.5 \times 10^5$ (cyan) and $N = 5 \times 10^5$ (green). For longer times there are more conjugation events on sector domain walls and so, for larger colony sizes, the number of sectors is lower for a given value of μ.*

Figure 3.8 shows that as the conjugation rate increases, the number of sectors decreases. Intuitively, this can be understood by conjugation causing some sectors to expand at the expense of other sectors. In section 3.8 it is shown how this can be explained mathematically. As time passes by, more and more conjugation events take place between cells, and so one may expect that for a given conjugation

rate μ the average sector number should be lower for larger colony sizes. This is seen in Fig. 3.8 where the number of sectors decreases with an increasing colony size, as indicated by plots of different colour. A question that could be asked is whether there exists a colony size for which the number of sectors becomes fixed for a given conjugation rate μ. One might expect that given large a enough colony perimeter its expansion rate should be fast enough to counteract the conjugative bias. Unfortunately, investigating this particular issue would require simulations of very large systems, and this in turn would be limited by the computational resources available for the case of the mechanical model used above. However, another model in later section 3.7.1 explores this question further.

3.6.1 Varying nutrient concentration c_0

Fig. 3.9 shows the weighted number of sectors calculated according to Eq.(3.21) for systems growing at different nutrient concentrations c_0. Higher nutrient concentration results in higher number of sectors, however at the point where $c_0 = 4fg/\mu m^2$ that increase in the average sector count stops.

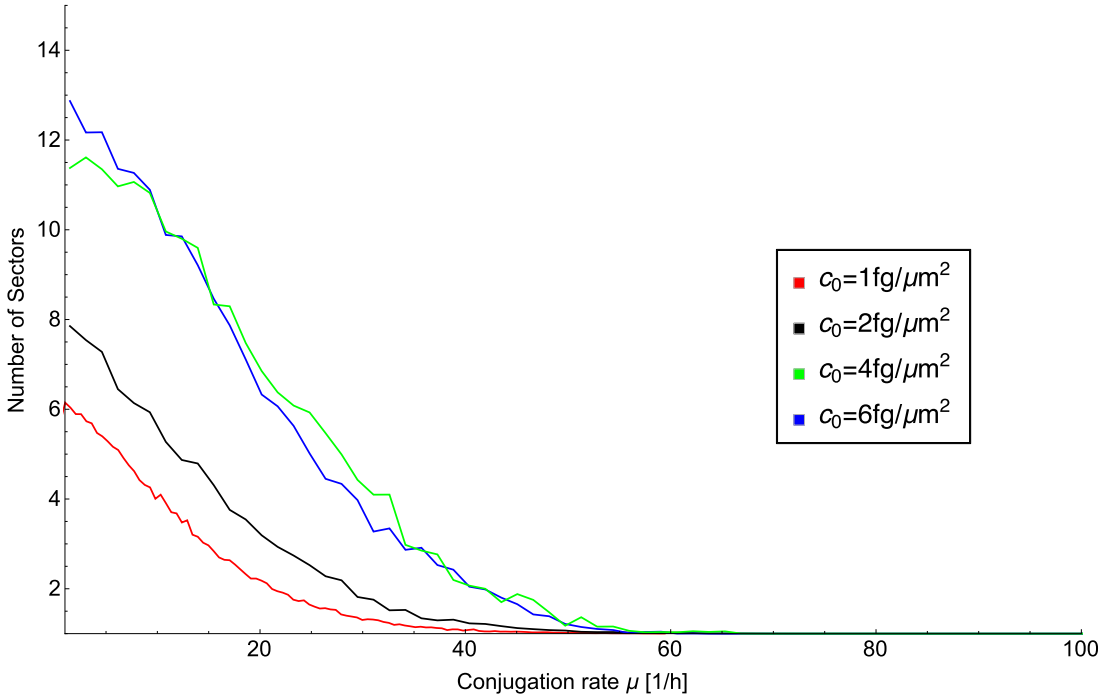

Figure 3.9 *Varying initial nutrient concentration results in different numbers of sectors. Colours correspond to different values of* c_0*: red* $c_0 = 1fg/\mu m^2$*, black* $c_0 = 2fg/\mu m^2$*, green* $c_0 = 4fg/\mu m^2$ *and blue* $c_0 = 6fg/\mu m^2$*.*

To explain these observations one should refer to the works Farell et al. [102] and

Gralka et al. [135]. In [102] it has been shown that the compactness of the colony structure and the corresponding roughness of the expansion front depend on the dimensionless branching parameter $\beta = (k\rho_0)/(\varphi c_0)$, where k is the nutrient uptake rate, ρ_0 is a local biomass density and φ is the growth rate. For decreasing values of β (that is, for increasing c_0) simulations in [102] show that the roughness of expansion front decreases. On the other hand, as β increases, the compact and circular structure of the colony as observed in Fig. 3.7 starts to develop branches which increase in amount and size as β increases. Additionally, simulations and experiments in [135] show that the larger front roughness increases the genetic drift, which in turn decreases the average number of sectors in case where there is no conjugation. Although in the case considered in this section there is an additional contribution from conjugation, the mechanism stays the same. Thus, as c_0 in simulations is increased the front roughness decreases due to decreasing β and as indicated by observations this should increase the average number of sectors. This is indeed what is seen in Fig. 3.9 where the number of sectors increases for increasing c_0. This also supports the observations in section 2.5 of Chapter 2 where a different roughness exponent α was observed for different front widths due to varying c_0. A lower value of branching parameter β which is due to higher c_0 results in a lower roughness that is characterized by smaller α, as is observed in Fig. 2.16.

Note that for $c_0 > 4fg/\mu m^2$ there is no further increase in the sector number, which can be related to the fact that β and the front roughness are so small that they do not affect the segregation pattern and the number of sectors any more. Note also that no results are shown for values $c_0 < 1fg/\mu m^2$. This is because for low c_0 the branching parameter β gets too high to give the compact structure of the colony and hence the measurement of the number of sectors is not possible in the way it is done for $c_0 \geq 1fg/\mu m^2$.

3.6.2 Segregative plasmid loss

Segregative plasmid loss is the phenomenon that occurs when the plasmid is not inherited by the daughter cell after division. For the plasmid to be inherited it needs to be segregated in enough copies between two poles of a cell before division, and failure to do so results in plasmid loss. It usually happens due to a high metabolic cost of plasmid replication that is not compensated by the fitness gain towards the host cell. Because of this phenomenon, the plasmid copy number

is reduced and given enough time, it can disappear from the population of cells. The probability of plasmid loss per division event is observed to be affected by factors such as culture dilution, temperature and pH, as well as the cell growth and division rates [162, 163].

Although the above conjugation algorithm is simple with no detailed mechanics implemented, it is nevertheless possible to implement the segregative plasmid loss without a significant decrease in the algorithm efficiency. The program is tracked for cell division events. At the every cell division event, a donor or transconjugant cell can lose the plasmid and change its type to a recipient with probability p_{seg}. The values of p_{seg} vary in values and depend on the environment, plasmid type and the family it belongs to. The review in [163] gives a example of a random distribution model which states that for a high plasmid copy number the probability that one of the cells after division ends up without a plasmid scales as 2^{1-n}, where n is the plasmid copy number. This is based on the assumption that each of n plasmids is randomly assigned to one of the cells. In the simulations in this chapter $n = 2$ gives $p_{seg} = 0.5$, however the low copy number means that the $p_{seg} = 2^{1-n}$ scaling might be not too relevant. Hence, for simulation purposes the values of p_{seg} that correspond to the experimental values obtained for a low copy number IncP plasmids are used. Based on observations and estimations in [163–165] the segregative plasmid loss rates used in simulations is $p_{seg} = 0.05$. Moreover, the additional value $p_{seg} = 0.1$ is used in the additional set of simulations to investigate the effect that varying the value of p_{seg} has on the average sector number distribution.

Bacteria are arranged in the ring of the unit radius and the colony is allowed to grow up to the size of $N = 5 \times 10^5$ cells. Sectors are counted according to 3.21 and measurements are taken at different time points. Figure 3.10 represents results obtained for simulations where the plasmid loss is implemented. Different colours in the plot correspond to the measurements taken at different time points. The figure at the top shows results for $p_{seg} = 0.05$ and the bottom figure corresponds to $p_{seg} = 0.1$. As compared to results seen in Fig. 3.8, there is no constant decrease in the sector number when the conjugation rate increases. Instead, there is a peak in the sector number count for a particular value of the conjugation rate μ^*

To explain the observed trend note that cells can now change their types in two ways. As before, the conjugation process can change the recipient cell into the transconjugant cell with rate μ, and the transconjugant cell can give rise to another transconjugant upon the division. However, now tranconjugants can

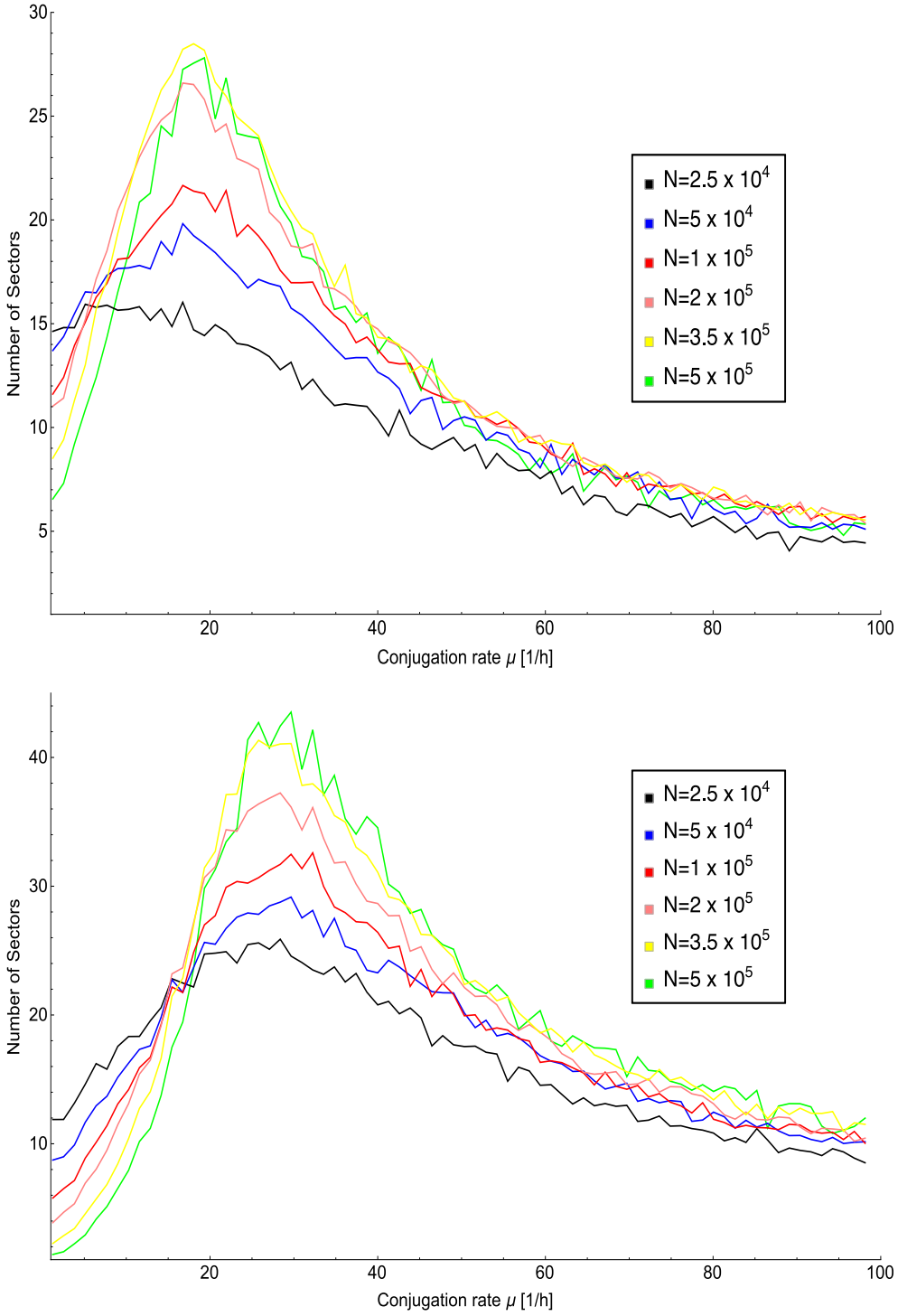

Figure 3.10 *Two plots representing sector number vs conjugation rate for two different values of* p_{seg}*:* 0.05 *(top) and* 0.1 *(bottom). Colours correspond to measurements taken at different colony sizes:* $N = 2.5 \times 10^4$ *(black),* $N = 5 \times 10^4$ *(blue),* $N = 1 \times 10^5$ *(red) ,* $N = 2 \times 10^5$ *(pink),* $N = 3.5 \times 10^5$ *(yellow) and* $N = 5 \times 10^5$ *(green). There is a single maximum that corresponds to the equilibrium between two opposing effects: plasmid segregative loss and conjugation. Note also that for* $p_{seg} = 0.1$ *the maximum moves towards higher values of conjugation rates. This results from a stronger segregative loss which causes more recipient sectors to appear that counteract the invasion of plasmid due to conjugation.*

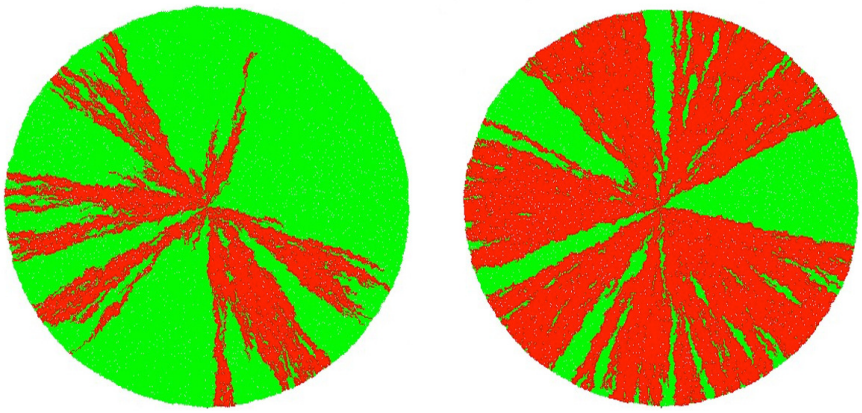

Figure 3.11 *Population structure obtained for colonies where plasmid conjugation and plasmid segregative loss influence the spatial structure of the colony. As in the case of Fig. 3.7, plasmid hosting cells (T or D) are red and plasmid recipients are green. For small conjugation rates (left, $\mu = 2\ h^{-1}$) plasmid segregation is dominant and green sectors dominate the population. As the conjugation rate increases (right, $\mu = 20\ h^{-1}$) conjugation becomes strong enough to counteract the effect of plasmid loss and red sectors become dominant. Note that as compared to colonies with no segregative loss (Fig. 3.7), there are many more patches of green sectors visible in the bulk of red sectors as a result of tranconjugants/donors reverting to recipients when the plasmid is lost.*

revert to recipients when the plasmid is lost with rate p_{seg} at the division event. Hence, there is competition between two processes: transconjugant/donor to recipient change due to plasmid loss, and recipient to transconjugant change due to conjugation. This kind of competition affects the spatial heterogeneity of the colony since new recipient sectors can emerge from the donor and transconjugant sectors due to plasmid loss. This can be seen in Fig. 3.11, where green patches of recipient sectors emerge in the bulk of red plasmid hosting cells. For $\mu < \mu^*$ segregative loss dominates and on average more recipient cells emerge during the expansion process. For decreasing μ the number of tranconjugants decreases and so they do not compensate for an increasing number of recipients. Thus, for low enough conjugation rates the recipient invasion occurs and the population is dominated by green sectors. This is manifested in Fig. 3.10 as a very low sector count for low μ. On the other hand, when $\mu > \mu^*$, conjugation dominates over segregative plasmid loss and the plasmid invasion occurs, following a similar trend to the one observed in Fig. 3.8.

It is also important to note that for the increased value of p_{seg} the value of μ^* moves towards larger values, as seen in the bottom figure in Fig. 3.10. For higher values of p_{seg} the plasmid loss is more effective in counteracting the

effect of conjugation and higher conjugation rates are needed to account for the emergence of new recipient sectors. Larger plasmid loss rates are more effective in counteracting the plasmid invasion. This also accounts for the fact that the average sector count at the plot maximum is larger for values p_{seg}. More recipient sectors emerge for higher loss rates, and this affects the average sector number in the way observed in Fig. 3.10.

3.7 Effective description and further numerical measurements

As discussed in section 3.1, the effective description of the sector pattern is related to Brownian dynamics of the sector domain walls. As the colony perimeter expands, the sector domain walls move around in a random way. The nature of this movement is dictated by the front roughness which in turn affects the average number of sectors. In case when the conjugation is considered there is also contribution coming from the plasmid transfer. It manifests itself as an additional bias in the wandering of domain walls that is proportional to μ, see Fig. 3.12 for reference.

To numerically verify whether this simplified picture of randomly wandering sector domain walls is enough to account for trends seen in Fig. 3.8 a new, simple computational model of annihilating random walkers is considered. A certain number n of sector domain walls are randomly distributed on a circle of radius $r_0 = 1$. Every random walker is described by its angular coordinate (see Fig. 3.13), with the coordinate $\phi(r)$ following Eq.(3.22)

$$\frac{d\phi}{dr} = \pm\frac{\nu}{r} + \frac{\eta(r)D_w}{r} \tag{3.22}$$

where the first term on r.h.s describe the contribution coming from conjugation at the expansion front which is described by the deterministic convection strength ν. The second term on r.h.s gives the non-deterministic contribution from the diffusive behavior of the walker, where D_w is the sector wall diffusion constant and η is the Gaussian noise with $\langle\eta(r)\eta(r')\rangle = \delta(r - r')$ for all r. Ideally two walls should annihilate when they meet at the same $\phi(r)$, however due to the numerical precision in the simulations this could not be possible. Hence, two

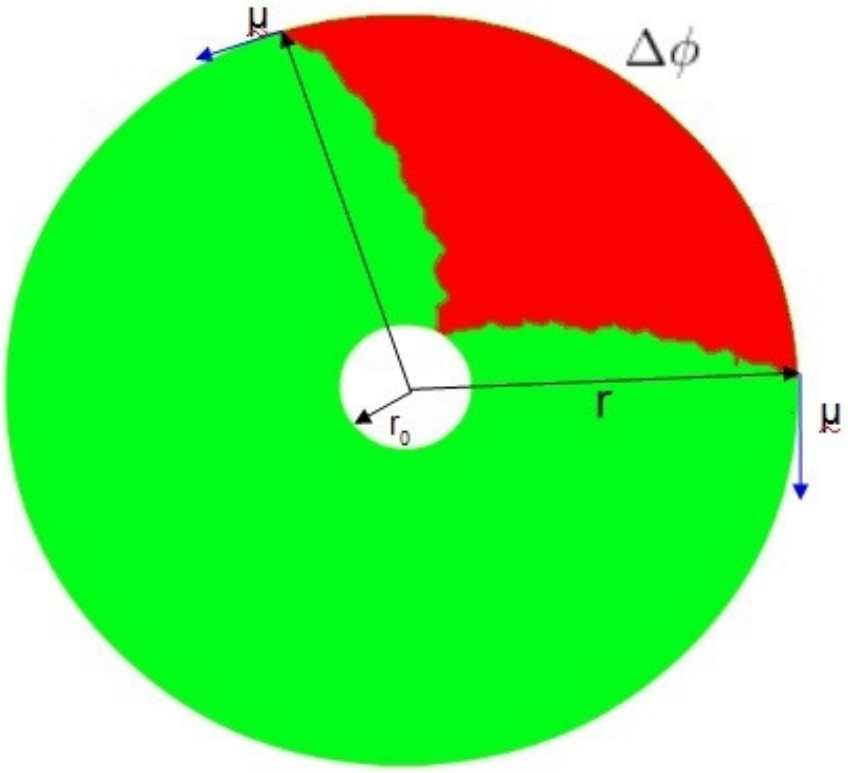

Figure 3.12 *A sector of the angular size ϕ is defined by domain walls which perform random motion with the drift of the magnitude proportional to ν.*

walls i and j are evaluated for the difference between their angular coordinates $\Delta\phi(r) = \phi(r)_i - \phi(r)_j$ and the annihilation takes place when $\Delta\phi(r)$ changes its signature.

In order to make numerical estimates that can be compared to the results seen in Fig. 3.8, the system is initialized with $n = 100$ random walkers. Every other random walker is biased in a clockwise direction, and every remaining a anti-clockwise direction (positive/negative sign in Eq.(3.22)). This is done to imitate conjugation which widens sectors with plasmid-bearing cells and shrinks the ones without plasmids. The radius is allowed to grow until $r = 60 \times r_0$ which corresponds to the colony growth from $N \approx 100$ to $N \approx 3.5 \times 10^5$ cells for the simulations that gave results in Fig. 3.8. The weighted number of sectors is calculated according to Eq.(3.21).

Fig. 3.14 represents numerical results obtained for 30 independent simulations for different values of ν (red), imposed on the corresponding plot (blue) obtained in previous simulations seen in Fig. 3.8. Note that the value of ν has been rescaled to a make the qualitative comparison of results in the plot. The ν_{scaled} parameter has been plotted such that $\nu_{scaled} = 400\nu$ so that two plots match. The

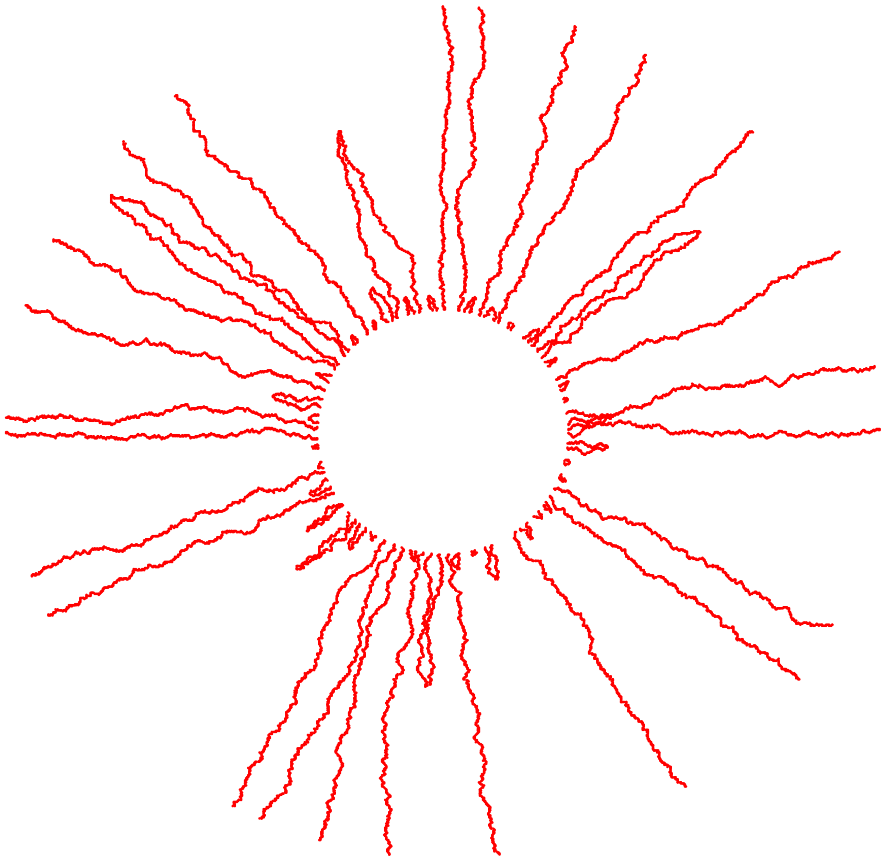

Figure 3.13 *A scheme representing the program setup used to verify the trends in sector distribution. Every random walker is defined by the angular coordinate ϕ that it makes with x-axis and is allowed to perform a biased random walk along the perimeter as the circle expands. The sector size is defined by the difference between coordinates ϕ of two neighboring sectors.*

qualitative observations indicate the same trend in scaling of the sector number with the convection/conjugation rate. For low convection strengths the number of sectors stabilises at a relatively high value already for small values of r. For larger ν there is a decrease in sector count and only one sector remains for large enough values of ν. Hence, this simplified model captures the characteristic behavior of the more complex, individual-based simulation from Section 3.6. The results in both Fig. 3.8 and Fig. 3.14 show that there exists a range of conjugation rates where the plasmid invasion will occur.

3.7.1 Larger perimeters

Exploration of the $r \to \infty$ should show whether the average sector number fixes at some particular number for large times limits. Such observation would mean

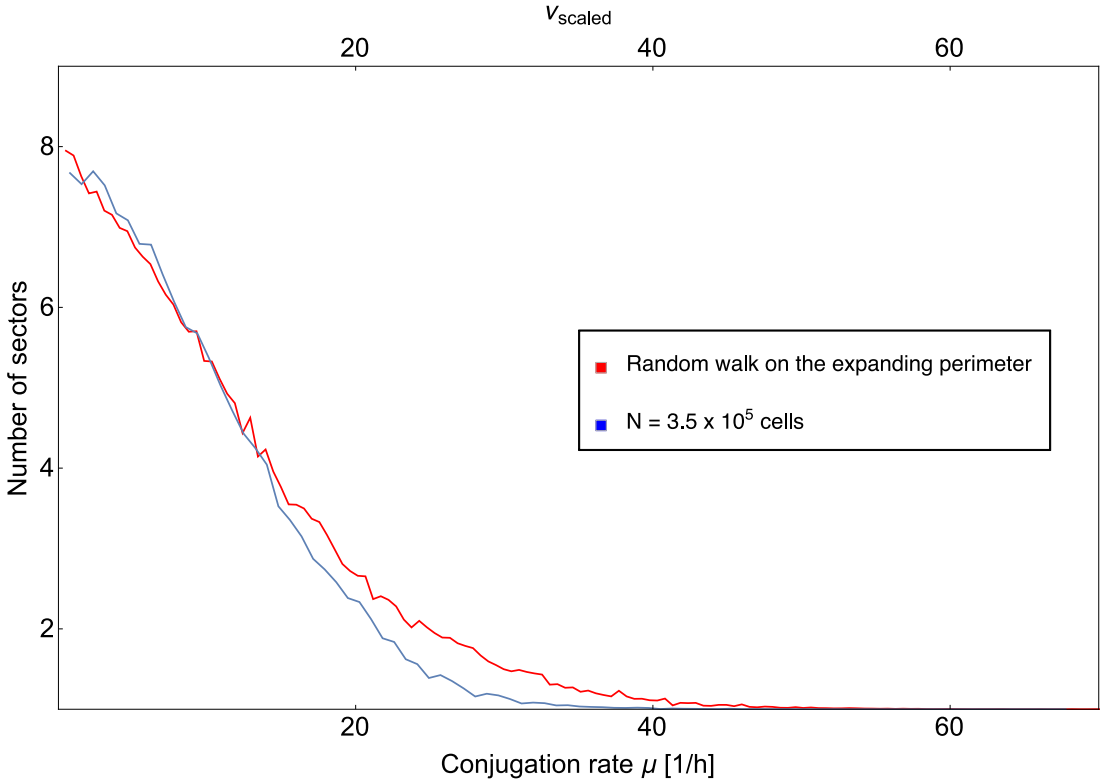

Figure 3.14 *The red line shows results obtained from simulations of a random walk on the expanding perimeter, with the top horizontal axis showing the convection strength. The blue line is the plot that corresponds to* $N = 3 \times 10^5$ *in Fig. 3.8, with the bottom horizontal axis giving the conjugation rate. Note that* ν *has been rescaled to impose plots, with* $\nu_{scaled} = 400\nu$ *in the top horizontal axis. In both cases a similar scaling of the sector number with the bias parameter is observed. Number of sectors goes quickly down to* 1 *for sufficiently large values of convection, indicating the low system heterogeneity in this regime of the bias parameter.*

that the perimeter expansion can counteract the drift of domain walls associated with conjugation. Although simulations of biased random walk for infinitely large colonies are obviously impossible, the algorithm of random walk described in the previous section can be used to explore large enough radii to extrapolate towards large values of r. Fig. 3.15 shows the results obtained from simulations run for the final radius values in the range from $r = r_0 \times 10^3$ to $r = r_0 \times 10^6$, where $r_0 = 1$ as before. The average number of surviving random walkers N_{walk}, and hence the number of sectors measured for a particular value of ν decreases at measurements taken for increasing r. Recall that quite similar observations were made in Fig. 3.8. The trend is further visible in Fig. 3.16, where N_{walk} is plotted against the colony radius r. Colours correspond to different values of ν (see figure caption) and it is clearly visible that N_{walk} is a decreasing function of r and as ν

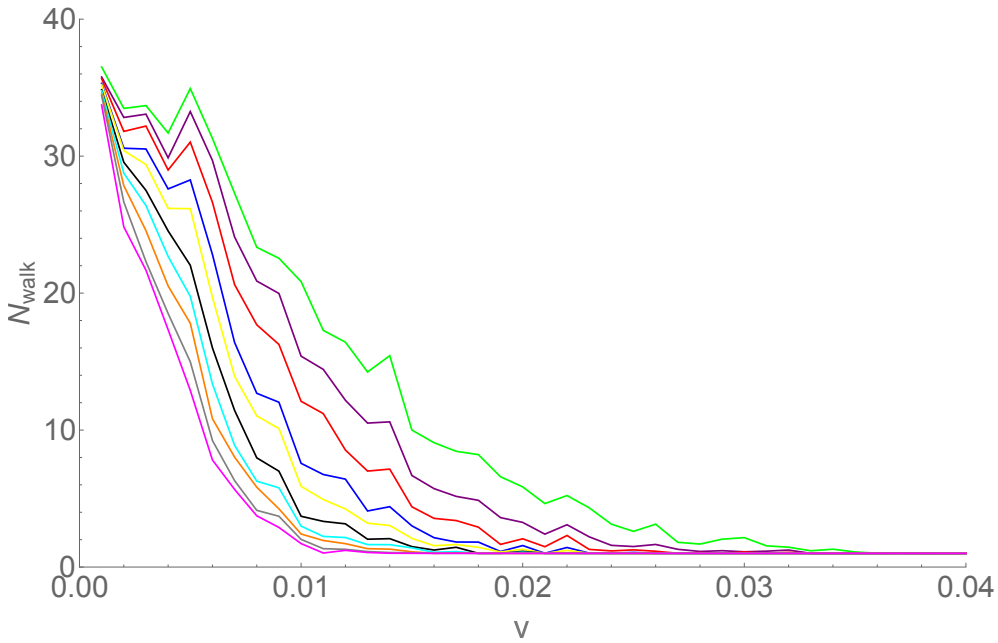

Figure 3.15 *The number of surviving random walkers N_{walk} vs ν for different values of r ranging from $r = r_0 \times 10^3$ (green) to $r = r_0 \times 10^6$ (pink). For given ν the value of N_{walk}, and hence, the average sector number decreases with an increasing r. Even for very large r (pink) the number of sectors is a decreasing function of time. Thus, the expectation is that for any non-zero convection strength the number of sectors will go to one given long enough expansion times.*

increases the $N_{walk} = 1$ for smaller r. Yet, even though the number of sectors is clearly decreasing for increasing r for all values of ν considered, it is difficult to say from the simulation alone whether it would eventually decrease to zero when the radius $r \to \infty$. However, the next section shows that a simplified model with just two sectors is able to shed light on this issue.

3.8 Mathematical model

To treat this problem more formally the analytical approach used by Hallatschek et.al [114] is adapted and extended. As already discussed in Section 3.1, Hallatschek used the dynamics of coalescing random walkers [166] to predict the number of sectors. In the case considered in this thesis the conjugation process affects the average number of sectors, as already seen from numerical results presented in Fig. 3.8. In order to investigate the phenomena that arise, it is necessary to include conjugation into the coalescing random walk methods.

The random wandering of sector domain walls on the circular expanding front

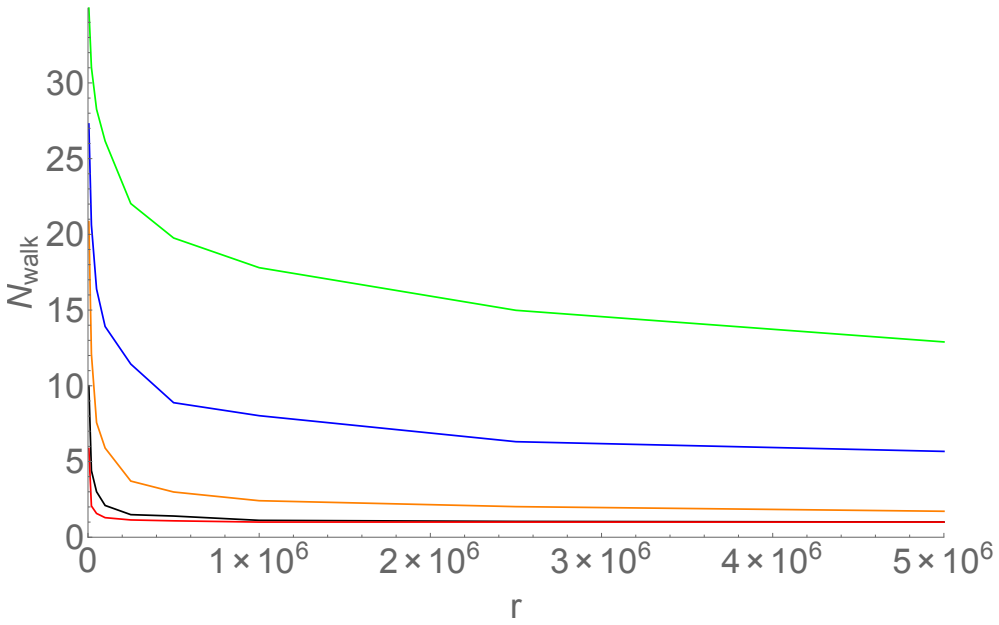

Figure 3.16 *The number of surviving random walkers N_{walk} vs r for different values of ν: 0.005 (green), 0.007 (blue), 0.01 (orange), 0.02 (black) and 0.03 (red). For all values of ν considered N_{walk} is a decreasing function of r. As the value of ν decreases, it takes longer for N_{walk} to decrease to 1.*

is determined by two contributions: diffusion which strength is measured with D_ϕ, and convection due to plasmid transfer which is proportional to ν_ϕ. It has been already shown in Section 3.1 that for the circular inoculation it is possible to express the diffusive coefficient D_ϕ in angular coordinates in terms of the diffusion constant D_x in Cartesian coordinates scaled by the inverse square of the radius: $D_\phi = D_x/r^2$.

Consider now a biased random walk of domain walls on an expanding colony front where the linear domain size (that is, the arc length between tips of domain walls that bound the sector) is w and the drift term is of magnitude ν. Let $\bar{P}(w,r)$ to be a probability of finding the sector of linear size w when the colony radius is r. $\bar{P}(w,r)$ evolves according to the following diffusion equation:

$$\frac{\partial \bar{P}(w,r)}{\partial r} = D_x \frac{\partial^2 \bar{P}(w,r)}{\partial w^2} - \frac{\partial}{\partial w}\left[(\frac{w}{r} + \nu)\bar{P}(w,r)\right] \tag{3.23}$$

where the first term accounts for spatial diffusion with the diffusion coefficient D_x. The second convective term consists of two components. The w/r term accounts for the linear expansion of front. As it expands the associated velocity field causes a point at a certain location x to move along the front. The second term is the drift term due to conjugation that is proportional to ν. Define the

angular sector size as $\phi = w/r$ and let $\bar{P}(w,r) \equiv P(\phi,r)/r$, that is the probability of finding the sector of angular size ϕ when the colony radius is r. The $1/r$ scaling comes from the normalization of probability distribution. Substituting $\phi = w/r$ and $\bar{P}(w,r) \equiv P(\phi,r)/r$ into Eq.(3.23) allows to restate the diffusion equation in terms of ϕ (see Appendix 1 for more detailed derivation):

$$\frac{\partial P(\phi,r)}{\partial r} = \frac{D_x}{r^2}\frac{\partial^2 P(\phi,r)}{\partial \phi^2} - \frac{\nu}{r}\frac{\partial P(\phi,r)}{\partial \phi} \tag{3.24}$$

where the linear domain $\phi \in [0 : 2\pi]$. To investigate the behavior of Eq.(3.24), consider a system that consist of two sectors of the same initial size. In such case, the initial angular size of the plasmid-bearing sector is $\phi_0 = \pi$ which corresponds to the initial condition for Eq.3.24 such that $P(\phi, r_0) = \delta(\phi - \phi_0)$, where r_0 is the initial colony radius. The domain wall at $\phi = 0$ or $\phi = 2\pi$ means that the sectors spans all the system and hence, plasmid fixes in the population. To account for this, the absorbing boundary conditions are imposed, such that $P(0,r) = P(2\pi,r) = 0$ for every $r > r_0$.

The equation is difficult to solve analytically for the finite domain $\phi \in [0, 2\pi]$. The main problem arises due to the radius dependencies on the right hand side of the equation which do not allow one to apply the conventional tools usually used to solve diffusion equations. Separation of variables does not work because two sides of the equation are conjugated by r. Similarly, Fourier series analysis is not possible as it is impossible to write down the Fourier modes that are independent of r. It is however possible to solve the equation for the infinite domain. In such a case, the absorbing boundary conditions at infinity are $P(-\infty, r) = P(\infty, r) = 0$ and the initial condition $P(\phi, r_0) = \delta(\phi - \phi_0)$. The solution of Eq.(3.24) (see Appendix 2 for more details of derivation) for the infinite domain is:

$$P(\phi,r) = \left(4\pi\left(\frac{1}{r_0} - \frac{1}{r}\right)\right)^{-1/2} \exp\left(\frac{-(\nu\ln(r) - \nu\ln(r_0) - \phi - \phi_0)^2}{4D_x\left(\frac{1}{r_0} - \frac{1}{r}\right)}\right). \tag{3.25}$$

The example density plots that come out of Eq.(3.25) are shown in Fig. 3.17 where $\phi_0 = \pi$, $r_0 = 1$ and $D_x = 0.1$. The value of $\nu = 0.1$ for left hand side and $\nu = 0.5$ for right hand side picture. The yellow strip represents $P(\phi, r)$. In both cases the bias causes the shift of probability distribution in ϕ towards more positive values

of ϕ. Larger values of ν increase the shift of probability distribution. Note that $1/r$ scaling of ν in the original diffusion equation manifests itself as the decrease in the drift velocity as r increases.

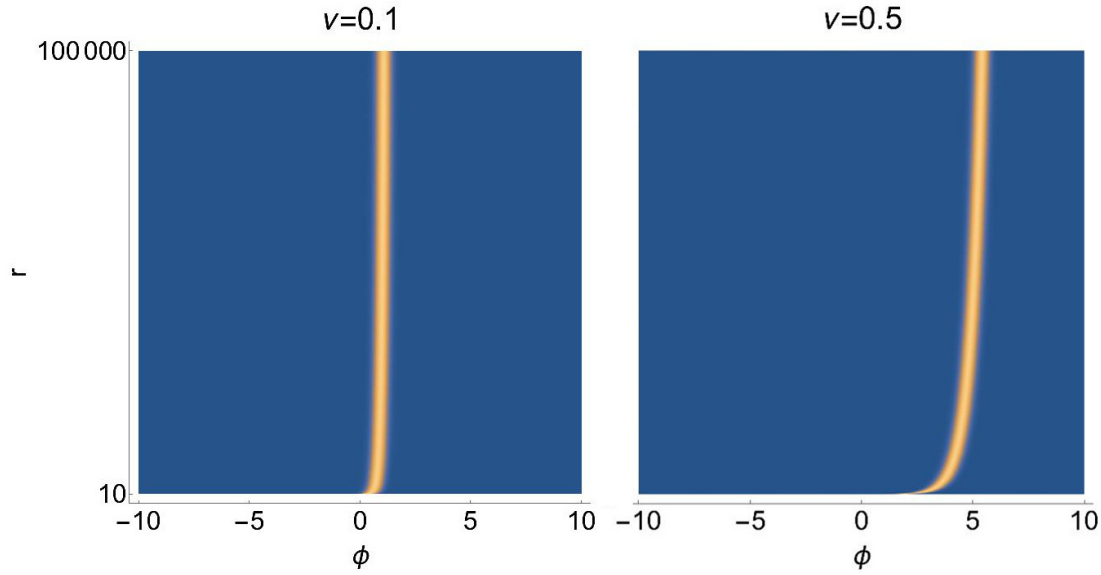

Figure 3.17 *The plot shows the probability distribution (yellow strip) that comes from the solution of Eq.(3.25) for two different values of ν plotted against r, for two sectors of the same initial size. In both cases the drift due to conjugation is determined by ν and causes the shift of probability distribution towards larger values of ϕ as r increases. As expected, for larger values of ν the shift is more significant. Note that as r increases the colony perimeter expansion reduces the rate of increase in ϕ.*

One could possibly argue that Eq.(3.25) might be used to predict the segregation pattern of the system consisting of two sectors for colonies with an infinite perimeter. However, this is not a physical case because such colonies do not exist. Asking about the probability of plasmid invasion on the infinite population does not make sense as it would need to span an infinite expansion front. It is necessary to retrieve original boundary conditions $P(0,r) = P(2\pi,r) = 0$ to account for the finite colony sizes. In the case of one absorbing boundary, it could be possible to apply the method of images to Eq.(3.25) and retrieve the absorbing boundary at $\phi = 0$ or $\phi = 2\pi$. Two absorbing boundaries are more difficult as it is necessary to apply two biased random walker images outside $\phi = 0$ and $\phi = 2\pi$ boundaries. Because of this, there appears to be a coupling between all three biased random walkers which does not allow one to analytically retrieve $P(0,r) = P(2\pi,r) = 0$ boundaries with the method of images. However, the form of Eq.3.25 gives the clue on what can be expected for large values of r. It suggests that the mean angular size $\langle\phi\rangle \propto \nu \log(r)$ and so given enough time a plasmid-bearing sector

can span any size on an infinite domain. Thus, restricting the domain to size to $\phi \in [0; 2\pi]$ would mean that for long enough times the plasmid-bearing sector will span the whole expansion front and thus the plasmid will overtake the population. The next section shows this effect by numerical evaluation of Eq.(3.24) on a finite domain.

3.8.1 Numerical solutions of the diffusion equation

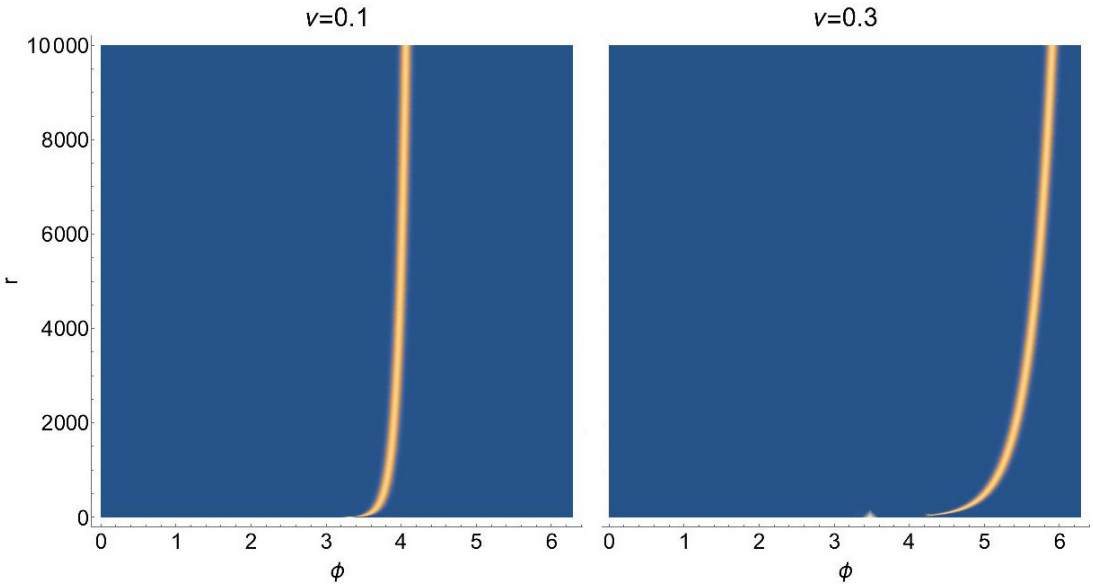

Figure 3.18 *The plot shows the probability distribution (yellow strip) that comes from the numerical solution of Eq.(3.24) on the finite $\phi \in [0; 2\pi]$ domain for two different values of ν, for two sectors of the same initial size. The trend is very similar to that in Fig. 3.17 which should be expected since the Eq.(3.25) is the solution of Eq.(3.24) for the unbound case. Here, when the probability distribution hits the $\phi = 2\pi$ boundary the random walker gets absorbed and the plasmid-bearing sector spans the whole colony.*

As discussed, solving the Eq.(3.24) analytically in the finite $\phi \in [0; 2\pi]$ domain is difficult even for two sectors of the same initial size ϕ_0. However, it is still possible to study it via numerical methods. Using the Mathematica software allows to obtain the time evolution of $P(\phi, r)$ for a range of conjugation rates ν and with absorbing boundaries $P(0, r) = P(2\pi, r) = 0$. Fig. 3.18 shows the example of density plot obtained through this numerical approach. As in the case of the infinite domain, the drift due to conjugation causes the probability distribution to move towards larger values of ϕ as r increases. In the case considered here the boundaries are absorbing and when the $\phi = 2\pi$ boundary is hit the sector spans the whole colony. To find the probability that the random wandering of a

domain wall causes it to hit one of the boundaries and to get absorbed, define the probability of absorption at the boundary when the colony radius is r' as

$$A(r') = 1 - \int_0^{2\pi} P(\phi, r')d\phi \tag{3.26}$$

where the integral gives the probability of survival at radius r', i.e probability of finding the random walker somewhere at $\phi \in [0; 2\pi]$.

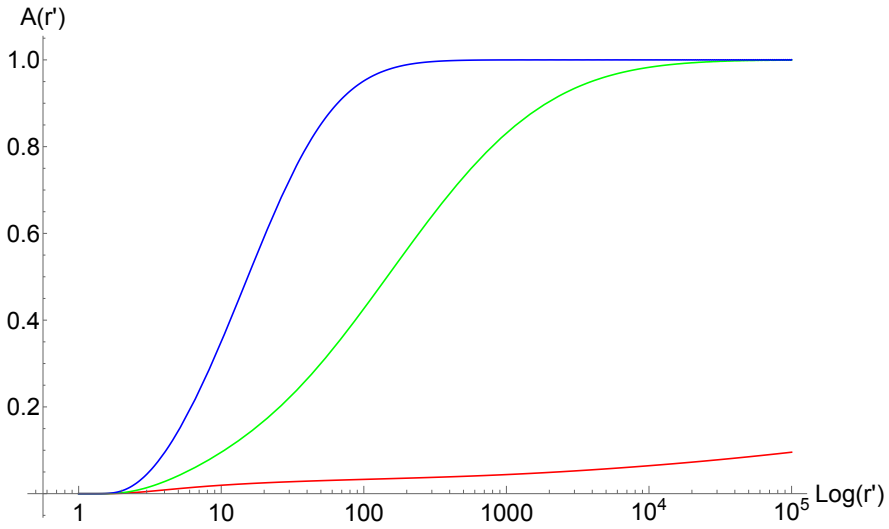

Figure 3.19 *$A(r')$ at the $\phi = 2\pi$ boundary based on the numerical solutions of Eq.(3.24) for two sectors of the initial angular size $\phi = \pi$ at $r_0 = 1$. Plots show the evolution of absorption probabilities in time. Three colours correspond to three different values of the drift parameter: $\nu = 0.01$ (red), $\nu = 0.03$ (green) and $\nu = 0.1$ (blue). For low conjugation rates (red) the absorption probability is very low and hence, even for very large values of r' two sectors can coexist at the same time. For the increasing conjugation rates the absorption takes place on smaller timescales that can be obtained in the laboratory conditions. Increasing the ν by one order of magnitude (blue) makes the absorption highly probable. Fast plasmid invasion can occur for such values of ν and the corresponding genetic trait can overtake the population.*

Fig. 3.19 shows survival probabilities $A(r')$ numerically evaluated for different values of ν and calculated for $r' \in [r_0, r_{max}]$ where $r_{max} \gg r_0$. It shows that the absorption probability for low conjugation rates (red) is very low. This is a similar case to that observed in Fig. 3.8 for low conjugation rates, where a relatively high number of sectors are observed even for large colony sizes. Note the rate of increase in absorption probability increases when the radius goes to large values of $r' > 10^4 \times r_0$. Based on this observation one might expect that the absorption probability tends to one for $r' \to \infty$. However, given that the initial

colony sizes are of the order $r_0 = 100\mu m$ one cannot expect r' to be larger than $100r_0 = 1$cm. Thus, for such realistic r' the colony will have two sectors as long as $\nu \ll 0.1$. These observations are similar to those in Fig. 3.8 and Fig. 3.14 where the decrease in the number of sectors for an increasing conjugation rate is observed.

Note that all the above numerical estimations based on Eq.(3.24) are made for the system that initially consists of two sectors only. To accurately model the sectoring pattern in the case of more than two sectors, one would need to include multiple diffusion equations to account for the dynamics of every individual domain wall. Moreover, the dynamics of random walkers would be coupled due to annihilation events at the expansion front. Formulation of such a problem is not trivial, and given the challenge that even two random walkers pose in case of the analytical approach, the mathematical analysis for more sectors could prove very difficult.

3.9 Summary

This chapter explored the influence of the plasmid conjugation on the spatial heterogeneity of 2D expanding microbial populations. The investigation was based on mechanistic simulations of microbial populations and implementation of the simple conjugation algorithm. Results show that neutral plasmids are capable of invading populations, given large enough expansion times or large enough conjugation rates, as seen in Fig 3.8 and 3.15. Throughout further simulations (Fig. 3.14) it has been shown that the observed pattern can be effectively described by the annihilating random walk of sector domain walls. Further mathematical exploration and the solutions of the corresponding diffusion equation (3.24) that drives the spatial heterogeneity of the system consisting of two sectors and neutral plasmid were performed. Numerical solutions of Eq. (3.24) for domain wall annihilation probabilities confirm observations from Fig 3.8 and 3.15 and show that strong conjugation can result in the plasmid dominated population. However, it was also shown that only large enough conjugation rates enable the plasmid to spread to the whole growing layer for realistic colony sizes, as seen in Fig. 3.19.

Additional factors that can affect spatial structure due to plasmid transfer were explored. Simulation for varying nutrient concentration c_0 show that there exist

a range of c_0 values (Fig. 3.9) for which conjugation performance is affected, with higher nutrient concentration giving larger number of sectors. Results also indicate that the roughness of the expansion front (which is decreasing for increasing c_0) affects the measured values of sector numbers. Another set of simulations shows that segregative plasmid loss causes the competition between plasmid loss and conjugative plasmid acquisition. Observations in Fig. 3.10 indicate that two low-sector number regimes arise, with a single maximum in the sector count that corresponds to the state where plasmid loss and conjugation contribute equally towards the distribution of sectors, giving rise to many sectors.

Simulations and numerical modeling show that the conjugation rate is the crucial factor that impacts the structure of expanding populations. Fast enough conjugation can homogenize the population i.e. all bacteria will have the plasmid. Such a scenario might be highly unwanted if a plasmid codes, for example, for an antibiotic resistance trait and is present in the clinical environment. Conjugation rate can be affected by many factors, including environmental ones (tempereture, humidity, pH etc. [167–170]) and according to Fig. 3.8 even small changes in μ can significantly change the fate of the plasmid (fixation vs. extinction). Results shows that plasmid segregative loss can effectively reduce the extent of plasmid invasion, however there still exists the regime of conjugation rates where plasmid-loss is counteracted by the plasmid invasion due to conjugation.

Observations made in this chapter indicate that simulations could be used together with experimental assays to infer plasmid invasion rates from the sector number distribution. This can supplement present approaches used for experimental measurements of conjugation rates in spatially structured populations, which mainly involve precise counting of different types of cells and finding ratios of transconjugants to donors and recipients [171, 172]. This kind of approach is usually time consuming and prone to errors, as it requires precise counting of individual cells. In contrast, experimental sector counting would not require time-consuming assays on cell numbers and can be performed using low-magnification imaging, since individual cells do not have to be distinguished. Such procedure would require labeling cells with fluorescent proteins that would distinguish between plasmid hosts and cells which do not have plasmids. Given that the generation time for *E.coli* is 20 minutes in good laboratory conditions, this would ideally require around 400 minutes (that correspond to around 20 generations in the exponential phase of growth) to reach the colony sizes of 5×10^5 cells. These time scales would be short enough to perform multiple sector count

assays and get statistically significant results. On the other side, a potential problem could be confining the growth to two dimensions, as it is observed that for colony sizes investigated in this chapter ($\approx 5 \times 10^5$ cells) the growth transits into the third dimension [29].

To get a more accurate computational model of conjugation more factors that affect and define conjugation process should be included in the simulation framework. These could include the transconjugant lag phase, the nutrient effects, in addition to already considered segregative plasmid loss. Moreover, conjugative junctions [173] are an important biomechanical factor that affects the conjugation process and mechanical interactions between cells by stabilizing mating cells. Next chapter of this thesis aims to take a more accurate view on conjugation, and aims to develop a more accurate algorithm for conjugation.

Chapter 4

Towards a more realistic conjugation model

4.1 Plasmid transfer mechanism

The model of conjugation presented in the previous chapter allowed one to efficiently explore the sectoring patterns and quantify the dynamics of plasmid transfer. It has been shown that a simple, non-mechanical model of biased random walk on an expanding perimeter captures the general statistical phenomena that emerge from more complicated, mechanical simulations. However, the assumption that conjugation is an instantaneous process is an oversimplification. On the level of a single cell the conjugation process is something more than a simple change of bacterial type. It is a complex and not yet fully understood process that involves many different steps that lead to plasmid transfer. For example, there is an apparent lack of study on the nature of conjugative junctions and their effect on stabilization of the mating pair against the external forces. Motivated by experiments on colliding colonies, the study in this chapter extends the computational model developed in Chapter 3. It contributes a novel computational framework where conjugation is not instantaneous and where conjugative junctions are physical objects that have a form of bridges between cells and provide an important biomechanical contribution to cell-cell interactions. Simulations in this chapter highlight some of the physical aspects of conjugative junctions that might be crucial in determining the success of plasmid transfer. The study in this chapter is a step towards understanding the key mechanical

aspect of plasmid conjugation.

4.1.1 Pilli and conjugative junctions

The exact mechanism of the plasmid transfer varies between plasmid incompatibility groups and involves many genetic factors that contribute to the successful conjugation event. In general, the conjugation process can be split into two steps: mating pair formation and DNA transfer due to relaxosome action. Fig. 4.1 shows an example scheme of the plasmid conjugation process between two cells. The first step of mating formation involves the mobilization and synthesis of secretion system proteins that are used to bring cells closer to each other and allow the plasmid to move between cells. Gram-negative bacteria such as *E.coli* use a Type IV secretion system (T4SS) [174, 175] to secrete and transfer biomolecules such as proteins and plasmids. Due to its resource cost, T4SS is normally switched off, and it is expressed (switched on) only when encountering the necessary stimulus, such as a plasmid-free cell or sex pheromones [176], is present in the surrounding environment. There are two components that are the main elements of T4SS: pilus and multiple secretion channels. The later is observed to be used for transferring the mobilizable elements between cells [177, 178]. However, this can happen only when two mating cells are close enough to each other. The experiments show that the pilus is used to bring two cells into such contact [179]. Yet, the exact role of pilus has been elusive and the question arose on whether facilitation of the mechanical contact is the only role of the pilus.

The F-plasmids that belong to the IncF incompatibility group were the first group of conjugative plasmids that has been systematically studied for the conjugation mechanics and the associated pilus action. F-plasmids are associated with conjugation in both liquid and solid environments. The IncF pair formation mechanism involves a long, thick and flexible pilus that has been observed to bring two cells together [181] and facilitate the mechanical contact between the mating pair. The pilus is made of a single, repeated sequence of pilin protein subunits [182, 183] coded by at least 12 different genes and has the form of a long (up to $2\mu m$ long), narrow cylinder [184] of approximately $8nm$ diameter and $2nm$ inner axial hole running through the whole length of the pilus. This kind of structure was sure to provoke questions on whether the pilus itself serves as a bridge for plasmid DNA transfer [185–187]. There has been a lot of controversy

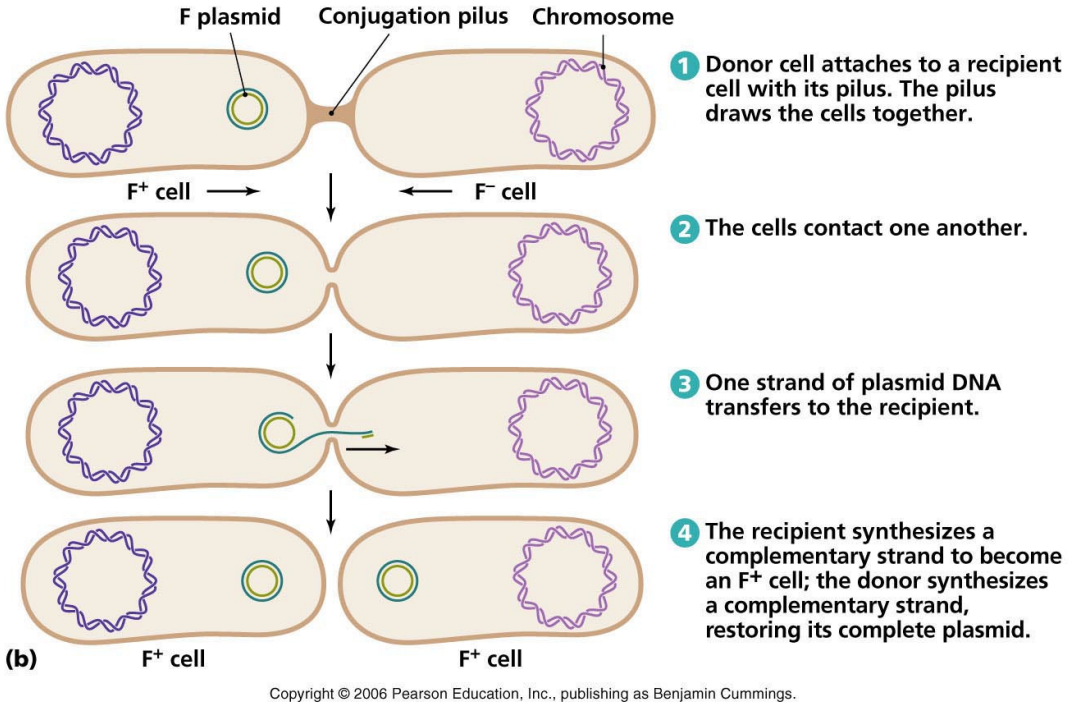

Figure 4.1 *Plasmid conjugation can be divided into two steps. Firstly, the mechanical contact between donor and recipient cells is established by the action of conjugative pilus that brings two cells together. Although the main role of the pilus is to bring two cells into direct contact by the process of pilus retraction, its exact role is still not certain. After mechanical contact between cells is made, transfer genes take part in the action of DNA splitting, transfer and termination of the conjugation procedure. At the end of conjugation, the synthesis of a plasmid complementary strand causes the recipient to become the transconjugant that can donate plasmid to other recipients. (Image source: [180])*

through the years of study on that topic. Early research, such as in [185] indicated that cells do not require close contact to successfully transfer DNA, which was further supported by research in [188] which indicated long-distance conjugation. However, spatio-temporary resolutions used in these experiment were small, and it could be possible that cells had enough time between measurements to move into close enough contact to perform conjugation. Thus, research continued and another studies by electron microscopy imaging have shown that pilus retraction [181, 189] is indeed used to bring cells into the direct mechanical contact and the observations indicated that the direct contact between cells results in much higher amount of transconjugant cells. Yet, the uncertainty on the exact role of the F-pilus still remained, and studies on other incompatibility groups did not bring clarification.

The IncP incompatibility group is a family of plasmids that is seen to perform well

in spatially structured populations, as opposed to liquid environments preferred by IncF [60]. It became a very important plasmid group for studies since biofilms and other forms of surface attached bacterial populations are abundant in clinical environments and can confer for antibiotic resistance, as already discussed in the introductory chapter of this thesis. The IncP family is characterized by short, rigid pili that are often present in multiple copies when the secretion system is expressed. As in the case of IncF however, the main role of the pilus is to bring cells into the mechanical contact, and as in the case of IncF, the exact role of the pilus in plasmid transfer is still uncertain [190]. The microscopy study of mating pairs in surface attached communities is hard, as it usually requires preparation of the sample in the liquid immersion that might have an effect on the details of cell-cell interactions. The study in [173] used the cryofixation method to 'freeze' the mating population. The resultant microscope picture of the frozen mating pairs is shown in Fig. 4.2, and it indicates the existence of high-electron density contact points between cell membranes termed as 'conjugative junctions' or 'mating bridges'. The existence of these kind of junctions had been already confirmed in [191] for the IncF plasmid family, yet both studies show no membrane-breaks that could be associated with channels used for the plasmid transfer. However, junctions observed in [173] are dominant only between donor-recipient cells and the distances between centers of cell bilayers are observed to be smaller than in case of cells with no plasmids. The study indicates that pillin is not essential for the formation of conjugative junctions, although it might serve the additional mating-pair stabilization function as junctions are more interrupted in the absence of pillin. Thus, the role of pillin and pili in the case of IncP plasmid conjugation might be of lower importance as compared to the IncF case discussed in the previous paragraph[191]. Yet, the role of pillin in the mating pair stabilization in case of IncP plasmids cannot be ignored. Studies such as in [192, 193] show that mating-aggregates consisting of up to 20 cells tend to form in a well-mixed environment, and due to stabilization by pilli conjugating cells are more resistant to shear forces that would otherwise break up mating pairs. Although the number of potential partners to conjugate with is much more restricted in dense spatially-structured colonies, the effect of pillin on mating pair stabilization is still important in such dense communities where forces acting between cells can significantly affect the colony morphology [29]

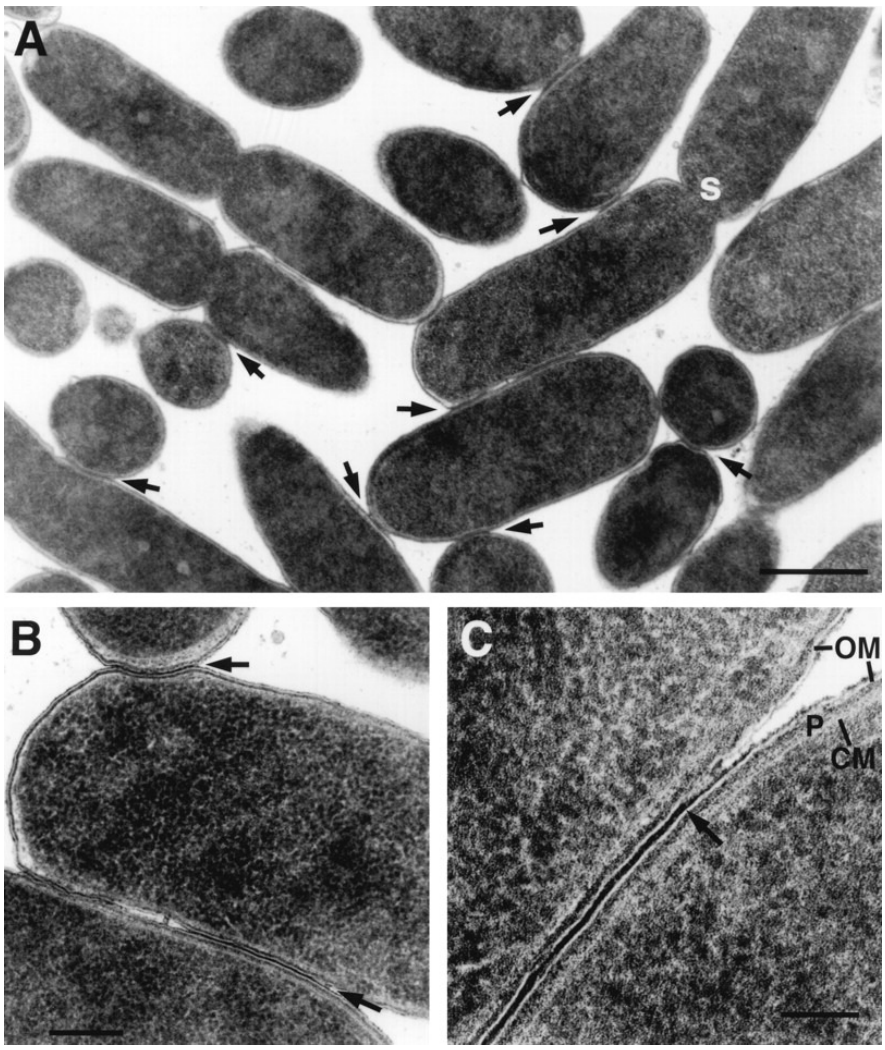

Figure 4.2 *The microscopy images of cryofixed conjugation mating pairs. Arrows indicate the high-electron density points of contact between cell-walls that form between mating pairs and act as conjugative junctions. (Image source: [173])*

4.1.2 Plasmid transfed dynamics and factors affecting the performance

Transfer of plasmid DNA is usually started and performed after the mechanical contact betweeen cells is established. Every conjugative plasmid carries the genetic code that includes the origin-of-transfer (*oriT*) nucleotide sequences serving as the transfer initialization sites. At the start of the conjugation process *oriT* serves as the assembly point for the complex of proteins called relaxosome. Along with the set of transfer genes (*tra-*) and their products, relaxosome serves the action of DNA separation, its transfer to the host cell, and finally the termination of conjugation procedure [194]. Although the exact details of these

processes are not in the scope of this thesis, an important point here is that all these steps make the conjugation process susceptible to outside factors and are far from being instantaneous. Even though the previous Chapter 3 considered conjugation as instantaneous, it is necessary to extend this view in order to capture the mechanics of the conjugation process that acts over time. As in case of the general conjugation mechanism, the time to complete the conjugation process varies between plasmid families. The main difficulty from the exact measurement of plasmid transfer pace and times comes from the fact that it is hard to estimate the moment of conjugation initialization, plasmid mobilization and transfer completion. The normal procedure of estimating the conjugation yield involves counting cells that express the fluorescent proteins encoded into plasmids that are expressed only after the plasmid is transfered to a recipient cell. This allows one to calculate transconjugant to donor or transconjugant to recipient ratios and estimate bulk conjugation rates, however, it gives little to no information about the pace at which the plasmid is transferred. The study in [170] aimed to estimate the time required for the mating process to complete. By performing multiple assays with dense mixtures of the pXO16-plasmid recipient and donor cells, Andrup et.al. investigated for the appearance times of first transconjugants. The study allowed them to infer that mating takes ~ 4 minutes for a plasmid of 200kbp size, giving a transfer rate of around 1-kbp per second. However, one needs to be careful with extrapolating this result to other plasmids of the IncP family, as such a rate of transfer was obtained in very good laboratory growth conditions which are not necessarily met in natural environments. The later study on F plasmid in [195] indicates that the mating event is 7 minutes long in case of IncF, significantly higher than that observed for pX016. Another observations in [170] study indicate that there is a lag phase associated with newly formed transconjugant cells which need to wait a certain amount of time before they can propagate the plasmid further. The plasmid lag phase is related to the expression of plasmid-related phenotypes and the metabolic burden due to plasmid transfer process. The recipient cell firstly integrates and expresses plasmid after which the metabolic recovery period takes place. Only then the conjugation process can start over again. For the pXO16 plasmid the lag phase was measured to have around $5 - 15$ minutes in the laboratory conditions conditions [170]. The later studies on F-plasmid in [195, 196] indicate the existence of such a lag phase in case of IncF group, and the transconjugant recovery time was estimated to reach 90 minutes, two times the measured cell generation time. Since the conjugation process in these assays was induced by

chemoattractants, the conclusion is that plasmid transfer could be induced only when the number of recipient cells, and the corresponding density of pheromone peptides, recovered after conjugation events. However, the F-plasmid study in [195] is in contrast with the previous assay in [169] where the lag phase for F-plasmid transfer in *E.coli* populations were estimated to last for 40 minutes. This again shows that time-scales involved in plasmid transfer vary between different plasmid species and can be environment dependent. Yet, with the above studies considered, it is quite surprising that in the era of powerful microscopes and novel laboratory methods quite a limited number of direct observations on conjugation dynamics have been performed so far. The studies in [197] and [198] used fluorescent microscopy to study the partitioning and copy number of plasmids in cells. Each plasmid was tagged with a fluorescent marker and the life cell images taken had large enough resolution to distinguish between individual plasmids. By applying this type of experimental methods to plasmid conjugation, one should have a much greater insight into the dynamics of plasmid transfer between cell. Such measurements performed on a single-cell level should clarify the above observations which were based on conjugation assays performed on whole populations.

Nutrient dependency

In order to initialize, perform and complete the plasmid transfer process, both host and recipient cells need to use energy and hence, they require nutrients to account for the costly process of conjugation. The study on well-mixed environments in [143] and detailed in subsection 3.2.1 uses the first-order Monod function approximation to express the relationship between the bulk conjugation rate $\gamma(c)$ and nutrient concentration c, taking the form of Eq.(4.1)

$$\gamma(c) = \gamma_{\max} \frac{c}{c + K_{\mathrm{c}}} \tag{4.1}$$

with $\gamma_{\max}$ being the maximum conjugation rate and K_{c} being the nutrient concentration when $\gamma/\gamma_{\max} = 0.5$. However, later studies on IncP families in surface attached communities [199, 200] indicate that the first-order Monod approximation of $\gamma(c)$ function might not be the most accurate description. The observations indicate threshold dependency on the nutrient concentration which has the form of the step function. No transconjugants are observed for nutrient

concentrations below some critical c_{min}, and there is little nutrient concentration effect observed when $c > c_{min}$. Based on these studies and other which followed [146, 149] the approximation of $\gamma(c)$ to step function is reasonable. Further observations in these studies indicate that even though $c > c_{min}$ is required to initialize the conjugation process, the reduced amount of nutrients does not affect the conjugation performance if it is already initialized. This suggests that the plasmid transfer mechanism 'senses' the amount of nutrients and activates only when there are enough of them to compensate the cell for the increased metabolic cost throughout the whole conjugation process.

There are no detailed studies that would show the values one could expect for c_{min} . The value will generally depend on environmental conditions and will vary between different plasmids due to different metabolic costs paid by the plasmid hosting cell. The study in [146] hints at the expected c_{min} values and shows that for the IncP family plasmid investigated there the glucose concentration below 0.2 mg/ml inhibits the plasmid invasion into a surface attached population. However, it appears to be the only study to date which aimed to directly measure the values of c_{min} for which conjugation occurs.

Cell density and other factors

As discussed in Chapter 1, bacterial colonies undergo the phase transition to nematic order when the density of cells increases. The study in [107] on rod-shaped cells predicts the existence of instability that increases the order by forming ordered domains deep inside the bulk of the colony. This in turn facilitates an increased cell-cell contact surface [96]. Another study in [171] used an individual-based experimental framework for real time observations of conjugation events of TOL IncP plasmids to show that there is a possible link between the relative orientation of mating cells and conjugation performance. The study shows that the number of transconjugants is largest when the contact surface between cells is maximized. Thus, based on these studies the conjugation performance should be better in high-density spatially structured populations of rod shaped cells where preferred orientation of mating cells is facilitated. These are indeed the observations made in [149, 201], where increasing the initial colony densities of donors and recipients gives significant increases to the amount of transconjugant. Other studies in [149, 201] also addressed other possible factors such as environmental temperature and humidity. The evidence in there shows

that there exists the optimal temperature at which conjugation gives the best performance and that depends on the type of cells and plasmids. These factors, however, are out of scope of the simulation framework in this thesis.

4.2 Aims

The review above outlined the importance of conjugative junctions and other factors that impact the conjugation performance. Implementing these factors into the code developed in Chapter 3 will allow better, mechanical modeling of conjugation in spatially expanding communities. Modeling junctions as physical objects that keep the mating pair together will allow one to capture and investigate some of the physical factors that affect the conjugation performance. For example, the relative motion of cells in the mating pair could result in shear forces that act on conjugative junctions between cells and break that connection. In such a case, the effect of strain on the junction will be determined by the mechanical properties of the junction and the biological aspects of the conjugation process. The aim of this chapter is to develop, parametrize and test the mechanical model of the conjugation process that will allow one to explore this phenomenon in different scenarios, such as circularly symmetric growth and conjugation on the collision front of two head-on colliding bacterial colonies. The additional motivation comes from experimental observations on colliding colonies detailed in section 4.5, where the effect of shear forces on conjugation is examined. The r702 plasmid of the IncP family used in the laboratory at The University of Edinburgh is used here to set and review some of the parameters in the model developed in this chapter.

4.3 Details of the algorithm

The conjugation procedure in this chapter is an extension of the existing simulation framework developed and described in Chapter 3. Similarly to Chapter 3, the restriction is that one donor can mate with one recipient at a time only and all plasmids are neutral. However, now there are additional contributions from factors that are discussed in the previous section. The conjugation process is not instantaneous anymore and is set to take $t_c = 4$ minutes to complete. The value corresponds to the one obtained for IncP plasmid in [170] and further supported

by more studies [170, 192, 202, 203]. Cells can conjugate when in mechanical contact with each other, however to account for pilus action at a distance the conjugation can be initialized if the distance between two cells is less than some minimum value D_{max}. Experimental assays in [173, 188, 204] show that the shortest pilli have the length of an order of 100 nm, and thus $D_{max} = 100nm$ is set to reflect these observations. Newly formed tranconjugant cells can conjugate only when their lag period is over. With reference to the previous discussion and based on results in [170] the lag time is set to $t_{lag} = 5$ minutes of physical time. Based on the discussion in section 4.1.2, conjugation starts only when $c(x, y) > c_{min}$ at the moment of conjugation initialization. Note, however, that at least c_{thres} is required for cells to grow (see section 3.4.1) and thus c_{min} should be larger than c_{thres} to have any effect on conjugation. Based on observations in [146] the value of $c_{min} = 0.2fg/\mu\text{m}^2$. The next section details the implementation of conjugative junctions.

4.3.1 Conjugative junctions

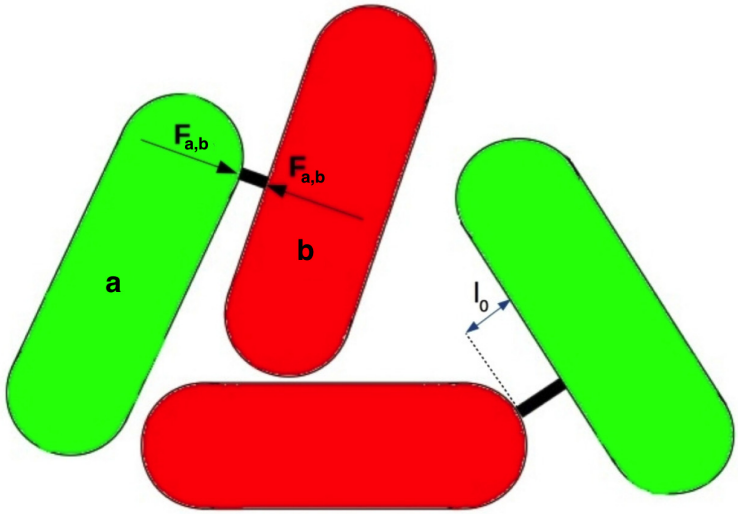

Figure 4.3 *A plasmid donor cell (red) mates with a plasmid recipient cell (green). The conjugative junction of length l_0 is created with rate m_j between two closest points $\vec{r}_{aj}$ and $\vec{r}_{bj}$ that lie on the surfaces of mating cells a and b. The junction is a spring-like object that acts on both cells with elastic force $F_{a,b}$.*

When two cells are found in favourable contact mechanical contact and conditions for conjugation initialization are met, the conjugative junction is created with rate m_j [h^{-1}]. Conjugative junctions are assumed to be narrow tubular objects

made up of the same material as the cell wall, see Fig. 4.3. They are modelled as Hookean spring-like objects that are associated with the force $\mathbf{F}_{a,b}$ that acts between the two mating cells a and b. The force is proportional to the spring constant k and the change in the junction length due to cell displacements is Δl. The plasmid transfer takes $t_c = 4$ minutes of physical time and if the strain $\sigma_{a,b}$ on the junction gets larger than σ_{max}, where σ_{max} is the maximum strain on the junction before it breaks, the plasmid transfer is unsuccessful. The following algorithm shows the implementation of the conjugation process and is evaluated for every system increment time dt:

1. Out of N cells pick up two neighbouring cells a and b.
2. Check for their types. If types do not match the ones required for conjugation then continue to the next pair of cells.
3. Otherwise, check if conjugation between a and b is already in progress and if the corresponding junction exists.
4. If the conjugation process is not in progress yet:
   (a) If one of the cells is transconjugant check the time t_p that has passed from the previous plasmid capture. If $t_p < t_{lag}$, increase t_p by dt and continue the next pair of cells.
   (b) Otherwise, check if the minimum distance between cells $d_{a,b} < D_{max}$ and if $c(x, y) > c_{min}$ at the cell centers of masses. Break if false and continue to the next pair of cells.
   (c) Otherwise, create a junction with probability $m_{\mathrm{j}} \times dt$ by picking the random number m_p^* such that $m_p^* \in [0; 1]$.
   (d) Initialize conjugation if $m_p^* \leq m_{\mathrm{j}} \times dt$, otherwise repeat the previous step during the next system update given that all the other requirements are fulfilled again.
   (e) Find the two closest points between cells and attach the junction at these points.
   (f) Record the initial junction length l_0 based on its attachment points $\vec{r}_{aj}$ and $\vec{r}_{bj}$ to cells a and b respectively. Set the time-counter of this conjugation process to 0.
   (g) Continue to the next pair of cells.

5. Else if conjugation is in progress:

   (a) If the conjugation between a and b lasted for time $t = t_c$ change the recipient cell type to the transconjugant, set its lag time counter to 0, remove the junction and move to the next pair of cells.

   (b) Otherwise, recalculate the new length l of junction due to cell displacements and growth (see section 3.4.1)

   (c) Calculate the strain on junction $\sigma_{a,b} = \frac{\Delta l}{l_0}$, where $\Delta l = l - l_0$. If $\sigma_{a,b} > \sigma_{max}$ stop conjugation, break the junction and continue to the next pair of cells.

   (d) Otherwise, evaluate the elastic force $\mathbf{F}_{a,b} = -k\Delta l\vec{r}_{aj,bj}$ that acts along the junction. Note that $\vec{r}_{aj,bj} = (\vec{r}_{aj} - \vec{r}_{bj})/(|\vec{r}_{aj} - \vec{r}_{bj}|)$ is the unit vector between junction attachment points on cell walls.

   (e) Add the force contribution $\mathbf{F}_{a,b}$ to $\mathbf{F}_{net}$ in Eq.(3.19). Similarly, add the resulting torque contribution $\tau_{a,b}$ due to $\mathbf{F}_{a,b}$ to torques on cells a and b, see Eq.(3.20).

   (f) Update the time counter of this conjugation process and move to the next pair of cells

6. Repeat the above steps N times

In step 1 of the above algorithm, cells are evaluated for neighbourhood by checking the minimal distance and contact between cell envelopes. Only when the distance between cells is smaller than D_{max} cells are considered to be neighbours and the junction can be formed. Note that for optimizing the procedure, the algorithm from Section 3.4.1 is used. The continuous space is subdivided into the grid of square boxes. For any cell a that sits in a given box cell b is picked up only from cells that sit in surrounding boxes. This makes the algorithm to scale in time as $O(N)$, where N is the total number of cells. It is also important to point out that if during the conjugation process one of the mating cells divides, the junction is broken and conjugation is not successful.

4.4 Parameters and simulations

4.4.1 Parameters k and σ_{max}

There are three parameters that characterize the junction and associated conjugation performance: the mating pair junction formation rate m_{j}, the maximum strain before the junction breaks σ_{max} and the junction spring constant k. The conjugation algorithm in section 3.4.1 has only one parameter μ which determines the performance of conjugation. Here m_{j}, σ_{max} and k all contribute to plasmid transfer dynamics and the net effect is the conjugation rate which is some unknown function of m_{j}, σ_{max} and k.

The estimation of expected value of k to be used in simulations can be based on the assumption that the conjugative junction is a part of cell envelope. This seems reasonable based on the observations in [173]. Assume the junction is a tube of diameter d_j with the axial hole d_{ax} and the cross-sectional area $A_j = \pi/4 \times (d_j^2 - d_{ax}^2)$ [204]. The bacterial cell elastic modulus is E_b and the junction of initial length l_0 is subject to forces due to cell displacements that change its length by Δl. The result of this extension is strain on the junction that is related to force by:

$$|\mathbf{F}_{a,b}| = k\Delta l = A_j E_b \Delta l / l_0 \tag{4.2}$$

which gives the expression for k

$$k = A_j E_b / l_0 \tag{4.3}$$

The value of E_b for the *E.coli* cell is of the order of 100 MPa [205]. The value of l_0 is the initial length of junction, however as discussed before the experimental assays are not conclusive about the exact nature of junctions [173]. Observations indicate that bacteria can conjugate when the distance between cells is of the order of IncP pilus length, that is $\sim 1 - 5 \times 10^{-7}$ meters [173, 188, 204]. Thus, it seems reasonable to set $l_0 = 10^{-7}$ meters, which also corresponds to D_{max} used in simulations. Observations of pilli in multiple assays [173, 188, 204] allow one to evaluate the value of A_j based on the value of d_j, which is quoted to have around 10^{-8} meters with the axial hole of diameter $d_{ax} = 5 \times 10^{-9}$ meter. Thus,

for $A_j = \pi/4 \times (d_j^2 - d_{ax}^2) \approx 60 \times 10^{-18} m^2$. Substituting these values into Eq.(4.3) gives $k \approx 6 \times 10^{-3} N/m$, which after rescaling to dimensions used in simulations gives $k \approx 6 \times 10^{-9} N/\mu m = 6nN/\mu m$.

What remains to be determined is the critical strain above which the junction breaks. Naively, one could assume that it corresponds to the range of displacements (over time intervals $t_c = 4$ minutes) that are normally found between between cells that live in a dense micro-colony. Simulations of colonies with no conjugation suggest cell displacements of the order of $1 \times 10^{-8} - 5 \times 10^{-7}$ per 4 minutes, which gives $\sigma_{a,v} \rightarrow [0.1; 5]$. This suggests that the junction could be stretched by a factor of up to 5 before it breaks, which seems highly unrealistic, given the strength of common materials [206, 207]. Moreover, the evaluation above assumes displacements as if no junction existed between cells, and hence the force contribution due to the junction is not considered. The range of values for $\sigma_{max} < 1$ seems like a more reasonable and realistic choice, given the values for common materials and given that the presence of a conjugative junction should restrain the relative motion of two mating cells and hence decrease Δl significantly. Further numerical studies in the next sections shed more light on the effect of σ_{max} on the conjugation performance.

4.4.2 Junction formation rate m_{j}

The deduction of m_{j} by the analysis similar to the above is not possible as there is no data available on junction formation rates in bacterial communities. The difficulty of directly measuring m_{j} is due to an inability to experimentally distinguish between stages of conjugation process, and in particular, in tracing the moment of the initialization of junction formation. However, the experimental data obtained for r702 plasmid used in The University of Edinburgh laboratory coupled together with simulations, might allow to get a rough estimate values of m_{j} expected for the r702 plasmid. Angela Dawson (The University of Edinburgh) performed the experimental assay to investigate plasmid dynamics for r702. Multiple colonies of 50:50 donor to recipient ratio of E.coli cells were exponentially grown on the filter plates for 3 generations. Donor cells hosted r702 conjugative plasmid with fluorescent protein being expressed after the successful plasmid transfer. After 3 generations the optical microscopy assay allowed her to measure transconjugant to donor(T/D) and transconjugant to recipient (T/R) ratios giving T/D=0.033 and T/R=0.17 respectively.

Simulations can be used to estimate m_j which would result in T/R and T/D ratios similar to these found in experiments. Fixing the value of $k = 6nN/\mu m$ and setting $\sigma_{max} \in [0.01; 0.2]$ allows one to run simulations for different values of m_j. To simulate the experimental conditions a single cell is seeded and allowed to expand into the colony of size $N = 500$ cells. Nutrients are set to c_0 and are replenished at the every simulation update step to make the colony grow exponentially. When $N = 500$, all cells in the colony are randomly assigned the donor or recipient type, so that a 50:50 culture is obtained. It is then grown for a further 3 generations and bacteria are allowed to conjugate according to the algorithm detailed in the previous section. When $N = 4000$, the number of specific types of cells are measured and the corresponding T/D and T/R ratios obtained. 30 independent simulations are run to get a good statistics of results.

Simulation results

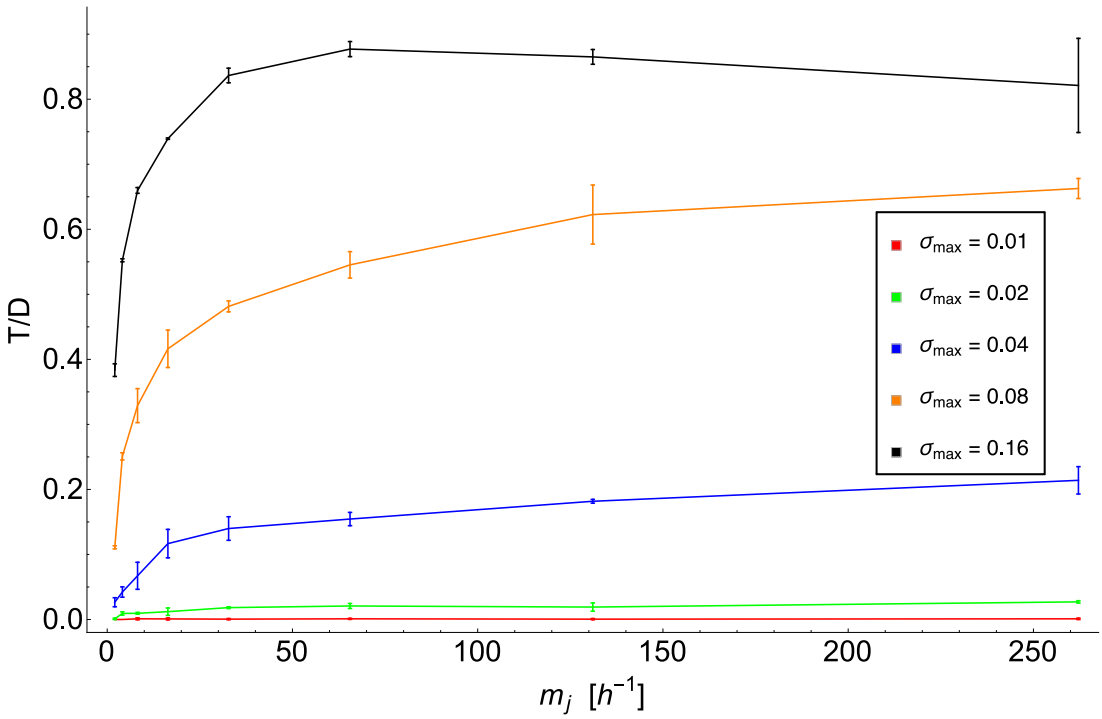

Figure 4.4 *T/D ratios obtained from simulations for different conjugation initialization rates* $m_j \in [2 : 260]$. *Colours correspond to different* σ_{max}*:* 0.01 *(red),* 0.02 *(green),* 0.04 *(blue),* 0.08 *(orange),* 0.16 *black. Most of the T/D values are higher than the values obtained throughout experimental assays for the r702 plasmid. At very small values* m_j *impacts the conjugation performance, however, for larger values the effect decreases.*

The range of values investigated for $m_j \in [2 : 260]$ per hour. Figures 4.4 and

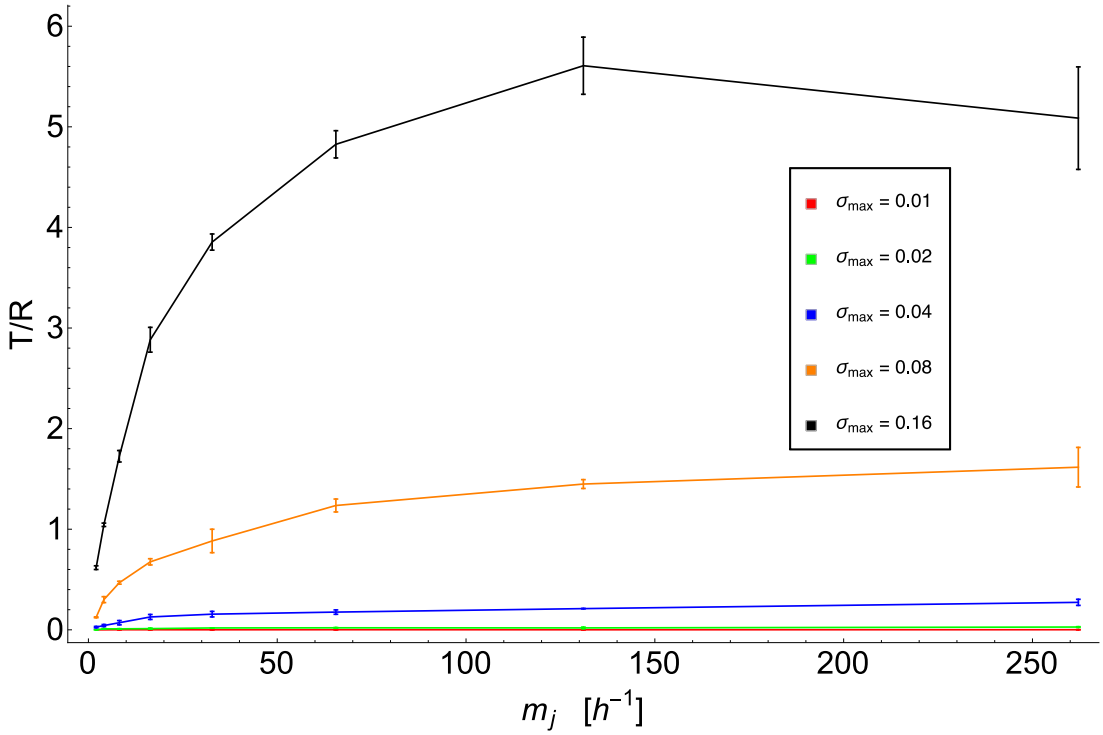

Figure 4.5 *T/R ratios obtained from simulations for different conjugation initialization rates* $m_j \in [2 : 260]$. *Similarly to Fig. 4.4 colours correspond to different* σ_{max}*:* 0.01 *(red),* 0.02 *(green),* 0.04 *(blue),* 0.08 *(orange),* 0.16 *(black). Similar trend to that in Fig. 4.4 is observed and ratios in both plots show that conjugation performance is sensitive to the value of* σ_{max}.

4.5 show the results of simulations where colours correspond to different values of σ_{max}, as described in the figure caption. In comparison to the experimental values of T/D=0.033 and T/R=0.17, the results obtained from simulations are generally larger for the investigated set of σ_{max} and m_j values. However, for $\sigma_{max} = 0.04$ and $m_j = 4$ h^{-1} the T/D ratio is 0.039 ± 0.009, while for $m_j = 8$ h^{-1} the T/D ratio is 0.068 ± 0.027. Both of these values are of the same order of magnitude as the experimental value of T/D=0.033. Similarly, the obtained T/R ratios are generally larger and as in the case of T/D, only a limited set of m_j values give T/R of the same order of magnitude as in experiments. For $\sigma_{max} = 0.04$ and $m_j = 4$ h^{-1} the T/R ratio obtained in simulations is 0.051 ± 0.012, for $m_j = 8$ h^{-1} the T/R ratio is 0.089 ± 0.024, while for $m_j = 16$ h^{-1} the T/R ratio is 0.119 ± 0.038. Although the obtained values do not exactly match the experimental observations, they allow one to estimate the range of m_j that could be expected for the r702 plasmid: $4 < m_j < 8$ h^{-1} for $\sigma_{max} = 0.04$. Hence, the range of these values can be used to explore the phenomena associated with this particular plasmid (r702), as seen later in this chapter.

Note also the clear trend in Figures 4.4 and 4.5. Only for very small values the m_{j} parameter impacts the conjugation performance. As m_{j} increases both T/R and T/D get flatter across the range of m_{j} values investigated. The surface attached colony is dense and cells stay in mechanical contact with each other. The m_{j} parameter should only impact the number of transconjugants when the junction formation rate is very small and comparable with the lifetime of the cell and the time it takes for conjugation to complete. Assuming the mean lifetime of a bacterium $t_{mean} \approx 20min$, for $m_{\mathrm{j}} = 3$ there will be, on average, one junction per cell life-cycle formed. As m_{j} increases the average number of junctions formed increases and hence more transconjugants can be produced. However, when $m_{\mathrm{j}} \approx 15$ the characteristic time of junction formation $1/m_{\mathrm{j}}$ is ≈ 4 minutes. This corresponds to one junction formed per $t_c = 4$ minutes (that is, the time required for the conjugation process to complete) and any further increase in m_{j} should have a smaller and smaller impact as the conjugation performance is now bottlenecked by t_c. Hence, the observed decrease in the rate of change in T/R and T/D as m_{j} gets large. Assuming that one wants to avoid m_{j} being the limiting step for conjugation performance, the value of this parameter should be at least of the order of 100 per hour to decrease its impact on the transconjugant number.

Results show that σ_{max} is an important factor determining the fate of plasmid in population. The trend is clear when one plots σ_{max} vs T/R, as seen in Fig. 4.6. Each data point corresponds to the measurement taken when the colony size $N = 4000$. $m_{\mathrm{j}} = 260$ h^{-1} so it does not affect the number of transconjugants. For very small values of σ_{max} there are hardly any transconjugants present and so T/R is low. The observed trend is that for an increasing value of σ_{max} the number of T cells is increasing as well. Thus, the stability of the physical connection between mating cells and its resistance to breaking due to shear that results from the relative motion of cells appears to be of big importance in the conjugation process. Note, however, that while for larger values of σ_{max} the number of transconjugants appears to increase linearly with σ_{max}, then for smaller values of $\sigma_{max} < 1$ there is a non-linear increase in the T/R ratio. As shown in the later section 4.5.2, for smaller values of σ_{max} the role of k becomes important in stabilizing the mating pair. Thus, it is possible that the interplay between σ_{max} and k is responsible for the observed non-linearity for $\sigma_{max} < 1$ in Fig. 4.6.

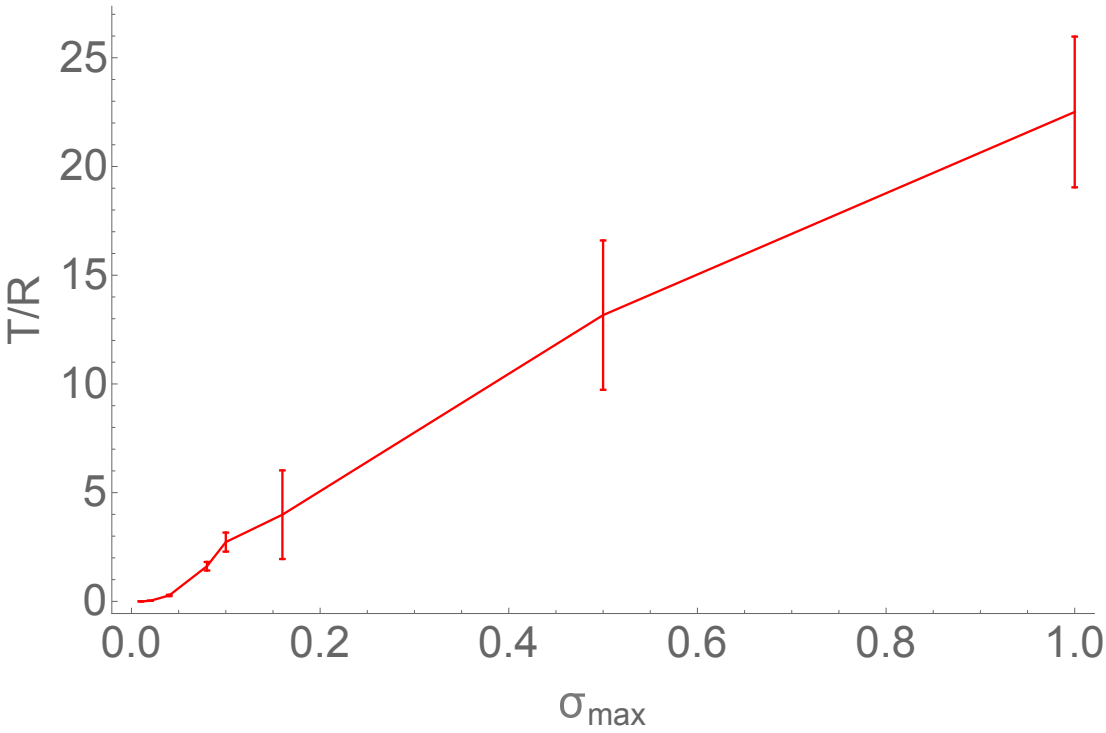

Figure 4.6 *Plot of σ_{max} vs T/R for the final colony size $N = 4000$ cells. The relationship is linear and increasing the value of σ_{max} results in more transconjugants observed. The plot indicates that the mechanical properties of junctions are of great importance for conjugation performance. Note that for larger values of σ_{max}, the T/R ratio gets very high, indicating the high amount of plasmids in the population.*

k=0

By virtue of Eq.(4.2), the magnitude of force due to junction $\mathbf{F}_{a,b}$ is scaled by the parameter k. Hence, when $k = 0$, the junction does not contribute any force to the net force acting between cells. By performing simulations with the same setup as above but now with $k = 0$, one observes the effect of junction on the mating pair stabilization.

30 independent simulations are performed for the case where $k = 0$. Starting from a single cell, colonies are grown exponentially up to the size of $N = 4000$ cells. Then T/R and T/D ratios are recorded. Simulations are performed for a set of σ_{max} and m_{j} values. Fig 4.7 shows an example of obtained results for $k = 0$ and compared to the cases seen in Fig. 4.5 where $k = 6nN/\mu m$, as is indicated in the figure caption. The effect that junctions have on the conjugation performance is evident. For any value of m_{j} considered the T/R ratios are much higher when $k = 6nN/\mu m$ as compared to the $k = 0$ case. The force from the junction reduces

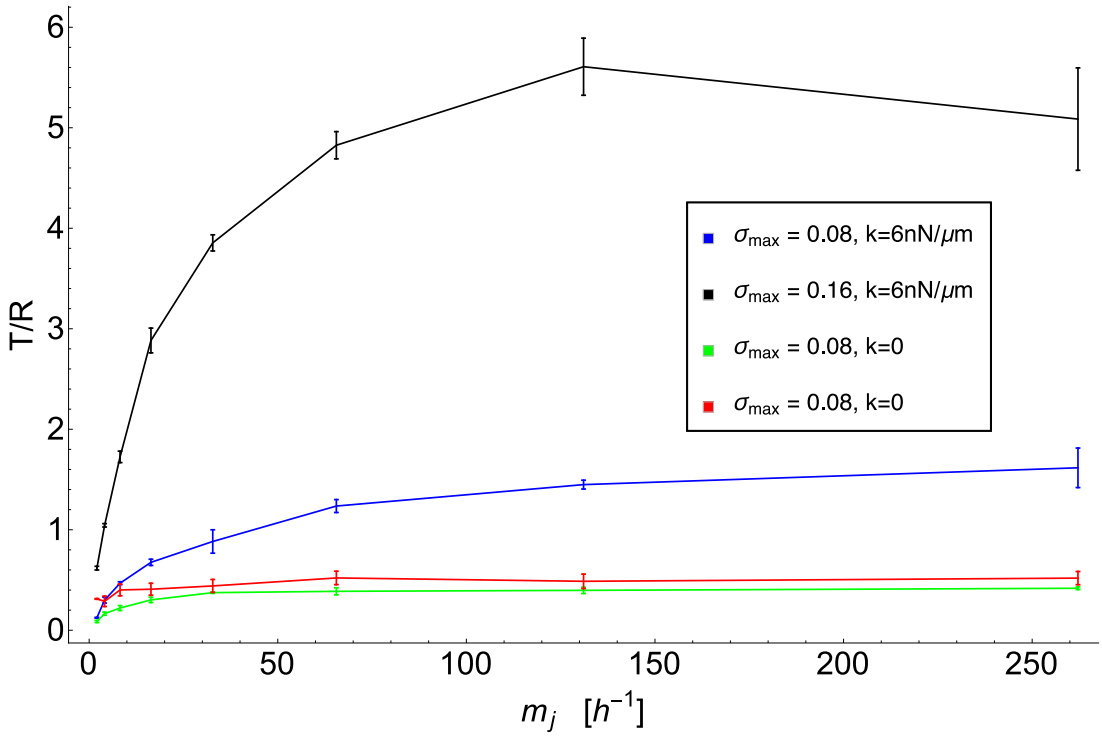

Figure 4.7 *Blue (σ_{max}=0.08) and black (σ_{max}=0.16) plots show the T/R ratios obtained in case where $k = 6nN/\mu m$. Green (σ_{max}=0.08) and red (σ_{max}=0.16) plots show the T/R ratios in case of $k = 0$. For all the values of σ_{max} and m_j considered here the number of transconjugants is higher in the case where $k = 6nN/\mu m$. The force from the junction causes the adhesion of mating cells and reduces the relative displacements that would otherwise result in breaking the conjugation process.*

down the relative displacements of cells in the mating pair significantly and thus, conjugation can continue since the displacements do not exceed Δl for which the conjugative junction breaks. Changes in k and their effect on the conjugation performance are further explored in section 4.5.

Summary of parameters

Following the estimation of parameters in previous sections, Table 4.1 sums up their respective values (or the range of values). Note that for σ_{max} and m_j two cases are distinguished. For σ_{max}, the first case corresponds to the r702 plasmid, while the second case considers a larger set of values that came from estimations in section 4.4.1. Similarly, based in Figures 4.4 and 4.5, the first case of m_j corresponds to the r702 plasmid, while the second case gives the range of values for which m_j does not affect the conjugation performance in simulations significantly.

Parameter	Values used
Transconjugant lag phase t_{lag}	5 minutes
Time for conjugation to complete t_c	4 minutes
Maximum separation between cells before conjugation D_{max}	$D_{max} = 100$ nm
Segregative plasmid loss rate p_{seg}	0.05 per division event
Threshold nutrient concentration c_{min}	0.2 fg/μm^2
Junction spring constant k	6 nN/μm
Maximum strain σ_{max} on junction	$\sigma_{max} = 0.04$ for r702, $\sigma_{max} < 1$ otherwise
Junction formation rate m_{j}	$4 < m_{\mathrm{j}} < 8$ h^{-1} for r702, $m_{\mathrm{j}} > 100$ h^{-1} otherwise

Table 4.1 *The table of parameters and their estimated values*

4.5 Collisions

The simulation framework that has been developed in this chapter can be used to study the effects that the mechanical forces acting on the mating pair have on the conjugation dynamics. In particular, this chapter considers the case of colliding colonies. Two single cells are initially separated by distance S_{in}, where one cell is of the donor type and the other is of the recipient type. Cells are allowed to develop into recipient and donor colonies that grow exponentially up to the point when they collide with each other. At this point, recipients at the collision front can mate with donors.

This section is motivated by experimental observations in the laboratory assays at The University of Edinburgh. The r702 plasmid donor and recipient colonies were grown on agar plates and collided with each other, see Fig. 4.8. The number of fluorescent transconjugants was measured with the use of an optical

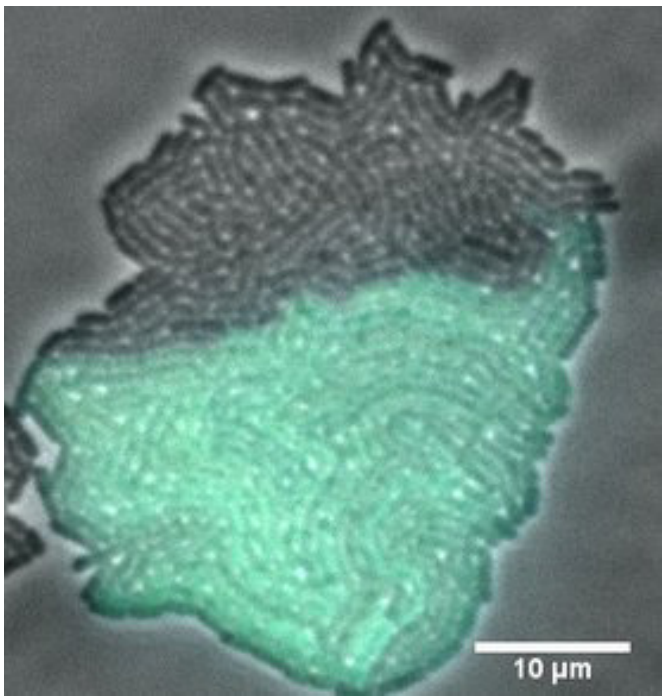

Figure 4.8 *The optical microscope image of colliding r702 plasmid donor (green) and recipient (gray) colonies. Transconjugants would manifest themselves as cyan patches at the collision front. As seen in the picture no transconjugants are present, even though r702 is known to perform relatively well in surface attached colonies. Image courtesy: Diarmiud Lloyd, the University of Edinburgh.*

microscope and no transconjugants were observed in any of the collision assays. This was quite a surprising result, since as discussed in Section 4.4.2, the r702 plasmid gives rise to a significant number of transconjugants (T/R=0.17 and T/D=0.033) when allowed to conjugate in colonies grown on filter plates. It could be possible that the growth conditions were not adequate for r702, however care was taken to ensure that collision assay was performed in appropriate nutrient, humidity, pH and temperature conditions. Another explanation could be that shear forces acting on the collision front due to the relative motion of cells were large enough to break the conjugative junctions and hence, reduce down the conjugation performance. Although there exists some previous research that indicates the limited impact of shear on mating aggregates observed in well mixed environments [192, 193], the quoted results are purely qualitative and applicable only to the well-mixed environments.

The simulation framework in this chapter can be used to shed some light on the effects associated with shear forces at the collision front in surface attached communities. By increasing S_{in} (i.e the initial distance between centers of colonies), one can increase the colony radius r at which the collision occurs. Note

that for a colony that grows exponentially the number of cells $N \propto 2^{\frac{t}{T}}$, where t is the time of the colony growth and T is the doubling time of the bacterial cell. Thus, the colony radius $r \propto \sqrt{N} = 2^{\frac{t}{2T}}$ and so the radial colony expansion velocity $v_{rad} = \frac{dr}{dt} \propto 2^{\frac{t}{2T}} = r$. Thus, since the radial colony expansion velocity $v_{rad} \propto r$, larger S_{in} implies larger impact velocity v_{imp} at the collision front. For larger v_{imp} the relative motion of mating cells at the collision front will be more profound, and this might result in cell displacements that can break conjugative junctions. Thus, by changing S_{in} and by measuring the total number of transconjugants on the collision front, one might get a view on a possible relationship between the magnitude of the relative motion of cells and the conjugation performance in the case where two colonies collide.

4.5.1 Simulation setup and methods

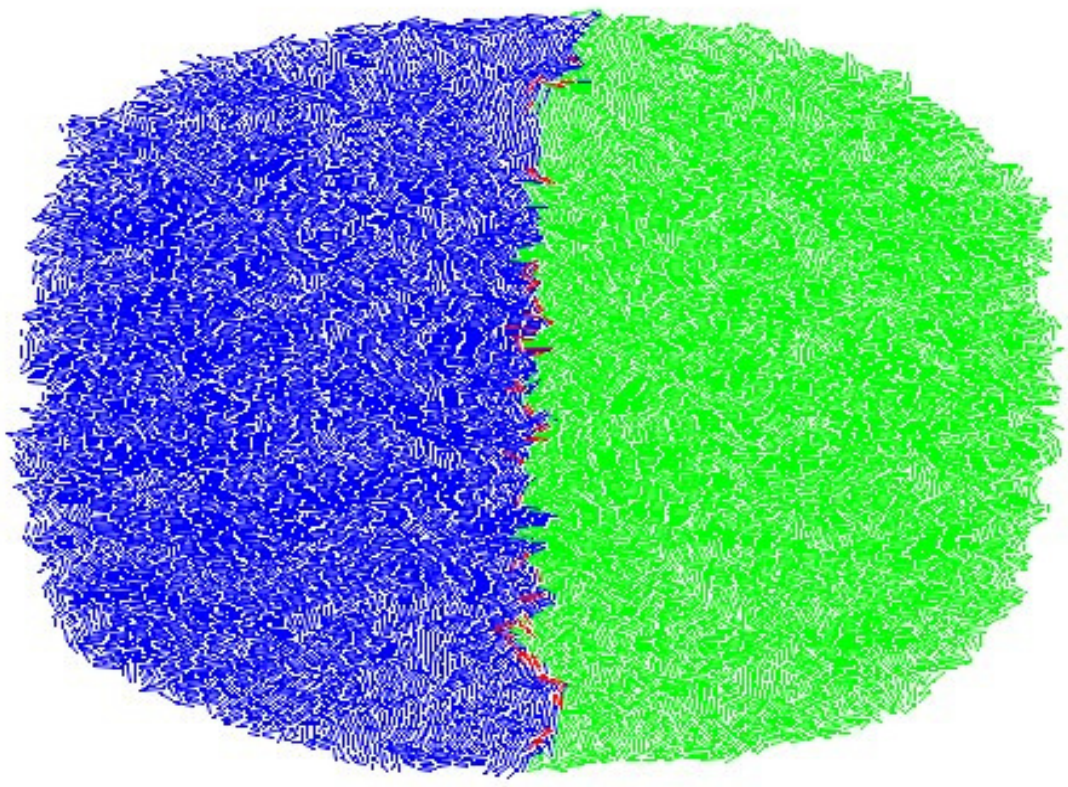

Figure 4.9 *The example simulation snapshot of colliding colonies. Donor (blue) and recipient (green) colonies start their growth from single cells separated by the initial distance S_{in} and are allowed to grow until they collide. Conjugation at the collision front results in red transconjugants.*

Simulations are initialized with two colonies which are seeded with one donor and

one recipient cell separated by distance S_{in}. The values of S_{in} under consideration are: 5 μm, 10 μm, 15 μm, 20 μm, 25 μm, 30 μm, 35 μm and 40 μm. Nutrient concentration $c(x, y) = c_0$ at the every simulation update step so that colonies grow exponentially. Colonies are allowed to grow and collide and cells can conjugate at the collision front according to the algorithm in section 4.3.1. The growth is continued until the collision front reaches the length of $L = 25\mu m$. This value of L corresponds to the collision front lengths observed in experimental assays, as seen in Fig. 4.8. When $L = 25\mu m$, the measurement of the total number of transconjugants and the number of transconjugants per L is performed. The values of parameters corresponding to the r702 plasmid are set accordingly: $\sigma_{max} = 0.04$, $k = 6nN/\mu m$, $m_j = 8\ h^{-1}$. However, in later subsections the restriction on these parameters is reduced and the wider set of values of σ_{ma} and k values is explored. Fig. 4.9 shows an example snapshot obtained in simulations, with red patches of transconjugants visible at the collision front.

4.5.2 Simulation results

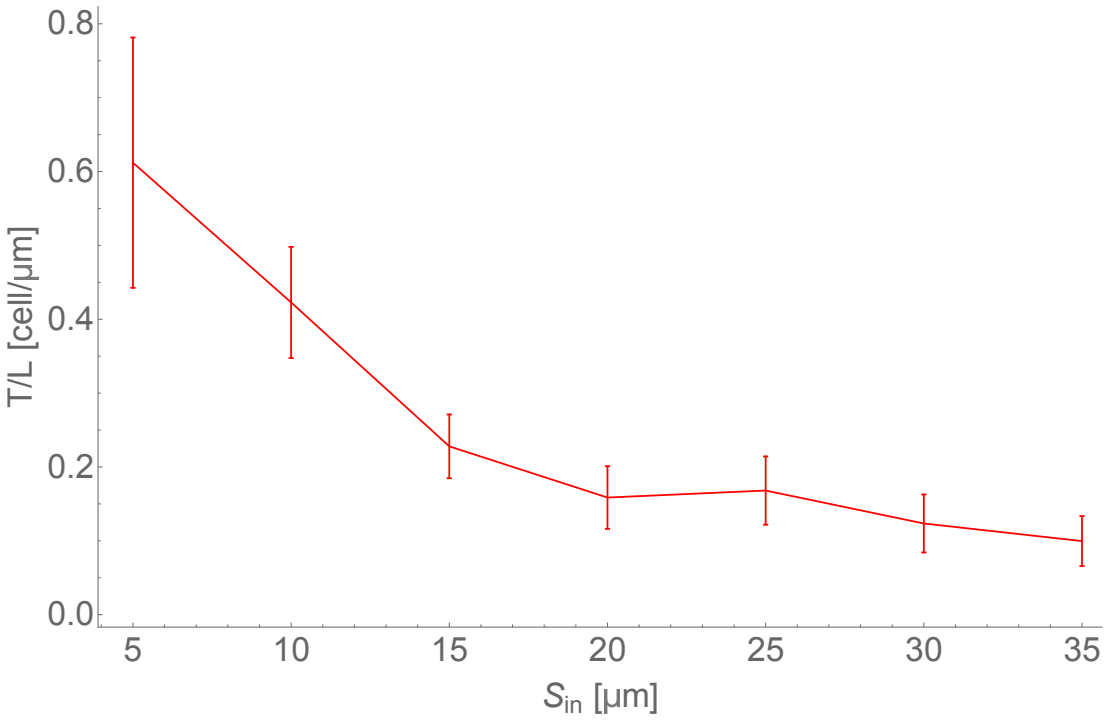

Figure 4.10 *The number of transconjugants per front length (T/L) vs S_{in}, simulations for the r702 plasmid ($\sigma_{max} = 0.04$, $k = 6nN/\mu m$, $m_j = 8\ h^{-1}$). The decrease in T/L for the increasing value of S_{in} shows that the relative motion of cells on the collision front can affect the conjugation performance and reduce the number of transconjugants significantly.*

Fig. 4.10 shows the number of transconjugants per front length (T/L) plotted against S_{in}, where every data point is averaged over 30 simulations and simulations are run with parameters estimated for the r702 plasmid. The T/L ratio decreases with increasing S_{in}, implying that the number of transconjugants is sensitive to the speed at which the colony collision occurs. As the shear on the collision front is larger for a larger S_{in}, results suggest that for a larger S_{in} shear is enough to break the conjugative junctions. Note, however, that the values of T/L do not go to zero for the range of S_{in} investigated. Even for larger values of S_{in} there are some transconjugants present at the collision front. The 7-fold increase in S_{in} and the collision force results in the observation of a few transconjugants at the collision front.

Varying σ_{max}

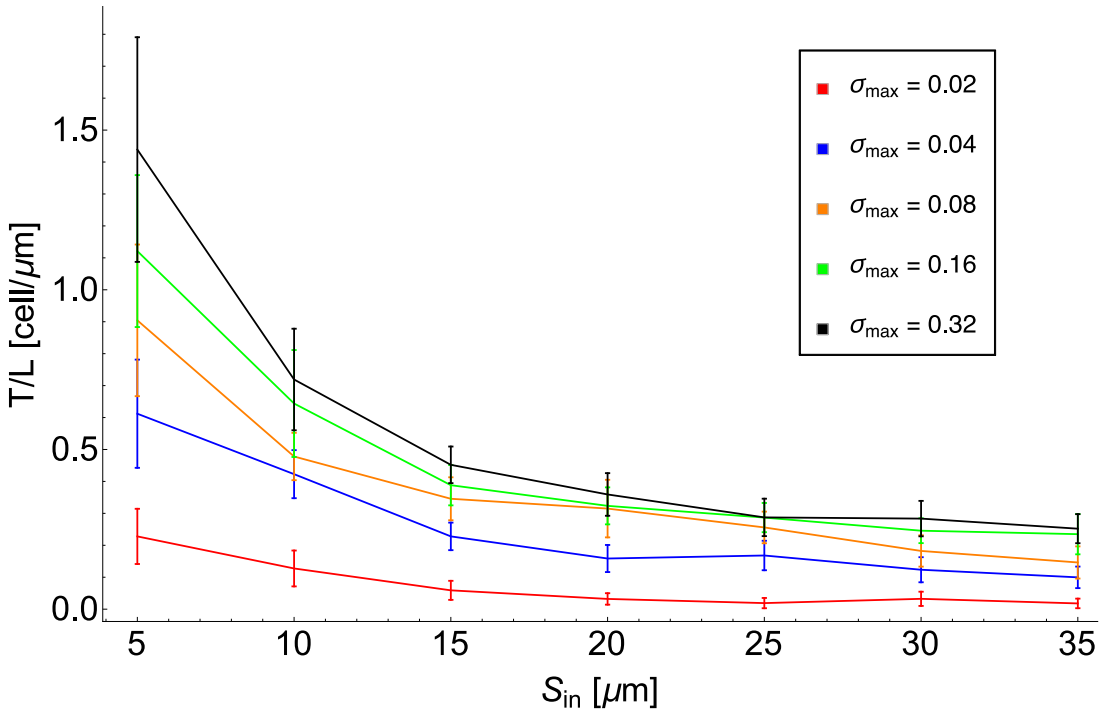

Figure 4.11 *The number of transconjugants per front length (T/L) vs S_{in}, for varying values of σ_{max}: 0.02 (red), 0.04 (blue), 0.08 (orange), 0.16 (green) and 0.32 (black). For larger values of σ_{max} less junctions are broken and more transconjugants are observed. These observations are similar to those for mixed cultures in 4.6 and show the impact of junction mechanical properties on the conjugation performance.*

Recall that the results in Fig. 4.6 indicated the importance of σ_{max} (that is, the maximum permitted strain above which the junction breaks) and its impact on

the conjugation performance. Simulations in this section can be used to further verify the effect of σ_{max} on the conjugation process. A set of simulations for colliding colonies is run for varying values of σ_{max}. The simulation set-up is the same as in the earlier sections, with the values of other parameters used corresponding to those estimated for the r702 plasmid: $k = 6nN/\mu m$ and $m_{\mathrm{j}} = 8$ h^{-1}.

Fig. 4.11 shows the plot of S_{in} vs T/L where every colour corresponds to a different value of σ_{max} used in the simulation, as indicated in the figure caption. Every data point corresponds to the average reading over 30 independent simulations. Plots in Fig. 4.11 show that when the maximum allowed strain on junction σ_{max} increases, the average number of transconjugants increases significantly for any value of S_{in} under consideration. Thus, the results in Fig. 4.11 are supporting those obtained for mixed colonies in Fig. 4.6 and highlight the significance of σ_{max} and its effect on the conjugation performance.

Varying k

Finally, it is worth taking a further look at the possible impact of the strength of elastic force $\mathbf{F}_{a,b}$ on the number of transconjugants. As already seen in Fig. 4.7, the value of the parameter k is an important element that determines the magnitude of force from a junction and hence, the result of conjugation. Here, a set of simulations is performed for different values of $k \in [0.5; 20]$ nN/μm that allow one explore the range around the estimated value given in Table 4.1. The value of $m_{\mathrm{j}} = 250$ h^{-1} so it does not bottleneck the conjugation process, and simulations are run for different values of σ_{max} and S_{in}.

Plots in Fig. 4.12 show the T/L ratio plotted against different values of the k parameter. The top plot corresponds to $\sigma_{max} = 0.08$ whilst the bottom plot shows the results for $\sigma_{max} = 0.32$. Different colours correspond to different values of S_{in}, as indicated in the figure caption, and every data point is the average over 30 independent simulations. Plots in Fig. 4.12 indicate that k impacts the conjugation performance, but only when σ_{max} is relatively small. For the case where $\sigma_{max} = 0.08$ and $k < 10nN/\mu m$, an increasing value of k results in larger T/L for all the values of S_{in} considered. When k gets larger than $10nN/\mu m$, its effect on T/L decreases and the k vs T/L plots get flat for all the values of S_{in}. When $\sigma_{max} = 0.32$, the value of k does not appear to impact the conjugation performance significantly.

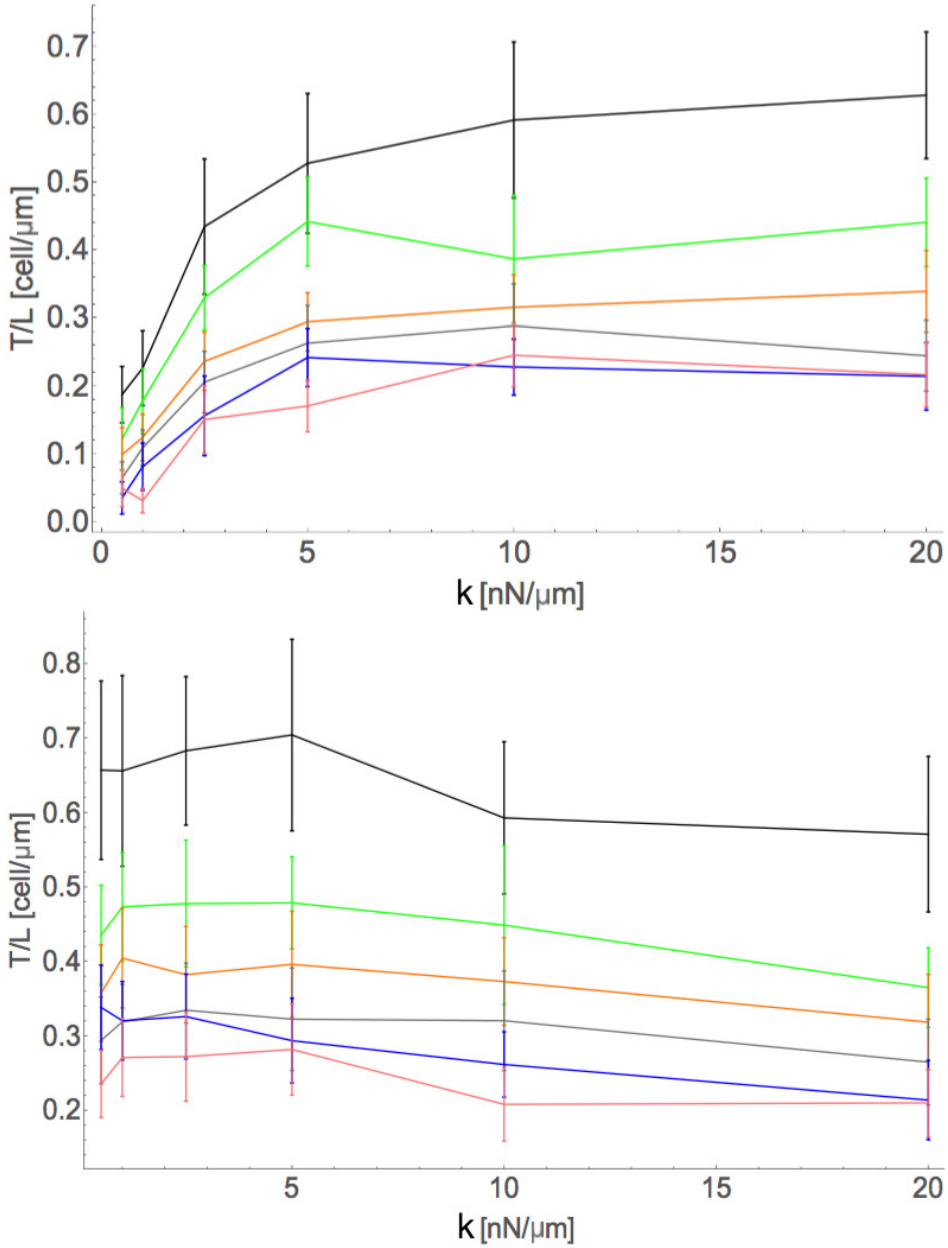

Figure 4.12 *The number of transconjugants per front length (T/L) vs k, with colours corresponding to different initial colony distances S_{in}: 10μm (black), 15μm (green), 20μm (orange) and 25μm (gray), 30μm (blue) and 35μm (pink). $\sigma_{max} = 0.08$ for the top and $\sigma_{max} = 0.32$ for the bottom plot. For smaller σ_{max} (top) the force on junction, which is determined by k, causes the stabilization of mating pair against displacements and the number of transconjugants increases with increasing k when $k < 10nN/\mu m$. On the other hand, when $\sigma_{max} = 0.32$ (bottom) the mechanical properties of junction are such that it does not break even for large strains. Thus, for large σ_{max} the impact of k on the number of transconjugants is not significant.*

To explain the observed trends, recall that the magnitude of the force from junction $\mathbf{F}_{a,b}$ is determined by the spring constant (see Eq.(4.2)). Thus, as k increases the increasing magnitude of $\mathbf{F}_{a,b}$ causes the stabilization of the mating pair against the relative cell displacements that could result in large strains on the junction that can break it, especially when σ_{max} is small. Hence, an observed increase in T/L due to the mating pair stabilization as the value k increases. However, as the value of k increases above a certain value the force from the junction is already strong enough to prevent any of the mating cells from large displacements. At this point, any further increase in k does not have any significant effect since cell displacements are too small to result in strains that would break conjugative junctions. This explains the flattening of plots for the large values of k observed in the top plot in Fig. 4.12. In comparison, when σ_{max} gets large the mechanical properties of the junction are such that it can sustain large strains due to cell displacements. In such a case a large magnitude of force $\mathbf{F}_{a,b}$ is not necessary to keep the mating pair together and so the effect of k on the number of transconjugants is neglible, as seen in the bottom plot in Fig. 4.12.

4.6 Summary

The simulation framework created in this chapter included the features that are observed to be important for conjugation performance. The implementation of conjugative junctions allowed one to investigate the mechanical aspects of the conjugation process. The investigation shows that there are three main parameters in the model which define the conjugation performance: junction formation rate m_{j}, maximum strain on the junction before it breaks σ_{max} and the junction spring constant k. The results in section 4.4.2 show that m_{j} affects the conjugation process but only when the characteristic time $(1/m_{\mathrm{j}})$ of junction formation is smaller or comparable to t_c, i.e time it takes to complete the plasmid transfer. Otherwise, the impact of m_{j} on conjugation is limited, as seen in Fig. 4.4. The results in sections 4.4.2 and 4.5.2 show that parameters k and σ_{max} are vital for the performance of conjugation. The value of σ_{max} is shown to significantly impact the conjugation performance, as seen in Figures 4.6 and 4.11, where increasing σ_{max} gives more observable transconjugants. Moreover, there exists an interplay between σ_{max} and k parameters. When σ_{max} is small, the junction breaks even for relatively small mating cell displacements. In such a

case larger values of k are needed to give the force from junction $\mathbf{F}_{a,b}$ that reduces the relative cell displacements. However, as σ_{max} increases, the junction becomes less susceptible to breaking. In such a case, the mating pair can sustain larger cell displacements before the junction breaks and thus, the change in k has no significant effect on the number of transconjugants, as seen in Fig. 4.12.

Results from simulations of colliding colonies performed for the r702 plasmid show that shear forces at the collision front can break conjugative junctions and affect the number of transconjugants. An increase in the relative cell motion at the collision front reduces down the observed number of transconjugants, as seen in Fig. 4.10. However, these observations can only partially explain the experiments where no transconjugants were observed for colliding colonies of the r702 plasmid. The initial distances S_{in} between colonies in experimental assays were of the order of $10 - 15\mu m$ and Fig. 4.10 suggests that for such distances a significant number of transconjugants should be observed. Even though the trend is such that T/L decreases with S_{in} and for large enough S_{in} one might expect no transconjugants at all, it is necessary to consider other possible factors and review some of the model assumptions. One should consider more experimental measurements on colliding colonies to further verify the effect of the relative cell displacement on conjugation performance. By colliding multiple colonies that arise from founder cells separated by different distances one should be able to obtain T/L measurements similar to those in section 4.5.2. Note that for the simulation setup used in section 4.5 the total number of cells in colliding colonies should not exceed $N\ 10^3$. Such colony sizes should be easily obtainable in good laboratory conditions, and hence by running multiple collision assays one should be able to further support the observations made in this section.

Furthermore, as discussed in the introductory section of this chapter, to date only a limited amount of research and data about the conjugation mechanics exist. Thus, a certain number of assumptions had to be made for modeling purposes in this chapter. It is possible that modeling junctions as spring-like objects acting on the mating pair with the Hookean force is an oversimplification. It was assumed that the junction is made of the same material as the rest of the cell's envelope, however, even in such a case the behavior of such material under large stresses is not fully understood. This could possibly affect the relationship between forces acting on mating pair and the conjugation performance. Moreover, the simulation framework in this chapter included only a limited amount of factors that are observed to contribute towards the conjugation mechanism. The focus was put

on conjugative junctions and the associated mechanical impact on conjugation. It has been noted in section 4.1 that environmental factors such as pH, temperature and humidity might have an observable impact on plasmid transfer. The relative orientation of mating cells might possibly affect the conjugation performance, as experimentally observed in [171]. Furthermore, the simulation framework considers only neutral plasmids and it has been pointed out in Chapter 1 as well as in section 4.1.2 that plasmid fitness cost and benefit towards the host cell is an important factor that affects the plasmid conjugation and plasmid fixation in populations. All the above observations and factors could possibly account for differences between simulations and experiments for colliding colonies. Yet, the observed trends fit the predictions and make physical sense. Thus, one can conclude that the simulation framework developed in this chapter successfully captures some of the effects associated with the conjugation process and its mechanics.

Chapter 5

Summary of the thesis and future work

The aim of this thesis was to explore the phenomena associated with biophysics and horizontal gene transfer in growing microbial communities. Simulations in Chapter 2 investigated the two dimensional Eden model of micro-community growth for its dynamic scaling properties. The numerical results showed that the scaling properties of the growing interface are not significantly affected by the shape of cells that give rise to Eden clusters. In all the cases considered the dynamic scaling of the growing interface was shown to follow that predicted by the KPZ model that is characterized by the growth exponent $\beta = 1/3$, the roughness exponent $\alpha = 1/2$ and the dynamic exponent $z = 3/2$. Only in the case of spatially correlated cells was the initial phase of the cluster growth shown to be different than that predicted for the KPZ growth. However, the effect of spatial correlations was shown to quickly disappear after the memory of initial configuration is lost due to system thermalization and the KPZ scaling was shown to be retrieved for longer times of growth.

It would be interesting to extend the study in Chapter 2 into the third dimension. The research in past years has already shown that for both lattice-based and the off-lattice Eden growth with symmetric (spherical) cells the observed dynamic scaling can belong to the KPZ universality class [116, 119], yet the cases with non-spherical cells in 3D and above have not been investigated. Based on results in Chapter 2, one could possibly expect no differences might be observed in the 3D case, however, care needs to be taken when extrapolating these results

into higher dimensions before thorough study. Further simulations of growing interfaces at the end of Chapter 2 hinted that the KPZ-like growth might not be universal for all the cases of growing clusters and might be relevant only when the growing front is narrow. For wider fronts simulations of microbial communities suggest the roughness exponent $\alpha = 1/3$, which implies the non-KPZ scaling. Further work needs to be done on the effect of the front width on the dynamic scaling, with detailed studies of both small and large t regimes to infer the characteristic β, α and z exponents for different cases of clusters growing in two dimensions. The numerical and analytical study should be supplemented with experimental measures on real, growing colonies. Changing the width of the front might be facilitated by manipulation of the nutrient medium. However, one might expect problems with confining the colony growth in two dimensions, as the transition to third dimension can happen due to buckling forces inside the colony [29]. Such a transition might possibly impact the dynamic scaling of the colony and thus, one would need to find a way to avoid this type of growth. A simulation framework that includes mechanical details of colony growth, like the one developed in Chapter 3, could further aid an experimental investigation of the interface scaling. Research shows that the roughness of the front is an important factor that determines the genetic structure of microbial colonies [113, 114]. Thus, understanding the scaling dynamics of a growing front in different cases is of importance in the wider context of understanding the evolution and growth of microbial communities.

In Chapter 3 a more detailed, mechanical simulation framework of 2D growing colonies was used to investigate the impact of the horizontal gene transfer on the genetic structure of an expanding colony. In addition to the front roughness, it has been shown that plasmid transfer by conjugation can have a profound impact on the colony manifested by reduced genetic diversity. Results show that neutral plasmid can invade the population if the conjugation rate μ is high or the expansion time is long enough. A range of nutrient concentrations c_0 was investigated and it has been shown that c_0 affects the plasmid spread in a population. Supported by other research in the field, the conclusion was that within a certain range of nutrient concentrations c_0 the roughness of the interface, which is determined by c_0, impacts the plasmid conjugation and its spread. Further simulations investigated the additional effects associated with plasmid segregative loss, showing that there exist two regimes where the number of sectors in population collapses to one. Large μ results in a population dominated by plasmid, while large segregative plasmid loss rate gives a population that lacks

the plasmid. The numerical study was further supplemented by numerical and analytical examination. Physics of annihilating random walkers on the expanding perimeter was demonstrated to successfully capture the observed patterns, at least in the case where the population initially consists of two distinct sectors. The associated diffusion equation governing the probability density of sector sizes could be analytically solved for an infinite domain. Even though the attempt of analytical solution for a finite domain did not succeed, the numerical study allowed one to make predictions about plasmid invasion rates and supported simulation results obtained in Chapter 3. It has been shown that a neutral plasmid can invade the population, however only large enough μ can result in plasmid fixation for realistic colony sizes observed in nature.

Simulation framework in Chapter 3 was further extended in Chapter 4 by implementing the more detailed plasmid conjugation algorithm. Modeling the conjugative junctions as spring-like objects acting with elastic force on conjugating cells allowed to explore the possible impact of mechanical forces on the conjugation process. Results show that σ_{max}, that is the maximum strain that the junction can sustain before it breaks, is one of the critical mechanical properties that influence the number of transconjugants. It has been shown that a larger σ_{max} gives rise to more transconjugants. However, when σ_{max} is small then the spring constant of junction k becomes important. In such a case, a larger k gives more transconjugants as it provides larger elastic force from the junction that keeps the mating pair together and prevents the junction from breaking. Moreover, results how that the junction formation rate m_{j} bottlenecks conjugation, but only when the characteristic junction formation time $1/m_{\mathrm{j}}$ is small in comparison to the plasmid transfer time t_c. Finally, the case of colliding colonies with the r702 plasmid conjugating at the collision front was investigated. It has been shown that the increasing relative motion of cells and the resulting shear acting on mating cells at the collision front affects the conjugation and reduces the number of transonjugants significantly.

Although the numerical results in Chapters 3 and 4 give qualitative and quantitative insight into the possible factors affecting plasmid conjugation, the impact of plasmid transfer on the spatial and genetic structure of the colony is still far from being understood. The computational models that have been developed for the purpose of this investigation omitted many environmental factors and were based on many assumptions. Only neutral plasmids were considered, and it has already been discussed that the metabolic cost of a plasmid is of the great

importance for its fixation or extinction. Implementing this into the existing model could shed new light on the possible impact of conjugation on segregation patterns investigated in Chapter 3 and the general conjugation performance. One could ease the restriction of one-to-one mating to allow for mating clumps as observed in the case of well-mixed colonies [192, 193]. Note that results obtained in Chapter 4 are based on a model with parameters based on certain assumptions about the nature of junctions and data available for the specific plasmid r702 that conjugated in specific conditions. To account for a more general model of conjugation some of the assumptions about the mechanical properties of junctions might need a review when new research data is present. Additionally, cell-cell interactions and the colony growth mechanics in simulations should be also extended to account for such phenomena as the 2D-to-3D transition due to inbuilt of pressure as seen in [29]. All this taken into account, such a simulation framework could be potentially used as a helpful tool to study the growth of colonies and horizontal gene transfer in many different scenarios. For example, it would be interesting to see how does the relative orientation of cells impact the conjugation process by simulating the colony growth in sets of narrow channels with different geometries.

Finally, recall that the analytical approach developed in Chapter 3 considered only a simple case for two sectors. Writing down the diffusion equation similar to Eq. 3.24, but for more than two sectors, would allow one to extend this analytical study to cases as in [113], where many sectors are present. The analytical solution of Eq. 3.24 and a similar equation for more sectors would supplement the numerical solutions such as those seen in section 3.8.1. Further incorporation of the additional factors such as plasmid segregative loss and plasmid fitness effects would make this analytical framework even more robust. With such a set of analytical tools, supplemented with simulations and aided with experiments, one should then be equipped enough for further study of biological evolution and the physics of growing microbial colonies.

Chapter 6

Appendix 1

6.1 Derivation of diffusion equation 3.24

Start with the diffusion equation for $\bar{P}(w,r)$ in linear coordinates 3.23:

$$\frac{\partial \bar{P}(w,r)}{\partial r} = D_x \frac{\partial^2 \bar{P}(w,r)}{\partial w^2} - \frac{\partial}{\partial w}\left[(\frac{w}{r} + \nu)\bar{P}(w,r)\right] \tag{6.1}$$

where the w/r convective term gives the sector growth due to colony perimeter expansion, and the ν convective term gives the sector growth due to conjugation. Define the angular sector size as:

$$\phi = \frac{w}{r} \tag{6.2}$$

which gives:

$$\frac{\partial}{\partial w} = \frac{\partial \phi}{\partial w}\frac{\partial}{\partial \phi} = \frac{1}{r}\frac{\partial}{\partial \phi} \tag{6.3}$$

Given $\bar{P}(w,r)$ in linear coordinates, this can be re-expressed as the corresponding probability distribution in angular coordinates ϕ, i.e. $\bar{P}(w,r) \equiv P(\phi,r)/r$ where the $1/r$ factor is necessary for the normalization of distribution. Substituting this

together with Eq.6.3 into Eq.6.1 and remembering that $\phi = \phi(r)$ gives:

$$\left(\frac{\partial P(\phi,r)}{\partial \phi}\frac{\partial \phi}{\partial r} + \frac{\partial P(\phi,r)}{\partial r}\right)\frac{1}{r} - \frac{P(\phi,r)}{r^2} = \frac{D_x}{r^3}\frac{\partial^2 P(\phi,r)}{\partial \phi^2} - \frac{1}{r^2}\frac{\partial}{\partial \phi}\left[\phi P(\phi,r) + \nu P(\phi,r)\right] \tag{6.4}$$

Noting $\frac{\partial \phi}{\partial r} = \frac{\partial}{\partial r}(w/r) = -w/r^2 = -\phi/r$ and further evaluating Eq. 6.4 gives:

$$-\frac{\partial P(\phi)}{\partial \phi}\frac{\phi}{r^2} + \frac{1}{r}\frac{\partial P(\phi,r)}{\partial r} - \frac{P(\phi,r)}{r^2} = \frac{D_x}{r^3}\frac{\partial^2 P(\phi,r)}{\partial \phi^2} - \frac{P(\phi,r)}{r^2} - \frac{\phi}{r^2}\frac{\partial P(\phi,r)}{\partial \phi} - \frac{\nu}{r^2}\frac{\partial P(\phi,r)}{\partial \phi} \tag{6.5}$$

Some of the terms cancel and after rearrangement one gets Eq. 3.24

$$\frac{\partial P(\phi,r)}{\partial r} = \frac{D_x}{r^2}\frac{\partial^2 P(\phi,r)}{\partial \phi^2} - \frac{\nu}{r}\frac{\partial P(\phi,r)}{\partial \phi} \tag{6.6}$$

Chapter 7

Appendix 2

7.1 Solution for the infinite domain

The equation

$$\frac{\partial P(\phi,r)}{\partial r} = \frac{D_x}{r^2}\frac{\partial^2 P(\phi,r)}{\partial \phi^2} - \frac{\nu}{r}\frac{\partial P(\phi,r)}{\partial \phi} \tag{7.1}$$

can be solved analytically on the infinite domain, subject to boundary conditions $P(-\infty,r) = P(\infty,r) = 0$ and the initial condition $P(\phi,r_0) = \delta(\phi-\phi_0)$. Define the Fourier transform

$$\tilde{P}(k,r) = \int_{-\infty}^{\infty} P(\phi,r)e^{-ik\phi}d\phi \tag{7.2}$$

The initial condition becomes

$$\tilde{P}(k,r_0) = \int_{-\infty}^{\infty} \delta(\phi-\phi_0)e^{-ik\phi}d\phi = -e^{ik\phi_0} \tag{7.3}$$

Applying the transform to each side of Eq.(7.1) gives:

$$\frac{\partial \tilde{P}(k,r)}{\partial r} = -\frac{D_x}{r^2}k^2\tilde{P}(k,r) - i\frac{\nu}{r}k\tilde{P}(k,r) \tag{7.4}$$

Rearranging the Eq.(7.4) and integrating both sides gives:

$$\ln \tilde{P}(k,r) = \frac{D_x k^2}{r} - i\nu k \ln(r) + C \tag{7.5}$$

where C is the integration constant. It can be evaluated from the initial condition Eq.(7.3) that :

$$-ik\phi_0 = \frac{D_x k^2}{r_0} - i\nu k \ln(r_0) + C \tag{7.6}$$

and so C is:

$$C = -\frac{D_x k^2}{r_0} + i\nu k \ln(r_0) + ik\phi_0 \tag{7.7}$$

Substituting it back into Eq.(7.5) gives:

$$\begin{aligned} \ln \tilde{P}(k,r) = \frac{D_x k^2}{r} - i\nu k \ln(r) - \frac{D_x k^2}{r_0} + i\nu k \ln(r_0) + ik\phi_0 = \\ = D_x k^2 \left[\frac{1}{r} - \frac{1}{r_0}\right] - i\nu k[\ln(r) - \ln(r_0)] + ik\phi_0 \end{aligned} \tag{7.8}$$

Taking the exponent of both sides gives the expression for $\tilde{P}(k,t)$:

$$\tilde{P}(k,r) = \exp\left[D_x k^2 \left[\frac{1}{r} - \frac{1}{r_0}\right] - i\nu k[\ln(r) - \ln(r_0)] + ik\phi_0\right] \tag{7.9}$$

Now apply the inverse Fourier transform to Eq.(7.9) to retrieve the expression for $P(\phi, r)$:

$$\begin{aligned} P(\phi,r) = \frac{1}{2\pi}\int_{-\infty}^{\infty} \tilde{P}(k,r) e^{ik\phi} dk = \\ = \frac{1}{2\pi}\int_{-\infty}^{\infty} \exp\left[D_x k^2 A - i\nu k[\ln(r) - \ln(r_0)] + ik\phi_0 + ik\phi\right] dk \end{aligned} \tag{7.10}$$

where $A = \left[\frac{1}{r} - \frac{1}{r_0}\right]$. Setting $B = i(\nu \ln(r) - \nu \ln(r_0) - \phi - \phi_0)$ reduces the above

expression to:

$$P(\phi, r) = \frac{1}{2\pi} \int_{-\infty}^{\infty} \exp\left[D_x k^2 A - kB\right] dk \tag{7.11}$$

which is the integral of the Gaussian function with the solution:

$$P(\phi, r) = \frac{1}{2\pi} \sqrt{\frac{\pi}{AD_x}} \frac{B^2}{4AD_x} \tag{7.12}$$

which after substituting for A and B gives the final expression for $P(\phi, r)$ on the infinite domain:

$$P(\phi, r) = \left(4\pi \left(\frac{1}{r_0} - \frac{1}{r}\right)\right)^{-1/2} \exp\left(\frac{-(\nu \ln(r) - \nu \ln(r_0) - \phi - \phi_0)^2}{4D_x \left(\frac{1}{r_0} - \frac{1}{r}\right)}\right) \tag{7.13}$$

Bibliography

[1] J. Bada and A. Lazcano, *The Origin of Life*. Cambridge, MA: Belknap Press of Harvard University Press., 2009.

[2] L. Parfrey, "Evaluating support for the current classification of eukaryotic diversity," *PSOL Genetics*, vol. 2, pp. 220–238, 2006.

[3] N. Pace, "Time for a change," *Nature*, vol. 441, no. 7091, p. 289, 2006.

[4] B. J. Tindall, "Notes on the characterization of prokaryote strains for taxonomic purposes.," *International Journal of Systematic and Evolutionary Microbiology*, vol. 60, no. 1, pp. 249–266, 2010.

[5] T. Curtis, W. Sloan, and J. Scannell, "Estimating prokaryotic diversity and its limits," *Proceedings of the National Academy of Sciences*, vol. 99, no. 16, pp. 10494–10499, 2002.

[6] P. Schloss and J. Handelsman, "Status of the microbial census," *Microbiology and Molecular Biology Reviews*, vol. 68, no. 4, pp. 686–691, 2004.

[7] A. Chapman, *Numbers of living species in Australia and the World*. Canberra: Australian Biological Resources Study, 2006.

[8] V. D'Costa, "Antibiotic resistance is ancient," *Nature*, vol. 477, no. 7365, pp. 457–461, 2011.

[9] H. Goossens, M. Ferech, S. R. Vander, and M. Elseviers, "Outpatient antibiotic use in europe and association with resistance: a cross-national database study," *Lancet*, vol. 365, no. 9459, pp. 579–587, 2005.

[10] E. Grice, "Topographical and temporal diversity of the human skin microbiome," *Science*, vol. 324, no. 5931, pp. 1190–1192, 2009.

[11] R. Sender, S. Fuchs, and R. Milo, "Revised estimates for the number of human and bacteria cells in the body," *bioRxiv*, 2016.

[12] W. Wikoff, A. Anfora, J. Liu, P. Schultz, S. Lesley, and E. Peters, "Metabolomics analysis reveals large effects of gut microflora on mammalian blood metabolites," *Proceedings of the National Academy of Sciences*, vol. 106, no. 10, pp. 3698–3703, 2009.

[13] F. Guarner and J. Malagelada, "Gut flora in health and disease," *Lancet*, vol. 361, no. 9356, pp. 512–519, 2003.

[14] E. Hsiao, S. McBride, S. Hsien, G. Sharon, E. Hyde, and T. McCue, "The microbiota modulates gut physiology and behavioral abnormalities associated with autism," *Cell*, vol. 155, no. 7, pp. 1451–1463, 2013.

[15] A. Wolfe and H. Berg, "Migration of bacteria in semisolid agar.," *Proceedings of the National Academy of Sciences*, vol. 86, no. 18, pp. 6973–6977, 1989.

[16] B. Miroux and J. Walker, "Over-production of proteins in escherichia coli: mutant hosts that allow synthesis of some membrane proteins and globular proteins at high levels.," *Journal of molecular biology*, vol. 260, no. 3, pp. 289–298, 1996.

[17] Z. Royce, J. Dong, and B. Schmittmann, "Modelling translation in protein synthesis with tasep: A tutorial and recent developments.," *Journal of Statistical Physics*, vol. 144, no. 2, pp. 405–428, 2011.

[18] J. Vilar and L. Saiz, "Systems biophysics of gene expression.," *Biophysical journal*, vol. 104, no. 12, pp. 2574–2585, 2013.

[19] S. Scheuring and Y. Dufrne, "Atomic force microscopy: probing the spatial organization, interactions and elasticity of microbial cell envelopes at molecular resolution.," *Molecular microbiology*, vol. 75, no. 6, pp. 1327–1336, 2010.

[20] D. Volfson, S. Cookson, J. Hasty, and L. Tsimring, "Biomechanical ordering of dense cell populations," *Proceedings of the National Academy of Sciences*, vol. 105, no. 40, pp. 15346–15351, 2008.

[21] Nahemlabs Website, "Automatic segmentation of microscopy images," 2016. [Online; accessed 23 February, 2016].

[22] CDEWorlds Website, "Microbes, inflammation, scaling and root planing, and the periodontal condition," 2016. [Online; accessed 11 February, 2016].

[23] R. Macnab and D. Koshland, "The gradient-sensing mechanism in bacterial chemotaxis," *Proceedings of the National Academy of Sciences*, vol. 69, no. 9, pp. 2509–2512, 1972.

[24] J. Sachs, "The evolution of cooperation," *The Quarterly Review of Biology*, vol. 79, no. 2, pp. 135–160, 2004.

[25] P. Andersen, B. Brodbeck, S. Oden, A. Shriner, and B. Leite, "Medical biofilms," *Biotechnology and bioengineering*, vol. 100, no. 1, pp. 1–18, 2008.

[26] P. Marsh and D. Bradshaw, "Dental plaque as a biofilm," *Journal of Industrial Microbiology*, vol. 15, no. 3, p. 169, 1995.

[27] P. Andersen, "Influence of xylem fluid chemistry on planktonic growth, biofilm formation and aggregation of xylella fastidiosa," *FEMS Microbiology Letters*, vol. 274, no. 2, pp. 210–217, 2007.

[28] L. Hall-Stoodley, J. Costerton, and P. Stoodley, "Bacterial biofilms: from the natural environment to infectious diseases," *Nature Reviews Microbiology*, vol. 2, no. 2, p. 95?108, 2004.

[29] M. Grant, B. Waclaw, R. Allen, and P. Cicuta, "The role of mechanical forces in the planar-to-bulk transition in growing escherichia coli microcolonies," *Journal of The Royal Society Interface*, vol. 11, no. 97, p. 20140400, 2014.

[30] A. Griffin, S. West, and A. Buckling, "Cooperation and competition in pathogenic bacteria," *Nature*, vol. 430, no. 7003, pp. 1024–1027, 2004.

[31] E. Zinser and R. Kolter, "Escherichia coli evolution during stationary phase," *Res. Microbiol*, vol. 155, no. 5, pp. 328–336, 2004.

[32] C. Beloin and J. Ghigo, "Finding gene-expression patterns in bacterial biofilms," *Trends in Microbiology*, vol. 13, no. 1, pp. 16–19, 2005.

[33] S. K. Lewis, A. Camper, G. Ehrlich, J. Costerton, and D. Davies, "Pseudomonas aeruginosa displays multiple phenotypes during development as a biofilm," *Journal of Bacteriology*, vol. 184, no. 4, pp. 1140–1154, 2002.

[34] M. Miller and B. Bassler, "Quorum sensing in bacteria," *Annu. Rev. Microbiol.*, vol. 55, no. 1, pp. 165–199, 2001.

[35] D. Senadheera and D. G. Cvitkovitch, "Quorum sensing and biofilm formation by streptococcus mutans," *Advances in Experimental Medicine and Biology*, vol. 631, pp. 178–88, 2008.

[36] C. OLoughlin, "A quorum-sensing inhibitor blocks pseudomonas aeruginosa virulence and biofilm formation," *Proceedings of the National Academy of Sciences*, vol. 110, no. 44, pp. 17981–17986, 2013.

[37] O. Rendueles and J. Ghigo, "Mechanisms of competition in biofilm communities," *Microbiology Spectrum*, vol. 3, no. 3, 2015.

[38] G. Sezonov, D. Joseleau-Petit, and R. D'Ari, "Escherichia coli physiology in luria-bertani broth," *J. Bacteriol*, vol. 189, no. 23, pp. 8746–8749, 2007.

[39] H. Lee, E. Popodi, H. Tang, and P. Foster, "Rate and molecular spectrum of spontaneous mutations in the bacterium escherichia coli as determined by whole-genome sequencing," *Proceedings of the National Academy of Sciences*, vol. 109, no. 41, pp. 2774–2783, 2012.

[40] J. Lawrence, "Horizontal and vertical gene transfer: the life history of pathogens," *Concepts in Bacterial Virulence*, vol. 12, pp. 255–271, 2005.

[41] J. Kleinschmidt, B. Soeding, M. Teuber, and H. Neve, "Evaluation of horizontal and vertical gene transfer and stability of heterologous dna in streptococcus thermophilus isolated from yogurt and yogurt starter cultures," *Systematic and applied microbiology*, vol. 16, no. 2, pp. 287–295, 1993.

[42] I. Letunic and P. Bork, "Interactive tree of life (itol): an online tool for phylogenetic tree display and annotation," *Bioinformatics*, vol. 23, no. 1, pp. 127–128, 2007.

[43] +Plus magazine, "Reconstructing tree of life," 2016. [Online; accessed 12 February, 2016].

[44] S. Soucy, J. Huang, and J. Gogarten, "Horizontal gene transfer: building the web of life," *Nat Rev Genet*, vol. 16, no. 8, pp. 472–482, 2015.

[45] M. Syvanen, "Evolutionary implications of horizontal gene transfer," *Annual Review of Genetics*, vol. 46, pp. 341–358, 2012.

[46] C. Gyles and P. Boerlin, "Horizontally transferred genetic elements and their role in pathogenesis of bacterial disease," *Veterinary Pathology*, vol. 51, no. 2, pp. 328–340, 2014.

[47] K. Wommack and R. Colwell, "Virioplankton: Viruses in aquatic ecosystems," *Microbiology and Molecular Biology Reviews*, vol. 64, no. 1, pp. 69–114, 2000.

[48] S. Phornphisutthimas, A. Thamchaipenet, and B. Panijpan, "Conjugation in escherichia coli," *Biochemistry and molecular biology education*, vol. 35, no. 6, pp. 440–445, 2007.

[49] Glover Lab, "Regulation of bacterial conjugation," 2016. [Online; accessed 12 February, 2016].

[50] http://parts.igem.org/Conjugation, "Registry of standard biological parts: conjugation.," 2016. [Online; accessed 20 May, 2016].

[51] J. Lederberg and E. Tatum, "Gene recombination in e. coli," *Nature*, vol. 158, no. 4016, p. 558, 1946.

[52] K. Ryan and C. Ray, "Sherris medical microbiology (4th ed.)," *McGraw Hill*, pp. 60–64, 2004.

[53] J. Yang and Y. Yang, "Plasmid size can affect the ability of escherichia coli to produce high-quality plasmids," *Biotechnol Lett.*, vol. 34, no. 11, pp. 2017–2022, 2012.

[54] J. Heinemann and G. Sprague Jr, "Bacterial conjugative plasmids mobilize dna transfer between bacteria and yeast," *Nature*, vol. 340, no. 6230, pp. 205–209, 1989.

[55] S. Projan, S. Carleton, and R. Novick, "Determination of plasmid copy number by fluorescence densitometry," *Plasmid*, vol. 9, no. 2, pp. 182–190, 1983.

[56] J. Lederberg, "Cell genetics and hereditary symbiosis," *Physiol. Rev*, vol. 32, no. 4, pp. 403–430, 1952.

[57] C. Thomas, "Horizontal gene pool: bacterial plasmids and gene spread," *CRC Press*, 2003.

[58] F. Rafii and D. Crawford, "Transfer of conjugative plasmids and mobilization of a nonconjugative plasmid between streptomyces strains on agar and in soil," *Appl Environ Microbiol*, vol. 54, no. 6, pp. 1334–1340, 1988.

[59] S. Maeda, "Horizontal transfer of nonconjugative plasmids in a colony biofilm of escherichia coli," *FEMS Microbiol Lett*, vol. 255, no. 1, pp. 115–120, 2006.

[60] R. Novick, "Plasmid incompatibility," *Microbiol Rev.*, vol. 51, no. 4, pp. 381–395, 1987.

[61] N. Velappan, "Plasmid incompatibility: more compatible than previously thought?," *Protein Engineering, Design and Selection*, vol. 20, no. 7, pp. 309–313, 2007.

[62] K. Nordstrom and S. Austin, "Mechanisms that contribute to the stable segregation of plasmids," *Annual Review of Genetics*, vol. 23, no. 1, pp. 37–69, 1989.

[63] M. Achtman, N. Kennedy, and R. Skurray, "Cell-cell interactions in conjugating escherichia coli: role of trat protein in surface exclusion.," *Proceedings of the National Academy of Sciences*, vol. 74, no. 11, pp. 5104–5108, 1977.

[64] A. Carattoli, "Resistance plasmid families in enterobacteriaceae," *Antimicrobial agents and chemotherapy*, vol. 53, no. 6, pp. 2227–2238, 2009.

[65] A. Stolz, "Degradative plasmids from sphingomonads," *FEMS Microbiol Lett.*, vol. 350, no. 1, pp. 9–19, 2014.

[66] T. Basta, A. Kecl, J. Klein, and A. Stolz, "Detection and characterization of conjugative degradative plasmids in xenobiotic-degrading sphingomonas strains," *J Bacteriol.*, vol. 186, no. 12, pp. 3862–3872, 2004.

[67] H. Milch, S. Nikolnikov, and E. Czirk, "Escherichia coli col v plasmids and their role in pathogenicity," *Acta Microbiol Hung.*, vol. 31, no. 2, pp. 117–125, 1984.

[68] M. Riley and D. Gordon, "A survey of col plasmids in natural isolates of escherichia coli and an investigation into the stability of col-plasmid lineages," *Journal of general microbiolog*, vol. 138, no. 7, pp. 1345–1352, 1992.

[69] T. Johnson and L. Nolan, "Pathogenomics of the virulence plasmids of escherichia coli," *Microbiol Mol Biol Rev.*, vol. 73, no. 4, pp. 750–774, 2009.

[70] K. E. IppenIhler and E. Minkley Jr, "The conjugation system of f, the fertility factor of escherichia col," *Annual review of genetics*, vol. 20, no. 1, pp. 593–624, 1986.

[71] T. Dimitriua, D. Misevica, A. Lindnera, and F. Taddeia, "Mobile genetic elements are involved in bacterial sociality," *Mobile Genetic Elements*, vol. 5, no. 1, 2015.

[72] J. Ghigo, "Natural conjugative plasmids induce bacterial biofilm development," *Nature*, vol. 412, no. 6845, pp. 442–44, 2001.

[73] S. Draw and R. Bonomo, "Three decades of ?-lactamase inhibitors," *Clinical Microbiology Reviews*, vol. 23, no. 1, pp. 160–201, 2010.

[74] A. Carattoli, "Plasmid-mediated antimicrobial resistance in salmonella enterica," *Curr Issues Mol Biol*, vol. 5, no. 4, pp. 113–122, 2003.

[75] A. Adjiri-Awere and T. Van Lunen, "Subtherapeutic use of antibiotics in pork production: Risks and alternative," *Canadian Journal of Animal Science*, vol. 85, no. 2, pp. 117–130, 2005.

[76] C. Cogliani, H. Goossens, and C. Greko, "Restricting antimicrobial use in food animals: Lessons from europe," *Microbe Magazine*, vol. 6, no. 6, p. 274, 2011.

[77] J. C. Pechere, "Patients' interviews and misuse of antibiotics," *Clinical Infectious Diseases*, vol. 33, no. 3, pp. S170–S173, 2001.

[78] R. Weinstein, "Controlling antimicrobial resistance in hospitals: infection control and use of antibiotics," *Emerging infectious diseases*, vol. 7, no. 2, p. 188, 2001.

[79] K. Kumarasamy, M. Toleman, and T. e. a. Walsh, "Emergence of a new antibiotic resistance mechanism in india, pakistan, and the uk: a molecular, biological, and epidemiological study," *Lancet Infect Dis*, vol. 10, no. 9, pp. 597–602, 2010.

[80] A. Queenan and K. Bush, "Carbapenemases: the versatile beta-lactamases," *Clinical Microbiology Reviews*, vol. 20, no. 3, pp. 440–458, 2007.

[81] Y. Liu, "Emergence of plasmid-mediated colistin resistance mechanism mcr-1 in animals and human beings in china: a microbiological and molecular biological study," *The Lancet Infectious Diseases*, vol. 16, no. 1, 2015.

[82] H. Hasman, A. Hammerum, F. Hansen, S. Hendriksen, B. Olesen, Y. Agerso, and E. Zankari, "Detection of mcr-1 encoding plasmid-mediated colistin-resistant escherichia coli isolates from human bloodstream infection and imported chicken meat, denmark 2015," *Eurosurveillances*, vol. 20, no. 49, pp. 1–5, 2015.

[83] L. Jian, C. Rayner, T. Nation, R. Deans, R. Boots, N. Widdecombe, A. Douglas, and J. Lipman, "Pharmacokinetics of colistin methanesulfonate and colistin in a critically ill patient receiving continuous venovenous hemodiafiltration," *Antimicrobial agents and chemotherapy*, vol. 49, no. 11, pp. 4814–4815, 2005.

[84] P. Zambryski, H. Joos, C. Genetello, J. Leemans, M. Van Montagu, and J. Schell, "Ti plasmid vector for the introduction of dna into plant cells without alteration of their normal regeneration capacity," *The EMBO journal*, vol. 2, no. 12, p. 2143, 1983.

[85] R. Walden and J. Schell, "Techniques in plant molecular biology–progress and problems," *European Journal of Biochemistry*, vol. 192, no. 3, pp. 563–76, 1990.

[86] A. Fischer, S. Hacein-Bey-Abina, and M. Cavazzana-Calvo, "20 years of gene therapy for scid," *Nature Immunology*, vol. 11, no. 6, pp. 457–460, 2010.

[87] S. Wolfram, "Statistical mechanics of cellular automata," *Reviews of Modern Physics*, vol. 55, no. 3, pp. 601–644, 1983.

[88] E. Ben-Jacob, . Schochet, A. Tenenbaum, I. Cohen, A. Czirok, and T. Vicsek, "Generic modeling of cooperative growth-patterns in bacterial colonies," *Nature*, vol. 368, pp. 46–49, 1994.

[89] D. Arkendra and R. Durrett, "Stepping-stone spatial structure causes slow decay of linkage disequilibrium and shifts the site frequency spectrum," *Genetics*, vol. 176, no. 2, pp. 969–981, 2007.

[90] M. Crimson and G. Barker, "Continuum model for the spatiotemporal growth of bacterial colonies," *Phys Rev E*, vol. 44, pp. 1680–1684, 1994.

[91] E. Alpkvist, N. Overgaard, S. Gustafsson, and A. Heyden, "A new mathematical model for chemotactic bacterial colony growth," *Water Science and Technology*, vol. 49, no. 11-12, pp. 187–192, 2004.

[92] T. Vicsek, A. Czirok, E. Ben-Jacob, I. Cohen, and O. Shochet, "Novel type of phase transition in a system of self-driven particles," *Physical Review Letters*, vol. 75, no. 6, pp. 1226–1229, 1995.

[93] J. Kreft, G. Booth, and J. Wimpenny, "Bacsim, a simulator for individual-based modelling of bacterial colony growth," *Microbiology*, vol. 144, no. 12, pp. 3275–3287, 1998.

[94] J. Kreft, C. Picioreanu, J. Wimpenny, and M. van Loosdrecht, "Individual-based modelling of biofilms," *Microbiology*, vol. 147, no. 11, pp. 2897–2912, 2001.

[95] L. Lardon, B. Merkey, S. Martins, A. Dotsch, C. Picioreanu, J. Kreft, and B. Smets, "idynomics: next-generation individual-based modelling of biofilms," *Environmental Microbiology*, vol. 13, no. 9, pp. 2416–2434, 2011.

[96] J. Shapiro and C. Hsu, "Escherichia coli k-12 cell-cell interactions seen by time-lapse video.," *Journal of bacteriology*, vol. 171, no. 11, p. 5963, 1989.

[97] Wikipedia, the free encyclopedia, "Bacterial cellular morphologies," 2016. [Online; accessed 26 February, 2016].

[98] K. Young, "The selective value of bacterial shape," *Microbiology and Molecular Biology Reviews*, vol. 70, no. 3, pp. 660–703, 2006.

[99] D. Hay, N.and Tipper, D. Gygi, and C. Hughes, "A novel membrane protein influencing cell shape and multicellular swarming of proteus mirabilis," *Journal of bacteriology*, vol. 181, no. 7, pp. 2008–2016, 1999.

[100] P. Danese, L. Pratt, S. Dove, and R. Kolter, "The outer membrane protein, antigen 43, mediates cell-to-cell interactions within escherichia coli biofilms," *Molecular microbiology*, vol. 37, no. 2, pp. 424–432, 2000.

[101] C. Gallant, C. Daniels, J. Leung, A. Ghosh, K. Young, L. Kotra, and L. Burrows, "Common b-lactamases inhibit bacterial biofilm formation," *Molecular microbiology*, vol. 58, no. 4, pp. 1012–1024, 2005.

[102] F. Farrell, O. Hallatschek, D. Marenduzzo, and B. Waclaw, "Mechanically driven growth of quasi-two-dimensional microbial colonies," *Physical Review Letters*, vol. 111, no. 16, p. 168101, 2013.

[103] D. Lauffenburger, R. Aris, and K. Keller, "Effects of cell motility and chemotaxis on microbial population growth," *Biophysics Journal*, vol. 40, no. 3, pp. 209–219, 1982.

[104] T. Garrett, M. Bhakoo, and Z. Zhang, "Bacterial adhesion and biofilms on surfaces," *Progress in Natural Science*, vol. 18, no. 9, pp. 209–219, 2008.

[105] L. Onsager, "The effects of shape on the interaction of colloidal particles," *Annals of the New York Academy of Sciences*, vol. 51, no. 4, pp. 627–659, 1949.

[106] D. Frenkel, "Entropy-driven phase transitions," *Physica A: statistical mechanics and its applications*, vol. 263, no. 1, pp. 26–38, 1999.

[107] D. Boyer, W. Mather, O. Mondragon-Palomino, S. Orozco-Fuentes, T. Danino, J. Hasty, and L. S. Tsimring, "Buckling instability in ordered bacterial colonies," *Physical Biology*, vol. 8, no. 2, p. 026008, 2011.

[108] H. Cho, "Self-organization in high-density bacterial colonies: efficient crowd control," *PLoS biology*, vol. 5, no. 11, p. e302, 2007.

[109] J. Hernandez-Ortiz, C. Stoltz, and M. Graham, "Transport and collective dynamics in suspensions of confined swimming particles," *Physical review letters*, vol. 95, no. 20, p. 204501, 2005.

[110] X. Wu and A. Libchaber, "Particle diffusion in a quasi-two-dimensional bacterial bath," *Physical Review Letters*, vol. 84, no. 13, pp. 3017–3020, 2000.

[111] N. Mendelson, A. Bourque, K. Wilkening, K. Anderson, and J. Watkins, "Organized cell swimming motions in bacillus subtilis colonies: patterns of short-lived whirls and jets," *Journal of bacteriology*, vol. 181, no. 2, pp. 600–609, 1999.

[112] C. Dombrowski, L. Cisneros, S. Chatkaew, R. Goldstein, and J. Kessler, "Self-concentration and large-scale coherence in bacterial dynamics," *Physical review letters*, vol. 93, no. 9, p. 098103, 2004.

[113] O. Hallatschek, P. Hersen, S. Ramanathan, and D. Nelson, "Genetic drift at expanding frontiers promotes gene segregation," *Proceedings of the National Academy of Sciences*, vol. 104, no. 50, pp. 19926–19930, 2007.

[114] O. Hallatschek and D. Nelson, "Life at the front of an expanding population," *Evolution*, vol. 64, no. 1, pp. 193–206, 2010.

[115] M. Eden, "A two-dimensional growth process," *Proceedings of the Fourth Berkeley Symposium on Mathematical Statistics and Probability, Vol 4: Contributions to Biology and Problems of Medicine*, vol. 4, pp. 223–239, 1961.

[116] M. Plischke and Z. Racz, "Dynamic scaling and the surface structure of eden clusters," *Phys. Rev. A*, vol. 32 (6), pp. 3825–3828, 1985.

[117] F. Aarao, "Depinning transitions in interface growth models.," *Braz. J. Phys.*, vol. 33, no. 3, pp. 501–513, 2003.

[118] M. Kardar, G. Parisi, and Y. Zhang, "Dynamic scaling of growing interfaces," *Phys. Rev. Lett.*, vol. 56, no. 9, pp. 889–892, 1986.

[119] M. Beccaria and G. Curci, "Numerical simulation of the kardar-parisi-zhang equation," *Phys. Rev. E*, vol. 50 (6), pp. 4560–4563, 1994.

[120] F. Family and T. Vicsek, "Scaling of the active zone in the eden process on percolation networks and the ballistic deposition model," *Journal of Physics A: Mathematical and General*, vol. 18 (2), p. L75, 1985.

[121] P. Meakin, P. Ramanlal, L. Sander, and R. Ball, "Ballistic deposition on surfaces," *Phys. Rev. A*, vol. 34 (6), pp. 5091–5103, 1986.

[122] H. Guo, B. Grossmann, and M. Grant, "Kinetics of interface growth in driven systems," *Phys. Rev. Lett.*, vol. 64 (11), pp. 1262–1265, 1990.

[123] K. Takeuchi, "Statistics of circular interface fluctuations in an off-lattice eden model," *Journal of Statistical Mechanics: Theory and Experiment*, vol. 2012 (05), p. P05007, 2012.

[124] S. Alves, T. Oliveira, and S. Ferreira, "Universal fluctuations in radial growth models belonging to the kpz universality class," *Europhysics Letters*, vol. 96 (4), no. 4, p. 48003, 2011.

[125] D. Wolf and J. Kertesz, "Surface width exponents for three- and four-dimensional eden growth," *Europhysics Letters*, vol. 4 (6), p. 651, 1987.

[126] T. Halpin-Healy, "Diverse manifolds in random media," *Physical Review Letters*, vol. 62 (4), pp. 442–445, 1989.

[127] J. Kim and J. Kosterlitz, "Growth in a restricted solid-on-solid model," *Physical Review Letters*, vol. 62 (19), pp. 2289–2292, 1989.

[128] P. Devillard and H. Stanley, "Scaling properties of eden clusters in three and four dimensions," *Physica A: Statistical Mechanics and its Applications*, vol. 160 (3), pp. 298–309, 1989.

[129] J. Maunuksela, "Kinetic roughening in slow combustion of paper.," *Physical review letters*, vol. 79, no. 8, p. 1515, 1997.

[130] A. Borodin, "Fluctuation properties of the tasep with periodic initial configuration.," *Journal of Statistical Physics*, vol. 129, no. 5-6, pp. 1055–1080, 2007.

[131] P. Su, P. Yen, S. Wang, C. Lin, A. Chiou, and W. Syu, "Factors affecting daughter cells' arrangement during the early bacterial divisions," *PloS one*, vol. 5, no. 2, p. e9147, 2010.

[132] H. Varian, "Bootstrap tutorial.," *Mathematica Journal*, vol. 9, no. 4, pp. 768–775, 2005.

[133] A. Reis, "Universality in two-dimensional kardar-parisi-zhang growth.," *Physical Review E*, vol. 69, no. 2, p. 021610, 2004.

[134] J. Kelling and O. Geza, "Extremely large-scale simulation of a kardar-parisi-zhang model using graphics cards.," *Physical Review E*, vol. 84, no. 6, p. 061150, 2011.

[135] M. Gralka, F. Stiewe, F. Farrell, W. Moebius, B. Waclaw, and O. Hallatschek, "Allele surfing promotes microbial adaptation from standing variation," *bioRxiv*, 2016.

[136] J. Masel, "Genetic drift," *Current Biology*, vol. 21, no. 20, p. R837?R838, 2011.

[137] K. Korolev, M. Avlund, O. Hallatschek, and D. Nelson, "Genetic demixing and evolution in linear stepping stone models," *Reviews of modern physics*, vol. 82, no. 2, p. 1691, 2010.

[138] M. Kimura and G. Weiss, "The stepping stone model of population structure and the decrease of genetic correlation with distance," *Genetics*, vol. 49, no. 4, p. 561, 1964.

[139] A. J. Lotka, *Elements of physical biology*. Williams and Wilkins Baltimore, 1925.

[140] H. Fujikawa, "Diversity of the growth patterns of bacillus subtilis colonies on agar plates," *FEMS microbiology ecology*, vol. 13, no. 3, pp. 159–167, 1994.

[141] B. Levin, F. Stewart, and V. Rice, "The kinetics of conjugative plasmid transmission: fit of a simple mass action model," *Plasmid*, vol. 2, no. 2, pp. 247–260, 1979.

[142] B. Levin and F. Stewart, "The population biology of bacterial plasmids: a priori conditions for the existence of mobilizable nonconjugative factors," *Genetics*, vol. 94, no. 2, pp. 425–443, 1980.

[143] L. Simonsen, D. Gordon, F. Stewart, and B. Levin, "Estimating the rate of plasmid transfer: an end-point method," *Journal of general microbiology*, vol. 136, no. 11, pp. 2319–2325, 1990.

[144] J. Monod, "The growth of bacterial cultures," *Annual Review of Microbiology*, vol. 3, p. 371, 1949.

[145] K. Duncan, N. Ferguson, and C. Istock, "Fitnesses of a conjugative plasmid and its host bacteria in soil microcosms," *Molecular biology and evolution*, vol. 12, no. 6, pp. 1012–1021, 1995.

[146] B. Normander, B. Christensen, S. Molin, and N. Kroer, "Effect of bacterial distribution and activity on conjugal gene transfer on the phylloplane of the bush bean (phaseolus vulgaris)," *Applied and environmental microbiology*, vol. 64, no. 5, pp. 1902–1909, 1998.

[147] A. Lilley and M. Bailey, "The transfer dynamics of pseudomonas sp. plasmid pqbr11 in biofilms," *FEMS microbiology ecology*, vol. 42, no. 2, pp. 243–250, 2002.

[148] T. Licht, B. Christensen, K. Krogfelt, and S. Molin, "Plasmid transfer in the animal intestine and other dynamic bacterial populations: the role of community structure and environment," *Microbiology*, vol. 145, no. 9, pp. 2615–2622, 1999.

[149] R. Fox, X. Zhong, S. Krone, and E. Top, "Spatial structure and nutrients promote invasion of incp-1 plasmids in bacterial populations," *The ISME journal*, vol. 2, no. 10, pp. 1024–1039, 2008.

[150] J. Haagensen, S. Hansen, T. Johansen, and S. Molin, "In situ detection of horizontal transfer of mobile genetic elements," *FEMS microbiology ecology*, vol. 42, no. 2, pp. 261–268, 2002.

[151] R. Freter, R. Freter, and H. Brickner, "Experimental and mathematical models of escherichia coli plasmid transfer in vitro and in vivo," *Infection and immunity*, vol. 39, no. 1, pp. 60–84, 1983.

[152] P. Freese, K. Korolev, J. Jimenez, and C. I., "Genetic drift suppresses bacterial conjugation in spatially structured populations," *Biophysical Journal*, vol. 106, no. 4, pp. 944–954, 2014.

[153] S. Guttenplan and D. Kearns, "Regulation of flagellar motility during biofilm formation.," *FEMS microbiology reviews*, vol. 37, no. 6, pp. 849–871, 2013.

[154] K. Johnson, K. Kendall, and A. Roberts, "Surface energy and the contact of elastic solids.," *Proceedings of the Royal Society of London A: Mathematical, Physical and Engineering Sciences*, vol. 324, no. 1558, 1971.

[155] K. Atkinson, *An Introduction to Numerical Analysis (2nd ed.)*. New York: John Wiley and Sons, 1989.

[156] P. Olver, *Introduction to Partial Differential Equations*. Springer Science and Business Media, 2013.

[157] R. Milo, P. Jorgensen, U. Moran, G. Weber, and M. Springer, "Bionumbers?the database of key numbers in molecular and cell biology," *Nucleic Acids Research*, vol. 38, pp. D750–D753, 2010.

[158] H. Tuson, "Measuring the stiffness of bacterial cells from growth rates in hydrogels of tunable elasticity.," *Molecular Microbiology*, vol. 84, no. 5, p. 874?891, 2012.

[159] L. Mignot and G. Guy-Alain Junter, "Diffusion in immobilized-cell agar layers: influence of microbial burden and cell morphology on the diffusion coefficients ofl-malic acid and glucose.," *Applied and environmental microbiology*, vol. 32, no. 4, pp. 418–423, 1990.

[160] A. Varma, B. Boesch, and B. Palsson, "Stoichiometric interpretation of escherichia coli glucose catabolism under various oxygenation rates.," *Applied and environmental microbiology*, vol. 59, no. 8, pp. 2465–2473, 1993.

[161] I. del Campo, "Determination of conjugation rates on solid surfaces.," *Plasmi*, vol. 67, no. 2, pp. 174 – 182, 2012.

[162] R. Lenski and J. Bouma, "Effects of segregation and selection on instability of plasmid pacyc184 in escherichia coli b.," *Journal of bacteriolog*, vol. 169, no. 11, pp. 5314–5316, 1987.

[163] S. Million-Weaver and M. Camps, "Mechanisms of plasmid segregation: have multicopy plasmids been overlooked?.," *Plasmid*, vol. 75, pp. 27–35, 2014.

[164] J. Ponciano, "The population biology of bacterial plasmids: a hidden markov model approach.," *Genetics*, vol. 176, no. 2, pp. 957–968, 2007.

[165] L. De Gelder, "Stability of a promiscuous plasmid in different hosts: no guarantee for a long-term relationship.," *Microbiology*, vol. 153, no. 2, pp. 452–463, 2007.

[166] D. Toussaint and F. Wilczek, "Particle–antiparticle annihilation in diffusive motion," *The Journal of Chemical Physics*, vol. 78, p. 2642, 1983.

[167] S. Krone, R. Lu, R. Fox, H. Suzuki, and E. Top, "Modelling the spatial dynamics of plasmid transfer and persistence," *Microbiology*, vol. 153, no. 8, pp. 2803–2816, 2007.

[168] L. De Gelder, J. Ponciano, P. Joyce, and E. Top, "Stability of a promiscuous plasmid in different hosts: no guarantee for a long-term relationship," *Microbiology*, vol. 153, no. 2, pp. 452–463, 2007.

[169] J. Cullum, J. Collins, and P. Broda, "Factors affecting the kinetics of progeny formation with f -lac in escherichia coli k12," *Plasmid*, vol. 1, no. 4, pp. 536–544, 1978.

[170] L. Andrup, L. Smidt, K. Andersen, and L. Boe, "Kinetics of conjugative transfer: A study of the plasmid pxo16 frombacillus thuringiensissubsp. israelensis," *Plasmid*, vol. 40, no. 1, pp. 30–43, 1998.

[171] J. Seoane, T. Yankelevich, A. Dechesne, B. Merkey, C. Sternberg, and B. Smets, "An individual-based approach to explain plasmid invasion in bacterial populations," *FEMS microbiology ecology*, vol. 75, no. 1, pp. 17–27, 2011.

[172] I. del Campo, R. Ruiz, A. Cuevas, C. Revilla, L. Vielva, and F. de la Cruz, "Determination of conjugation rates on solid surfaces," *Plasmid*, vol. 67, no. 2, pp. 174–182, 2012.

[173] A. Samuels, E. Lanka, and J. Davies, "Conjugative junctions in rp4-mediated mating of escherichia coli," *Journal of bacteriology*, vol. 182, no. 10, pp. 2709–2715, 2000.

[174] T. Lawley, W. Klimke, M. Gubbins, and L. Frost, "F factor conjugation is a true type iv secretion system," *FEMS microbiology letters*, vol. 224, no. 1, pp. 1–15, 2003.

[175] R. Fronzes, E. Schaefer, L. Wang, H. Saibil, E. Orlova, and G. Waksman, "Structure of a type iv secretion system core complex. science," *Science*, vol. 323, no. 5911, pp. 266–268, 2009.

[176] D. Clewell, "Tales of conjugation and sex pheromones: a plasmid and enterococcal odyssey," *Journal of The Royal Society Interface*, vol. 1, no. 1, pp. 38–54, 2011.

[177] C. Hueck, "Type iii protein secretion systems in bacterial pathogens of animals and plants.," *Microbiology and molecular biology reviews*, vol. 62, no. 2, pp. 379–433, 1998.

[178] D. Thanassi and S. Hultgren, "Multiple pathways allow protein secretion across the bacterial outer membrane.," *Current opinion in cell biology*, vol. 12, no. 4, pp. 420–430, 2000.

[179] M. Achtman, G. Morelli, and S. Schwuchow, "Cell-cell interactions in conjugating escherichia coli: role of f pili and fate of mating aggregates.," *Journal of bacteriology*, vol. 135, no. 3, pp. 1053–1061, 1978.

[180] http://academic.pgcc.edu website, "The three types of horizontal gene transfer in bacteria are transformation, transduction and conjugation.," 2015. [Online; accessed 1 December, 2015].

[181] R. Curtiss III, "Bacterial conjugation," *Annual Reviews in Microbiology*, vol. 23, no. 1, pp. 69–136, 1969.

[182] N. Sauvonnet, G. Vignon, A. Pugsley, and P. Gounon, "Pilus formation and protein secretion by the same machinery in escherichia coli," *The EMBO Journal*, vol. 19, no. 10, pp. 2221–2228, 2000.

[183] N. Sauvonnet, G. Vignon, A. Pugsley, and P. Gounon, "Type iv pili and twitching motility," *Annu Rev Microbiol.*, no. 56, pp. 289–314, 2002.

[184] P. Silverman, "Towards a structural biology of bacterial conjugation," *Molecular microbiolog*, vol. 23, no. 3, pp. 423–429, 1997.

[185] C. Brinton, "The structure, function, synthesis and genetic control of bacterial pili and a molecular model for dna and rna transport in gram negative bacteria," *Transactions of the New York Academy of Sciences*, vol. 27, no. 8, pp. 1003–1054, 1965.

[186] A. Lawn, "Morphological features of the pili associated with escherichia coli k12 carrying r factors or the f factor," *Journal of general microbiology*, vol. 45, no. 2, pp. 377–383, 1966.

[187] R. Valentine and M. Strand, "Complexes of f-pili and rna bacteriophag," *Science*, vol. 148, no. 3669, pp. 511–513, 1965.

[188] S. Barbour, "Effect of nalidixic acid on conjugational transfer and expression of episomal lac genes in escherichia coli k12," *Journal of molecular biology*, vol. 28, no. 2, pp. 373–376, 1967.

[189] D. Marvin, "Filamentous bacterial viruses," *Bacteriological reviews*, vol. 33, no. 2, pp. 172–173, 1969.

[190] C. Thomas and C. Smith, "Incompatibility group p plasmids: genetics, evolution, and use in genetic manipulation.," *Annual Reviews in Microbiology*, vol. 41, no. 1, pp. 77–101, 1987.

[191] M. Darrenberger and W. Villiger, "Conjugational junctions: morphology of specific contacts in conjugating escherichia coli bacteria," *Journal of structural biology*, vol. 107, no. 2, pp. 146–156, 1991.

[192] M. Achtman, "Mating aggregates in escherichia coli conjugation," *Journal of bacteriology*, vol. 123, no. 2, pp. 505–515, 1975.

[193] M. Achtman, S. Schwuchow, R. Helmuth, G. Morelli, and P. A. Manning, "Cell-cell interactions in conjugating escherichia coli: Cona mutants and stabilization of mating aggregates," *Molecular and General Genetics MGG*, vol. 164, no. 2, pp. 171–13, 1978.

[194] A. Grahn, "Components of the rp4 conjugative transfer apparatus form an envelope structure bridging inner and outer membranes of donor cells: Implications for related macromolecule transport systems," *Journal of Bacteriology*, vol. 182, no. 6, p. 1564?1574, 2000.

[195] L. Andrup and K. Andersen, "A comparison of the kinetics of plasmid transfer in the conjugation systems encoded by the f plasmid from escherichia coli and plasmid pcf10 from enterococcus faecalis," *Microbiology*, vol. 145, no. 8, pp. 2001–2009, 1999.

[196] P. Broda, J. Cullum, and J. F. Collins, "Factors affecting the kinetics of progeny formation with f -lac in escherichia coli k12," *Plasmids (S. Mitsuhashi, Ed.)*, pp. 469–472, 1978.

[197] N. Hironori and S. Hiraga, "Subcellular distribution of actively partitioning f plasmid during the cell division cycle in e. coli.," *Cell*, vol. 90, no. 5, pp. 951–957, 1997.

[198] A. Derman, L. Grace, and J. Pogliano, "Intracellular mobility of plasmid dna is limited by the para family of partitioning systems.," *Molecular microbiology*, vol. 67, no. 5, pp. 935–946, 2008.

[199] A. Lilley and M. Bailey, "Diversity of mercury resistance plasmids obtained by exogenous isolation from the bacteria of sugar beet in three successive seasons," *FEMS Microbiol. Ecol*, vol. 20, pp. 211–228.

[200] N. Kroer, T. Barkay, S. Sorensen, and D. Weber, "Effect of root exudates and bacterial metabolic activity on conjugal gene transfer in the rhizosphere of a marsh plant," *FEMS Microbiology Ecology*, vol. 25, no. 4, pp. 375–384, 1998.

[201] L. Simonsen, "Dynamics of plasmid transfer on surfaces," *Journal of general microbiology*, vol. 136, no. 6, pp. 1001–1007, 1990.

[202] A. Babic, A. B. Lindner, M. Vulic, E. J. Stewart, and M. Radman, "Direct visualization of horizontal gene transfer," *Science*, vol. 319, no. 5869, pp. 1533–1536, 2008.

[203] T. Lawley, G. Gordon, A. Wright, and D. Taylor, "Bacterial conjugative transfer: visualization of successful mating pairs and plasmid establishment in live escherichia coli," *Molecular microbiology*, vol. 44, no. 4, pp. 947–956, 2002.

[204] D. Bradley, "Characteristics and function of thick and thin conjugative pili determined by transfer-derepressed plasmids of incompatibility groups i1, i2, i5, b, k and z.," *Journal of General Microbiology*, no. 130, pp. 1489–1592, 1984.

[205] H. Tuson, G. Auer, L. Renner, M. Hasebe, C. Tropini, M. Salick, W. Crone, A. Gopinathan, K. Huang, and D. Weibel, "Measuring the stiffness of bacterial cells from growth rates in hydrogels of tunable elasticity," *Molecular Microbiology*, vol. 84, no. 5, pp. 874–891, 2012.

[206] A. Howatson, P. Lund, and J. Todd, *Engineering Tables and Data*.

[207] S. Ogata and Y. Sidney, "Ideal pure shear strength of aluminum and copper," *Science*, vol. 298, no. 5594, pp. 807–811, 2002.